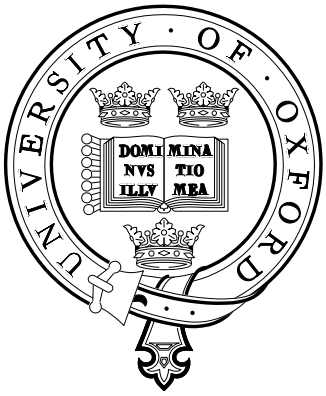
Aerodynamic flow sensing in the desert locust (*Schistocerca gregaria*)



Thesis submitted in partial fulfilment of the requirements for the Degree of Doctor of Philosophy by

Fergus McCorkell

St Catherine's College

University of Oxford

Trinity 2016

Supervisors: Prof. Graham K Taylor and Dr Richard J Bomphrey

Acknowledgments

Four years of research are encompassed within these pages. I regret that they will only capture a fraction of the insights and interests I have gained over this time. Working in the Animal Flight Group has sparked a fascination that I hope to pursue for many years to come. I give all my thanks to Graham and Richard for providing the initial opportunity and as continuing sources of education and inspiration. Richard, you once remarked that in science we stand on the shoulders of giants - you are both two such giants, and I look forward to future opportunities to work together.

To my office companions of the first three years, Tonya, Kate, and Caroline, all my thanks for providing wonderful company, and for acting as useful guinea pigs for me to observe the examination process. To the current office and members of the Flight Group, I hope I have provided similar services, I am hugely grateful to you all for making the group such an enjoyable place to work. At some time or other I have pestered every postdoc in our group for aid - perhaps this is why only one of the original members remains! Particular thanks go to Toshi, Nathan, Per, and Simon for their vital technical assistance. Additionally, I am greatly indebted to Tony and John in the workshop, without whom my experimental setups would not have been possible. A special thanks must also go to Michael Doube at the Royal Veterinary College for his insights and close collaboration on two chapters of this work.

I send all my love to my family for continuous support and for trying to explain exactly what I do to numerous baffled friends and relations. To my partner Hannah, all my gratitude for sticking with me and doing your very best to try and share in my enthusiasm for this research.

I am immensely grateful to the Defence Science and Technology Laboratory (Dstl) for funding this work and to Chris Jones in particular who has been a great support throughout.

A final note of mention must go to the great Irish folk singers, The Clancy Brothers and The Dubliners, whose music has provided unwavering succour through many long and dark hours of data analysis.

Aerodynamic flow sensing in the desert locust (*Schistocerca gregaria*)

Fergus McCorkell, St Catherine's College
(Department of Zoology)

Thesis submitted for the degree of Doctor of Philosophy at the University of Oxford, Trinity 2016.

Abstract

Insects are richly instrumented with sensors used in flight control. Whilst we have good knowledge of the basic physiology of these structures, in many cases we have only a cursory understanding of the likely stimuli each sensory system receives during flight or why these systems have evolved to perform their particular function. This thesis examines the role and optimisation of arrays of cephalic flow-sensitive hairs, called trichoid sensilla, in the flight control of the desert locust (*Schistocerca gregaria*). Particle image velocimetry and computational fluid dynamics are used to measure and simulate the airflows being received by the fields of sensilla during flight. The visualisations reveal distinct local flow conditions over each field and how these are modulated differently by perturbations. The geometry of every individual hair is captured using both benchtop and synchrotron based X-ray micro tomography (XMT). These scans enable three-dimensional measurement of each hair's direction of curvature, which represents the direction of peak sensitivity to airflow. By combining flow stimulus and directional sensitivity data, we provide strong evidence for separate fields being tuned for distinct roles: some as step detectors for monitoring stall at extreme angles of attack, others as graded sensors for angles of attack and sideslip, and possibly for monitoring airspeed. Finally, we examine the flight response of tethered locusts to varying aerodynamic stimuli by changing the angle of sideslip and selectively covering fields of sensilla from oncoming airflow. We demonstrate a clear role for the sensilla in modifying the forces and moments generated under varying sideslip, as well as in changing the underlying natural modes of motion of the system. We reveal the axes about which the locusts are unstable under our experimental conditions, and demonstrate the necessary additional sensory feedback required to stabilise the system fully.

The combined data represent a comprehensive and thorough examination of the complete cephalic flow-sensing system, providing insights applicable to both further biological study on multi-modal flight control and the use of bio-inspired arrays of sensors for manmade applications.

Nomenclature 1

Chapter 1 Introduction and background 2

1.1 Context 2

1.2 Locust mechanosensors in flight control 8

Airflow sensing 8

Load sensing 22

1.3 Manmade applications 25

Flow and load measurement for flight dynamics modelling 25

Sensory information in insects versus aircraft 28

Biomimetic sensors 29

1.4 Research questions and thesis structure 33

Chapter 2 Flow over the locust head: an experimental approach 36

2.1 Introduction 36

2.2 How can we visualise flows? 37

2.3 Methods 39

Creating a physical model 39

Particle Image Velocimetry 42

2.4 Results and discussion 47

2.5 Conclusion 55

Chapter 3 Flow over the locust head: a computational approach 56

3.1 Introduction 56

3.2 Methods 57

Mesh generation 57

Numerical technique and validation 60

3.3 Results and discussion 62

Flow over the trichoid sensilla 65

What aerodynamic features do the fields experience? 74

Airflow stimuli in the context of flight 75

3.4 Conclusion 76

Chapter 4 Head trichoid sensilla imaging 78

4.1 Introduction 78

How do we expect hairs to be oriented? 79

4.2 Methods 83

Benchtop XMT 83

Synchrotron XMT 85

4.3 Results and discussion 86

Calculating peak directional sensitivity 89
Hair metrics 99
4.4 Conclusion 102
Chapter 5 Tuning of sensilla directional sensitivity to airflows **103**
5.1 Introduction 103
5.2 Methods 104
5.3 Results 106
Are HSVs distributed uniformly? 110
Do HSVs vary across hair fields and between individuals? 111
Do different side fields have similarly oriented HSVs? 112
Do curvature and lean measurements show correlation? 114
5.4 Discussion 115
How are airflow stimuli transduced by the locust? 115
Flow sensing in a broader context 122
5.5 Conclusion 124
Chapter 6 *In vivo* sensor manipulation **126**
6.1 Introduction 126
Sensor manipulation 127
6.2 Methods 128
Axis system 128
Animals 129
Tethering 129
Force measurements 130
Flight conditions 131
Measurement series 132
Conversion of force balance output to force-moment data 133
6.3 Results 136
β derivatives 138
6.4 Discussion 142
6.5 Conclusion 147
Chapter 7 Dynamic stability analysis **148**
7.1 Introduction 148
7.2 Methods 149
7.3 Results 151
7.4 Conclusion 162
Chapter 8 Summary and outlook **164**
Bibliography **169**

Nomenclature

A	system matrix representing the natural flight dynamics
B	control system matrix
x	longitudinal axis of the locust
y	lateral axis of the locust
z	vertical axis of the locust
X	x-axis force
Y	y-axis force
Z	z-axis force
L	roll moment about the x-axis
M	pitch moment about the y-axis
N	yaw moment about the z-axis
p	angular rate for rotations about the x-axis
q	angular rate for rotations about the y-axis
r	angular rate for rotations about the z-axis
u	airspeed vector along the x-axis
v	airspeed vector along the y-axis
w	airspeed vector along the z-axis
Φ	Euler angle about the x-axis (roll)
Θ	Euler angle about the y-axis (pitch)
Ψ	Euler angle about the z-axis (yaw)
U	airspeed
$x(t)$	state vector
$u(t)$	control input vector
α	Angle of attack
β	Sideslip angle
$C_{y\beta}$	Derivative of Y with respect to β
$C_{l\beta}$	Derivative of L with respect to β
$C_{n\beta}$	Derivative of N with respect to β
Re	Reynolds number

Chapter 1

Introduction and background

1.1 Context

In contrast to manmade aerial vehicles, insects are teeming with sensors used in flight control. Typical instrumentation to directly control the flight of aircraft may amount to less than 20 sensors, while the head of the desert locust (*Schistocerca gregaria*, Forskål) lays host to over 200 hairs sensitive to air flows and approximately 40 structures to measure aerodynamic loads [1]. The human approach has not proven itself incapable; we broke the sound barrier with a manned aircraft almost 70 years ago and have since far exceeded it. We have honed distinct aircraft designs to achieve desired agility, speed, and efficiency, and air travel has become a keystone of human civilisation. So why might insects accommodate such a sensor-rich feedback system over our comparatively parsimonious approach, and why is it of interest to us?

Our failure to construct insect-scale flying vehicles of comparable agility, stamina, robustness, and autonomy suggests that the insect approach warrants further scrutiny.

Engineers have long sought to extract biological principles for their own designs, but direct mimicry of insects has proved challenging. A distinct property of insects is their lack of stabilising surfaces or structures akin to assemblies like the empennage of aircraft. Their bodies are not rigid, and the wings usually highly flexible, meaning there are many additional postural and elastic degrees of freedom to the three in rotation and translation present on any rigid flying body. Wing shape, kinematics, and body inclination can all change significantly over a single wingbeat and the flapping action itself generates highly unsteady flows that are exploited by insects to produce high-lift mechanisms for flight. These mechanisms are themselves complex and a single insect can employ several different techniques (e.g. [2, 3]). We postulate these many varying degrees of freedom and rapid changes in local forces and flows necessitate active stabilisation utilising rich sensory feedback from sensors around the insects' bodies and wings.

The CIA discovered the difficulty in replicating insect flight in the 1970s with their dragonfly-inspired Insectothopter (Figure 1) [4]. This device had a rigid body, no active sensory feedback, and only coarse control from a pilot. Consequently, it proved incapable of steady flight in even the lightest of crosswinds.



Figure 1: CIA's Insectothopter. Image credit: CIA museum.

More recent attempts have been more successful. The Aerovironment Nano Hummingbird [5] and Delfly [6-9] have both demonstrated stable flight with some autonomous abilities. However, they achieve stable orientation and basic navigation through a ground-up engineering approach, employing MEMS gyroscopes, accelerometers, magnetometers, and GPS units. This paradigm contrasts starkly with insects – the interaction between the wings, body, and surrounding airflows and forces are not directly part of the control system. Both machines have a limited flight envelope and are far from replicating the highly adaptive and intelligent behaviours of insects enabling agile evasive, predatory, and planned flight manoeuvres. A biomimetic, high-fidelity feedback approach seems logical if we are to match the aerobatics and gust tolerance of insects.

If we wish to mimic these biological systems, it is crucial to understand the entire sensory pathway from stimulation of flight control sensors, transduction and processing of the signal, through to motor output. The insect sensory system used in flight control is complex and multi-modal, incorporating visual and mechanical information across many discrete structures. Neuronal information is combined across multiple units of the same modality, such as all the individual ommatidia that constitute the compound eye, but also across different modalities. In the desert locust, visual information is fused with mechanosensors measuring flows and loads before any signal is sent to the flight motor neurons. Because of this inherent complexity, the integration and processing of these inputs remains one of the least well-known aspects of insect sensory flight control. In many cases we have only a cursory understanding of the likely stimuli to each sensory system during flight or why these systems have evolved to measure what they do [10].

In this thesis, we seek to unravel the stimuli, optimisation, and role of a key sensory system – the airflow-sensing trichoid sensilla – in the desert locust.

Desert locusts have a legacy of research dating back over 80 years stemming from a need to understand and tackle the effects of locust plagues. This puts us in the position of knowing more about their flight control sensors than any other insect. Locusts also offer certain

attributes that are relevant to flight study: they have a large body size for an insect (*circa*. 2 grams (g)) making them an attractive model to mimic and meaning the forces they generate are more readily measured using existing equipment. Additionally, they are capable of swarming, flying at night, through sandstorms, and carrying out extraordinarily long-distance flights with comparatively low metabolic rates [11], all of which are desirable qualities for manmade vehicles.

The locust sensory apparatus used in flight control consists of antennae for airspeed sensing, compound eyes for feature detection and motion vision, ocelli for horizon detection, strain-sensing campaniform sensilla, and flow-sensing trichoid sensilla (Figure 2) [10]. All of these structures are found on the head, although additional groups of campaniform and trichoid sensilla are found at various locations around the body and wings. For flow- and load-sensing structures, the location on the head likely confers a favourable signal-to-noise ratio in terms of oncoming airflow relative to airflow induced by the beating wings (assuming oncoming flow is the signal of interest). Having the visual sensors front-facing and unobstructed by other body parts also logically seems sensible. Grouping these multiple systems together on the same rigid structure potentially allows for easier integration across modalities, as any change in the orientation of the head will be experienced consistently across all sensory systems. Several other less numerous sensors, such as the force-responsive tegula [12, 13] may also be involved in flight control but have received less attention.

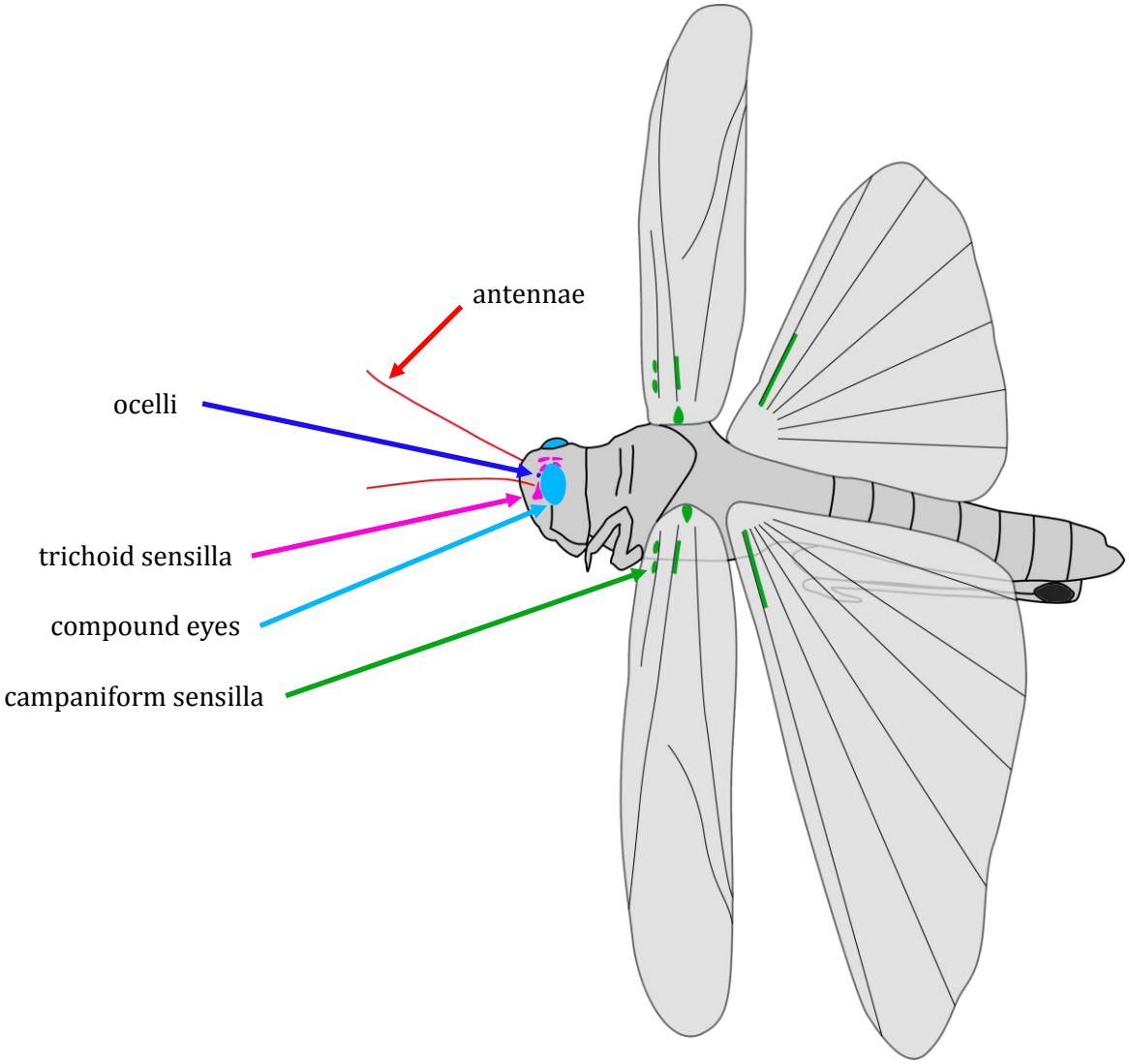


Figure 2: Sensors used in flight control by the desert locust.

The visual sensors has received more attention than any other sensory system in insects, and with good reason. You need only look at the head of an aerobatic insect such as the dragonfly to see the dominance of the visual system (Figure 3). In the brains of flies such as *Musca* and *Calliphora* we find that around two thirds of their 360,000 neurons are used in the processing of visual information [14]. One reason for this is the use of vision over a large range of distances from the insect itself. While sensors for measuring flows and loads are responding to stimuli local to the body, the visual field is used over long as well as short range to plan flight, avoid threats, and plan routes to targets [10]. The compound eyes are also usually panoramic in their coverage of the visual field. The processing of visual

information is complex and diverse, with separate pathways to process different aspects of the incoming information, such as polarisation, colour, and intensity of light, as well as magnitude and direction of motion across the retina [10].

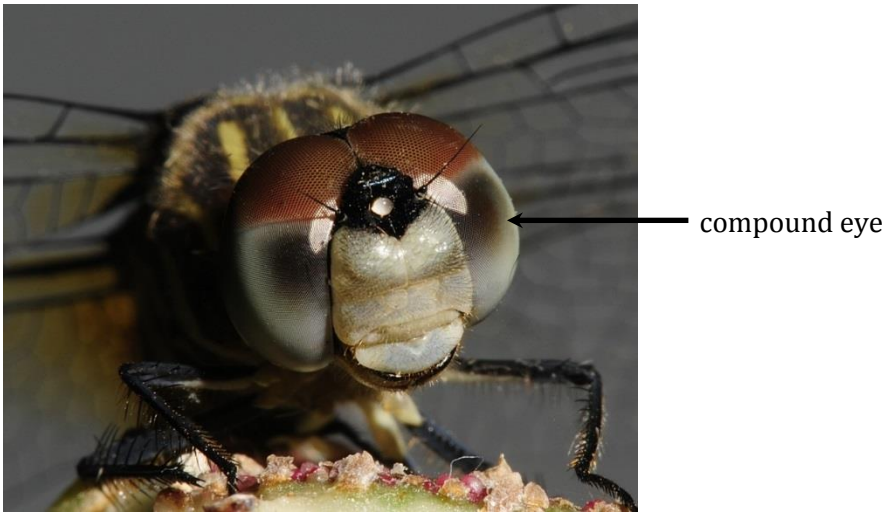


Figure 3: Dragonfly head. The compound eyes constitute the majority of the head volume, illustrating the dominance of the visual system.

The obvious importance of the visual system, and consequent large body of research on it (comprehensive review in [10] Section 3), particularly the compound eyes, has led us to be in the beneficial position of understanding their role in gaze stabilisation, indicating the self-rotations and orientation of the insect, and neuronal responses sensitive to stimuli over a range of distances. However, despite the clear importance of vision, visual information has been shown to be combined with inputs from mechanosensory force and flow sensors (antennae, campaniform and trichoid sensilla) before any signal is sent to the motor neurons controlling flapping (e.g. [15]). Mechanosensory systems are also demonstrably key to flight control; as we shall explain below, removing input from any of these systems in the locust generally has severely detrimental effects on flight. Therefore, these non-visual modalities warrant equal attention if we are to unravel the insect flight control system.

The focus of this thesis is on the flow-sensing trichoid sensilla found on the locust head, and in this introductory chapter, we provide a review on the current state of our knowledge of these structures. However, the inherently multi-modal nature of locust sensory system

necessitates that, for context, we also briefly discuss the other non-visual sensors used in flight control – the antennae and campaniform sensilla. We follow with a discussion of the application and advantages of these sensors in manmade systems, and a summary of the overarching research goals.

1.2 Locust mechanosensors in flight control

Airflow sensing

Airflow sensing is essential to insect flight control. While the visual system provides information on an insect's motion relative to some visual frame of reference, flow sensing provides this information relative to the surrounding air mass. Interaction with the surrounding air is what determines the forces and moments produced on and by the insect. We have already mentioned that the flapping wings of insects generate complex and unsteady flows, which potentially require rich feedback from flow sensors for controlled flight. There are also aerodynamic quantities well-established for manmade aircraft that are likely crucial for insects. The key quantities in reference to a flying body and the surrounding airflow are the aerodynamic angles of attack (α) and sideslip (β). These are defined in terms of the three Euler angles used to describe the orientation of a body's *x*, *y*, and *z* axes in a given reference frame. These angles are, respectively, roll (Φ), pitch (Θ), and yaw (Ψ). Angle of attack refers to the angle about the pitch axis between the oncoming airflow and some reference line on the body. While sideslip angle is the yaw of the body from the oncoming airflow (it is the lateral angle of attack) (Figure 4).

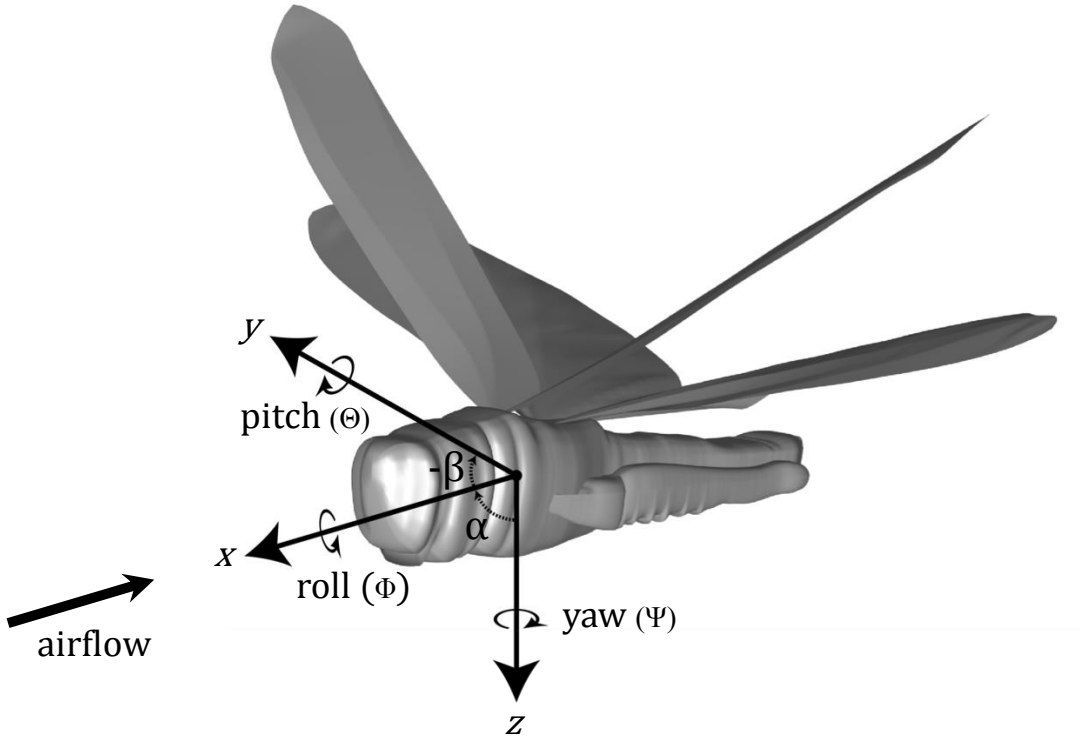


Figure 4: Aerodynamic and Euler angles. The angles of attack (α) and sideslip (β) are defined relative to oncoming airflow, and refer to orientation of the flying body about the pitch (Θ) and yaw (Ψ) axes respectively. (Locust geometry courtesy of Dr S. Walker, University of Oxford)

Angle of attack is a critical measure in manned aircraft. In the case of a conventional fixed-wing airplane, if the angle of attack is too steep, flow can separate from the wing, causing a drop in lift that may lead to severe stall. This has catastrophic consequences; potentially leading to a crash if sufficient lift cannot be restored. As a result, airplanes have dedicated sensors, typically in the form of small vanes or differential pressure probes, to constantly monitor this angle. Sideslip is also important in order to account for wind drift when flying in crosswinds. Most airplane passengers are familiar with this phenomenon (and the pilot's counteraction) when coming into land with strong winds across the strip. Vanes (oriented orthogonally relative to angle of attack vanes) are also used for sensing sideslip angle.

While the dynamics of flapping wings are somewhat different to manmade aircraft, there are likely limits to the maximum angles of attack capable in insects, particularly with non-hovering species such as the desert locust. The low body mass of insects means they will

also be highly susceptible to wind drift, and many other potentially disturbing and unsteady aerodynamic phenomena.

Thus, it is no surprise we find that insects are richly instrumented with sensors responsive to airflows. In locusts, the flow sensors involved in flight control are the antennae and trichoid sensilla. Although this thesis focusses on the latter, the relationship between the two systems is complementary and it is therefore important to discuss the respective functions of both.

Trichoid sensilla

Structure and function

Locusts have trichoid sensilla at various locations on the external surface of their bodies and wings, including around 800 on the ventral surface of each hindwing [16], and even between ommatidia [17]. A group of hairs on the prosternum have been shown to have high sensitivity to wind stimuli and therefore may be involved in flight control [18, 19]. However, the approximately 430 sensilla on the frons and vertex of the head, are the only such hairs thus far proven to play a role in flight control [10]. They vary in length from 30 to more than 350 μm, with approximately 25% over 150 μm [20]. The cephalic sensilla have so far only been accurately enumerated in *Locusta migratoria* [20], but are present in a similar configuration in *Schistocerca gregaria*. Burrows [1] states '*In Schistocerca gregaria, there are about 200 hairs…up to 300 μm*' in these fields with up to 200 additional hairs too short to be sufficiently stimulated by airflow. The hairs are individually innervated by attachment of a neuron cell to each shaft base where it meets the cuticle (Figure 5).

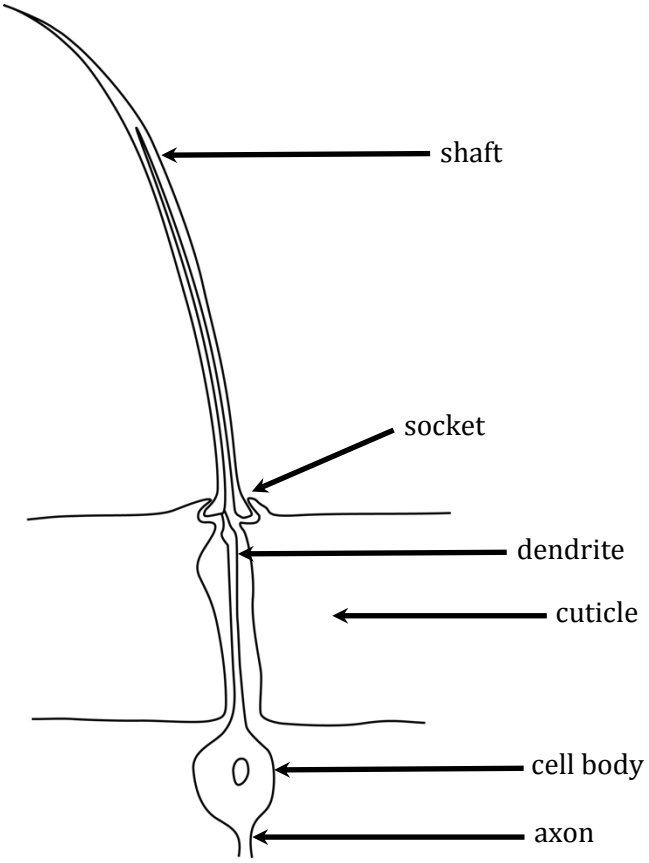


Figure 5: Structure of a trichoid sensillum. Directional sensitivity is conferred by curvature of the shaft, socket force asymmetry, and eccentric dendrite attachment. Redrawn after Camhi [21].

Each hair has a curved shaft (Figure 5 and Figure 6), creating a directionality in wind sensitivity, with peak impulse frequencies occurring in the neuron when airflow is directly opposite the hair's arc [22, 23]. Directional sensitivity is also enhanced by two other structural asymmetries: the socket force asymmetry and eccentric dendrite attachment (Figure 5). Stimulation of the hair neuron is caused by drag on the shaft from oncoming airflow causing deflection at the base, with an initial impulse frequency around 200 s^{-1} (at 4.5 ms^{-1} oncoming flow speed), falling to around 125 s^{-1} within 0.25 seconds (s) [21].

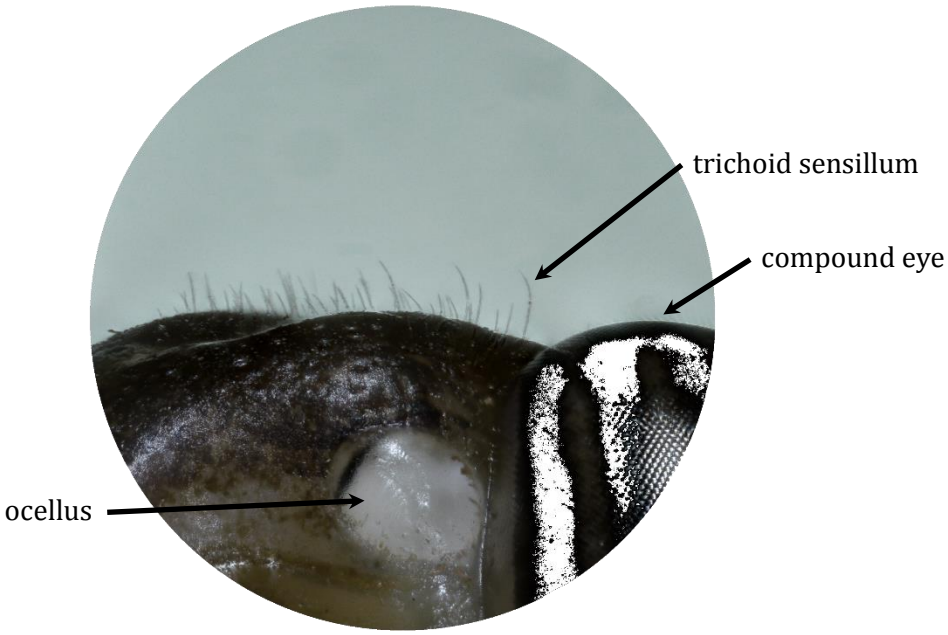


Figure 6: Anterolateral microscope view of trichoid sensilla on the top of an S. gregaria head. Note the pronounced curve of the hairs.

The impulse frequency is not only a function of wind direction, but also of wind speed (Figure 7) [21], with which it exhibits an approximately linear relationship, and temperature [23]. Because the sensory response is a function of both wind direction and speed, the locust could not employ individual sensory cells to achieve an accurate direction reading, such as that implied by Weis-Fogh's [24] behavioural experiments, as this would require some independent velocity measurement [10]. This is reflected in the neuronal connections of the hairs: individual neurons do not directly connect to motoneurons, but instead central projections terminate in the suboesophageal ganglia, with about 20% continuing on to the thoracic ganglia [17]. Therefore it is the combined inputs across many trichoid sensilla that provides the response [17].

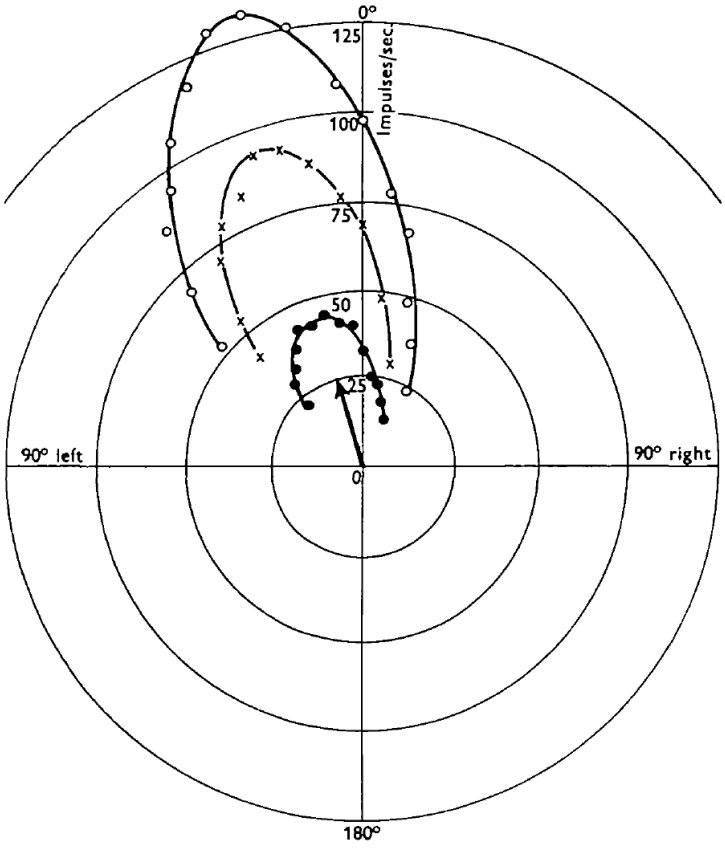


Figure 7: Camhi's original tuning curve [38], showing number of impulses against angle of airflow. The arrow represents the direction of this particular hair's curve. Filled dots, crosses, and open dots represent three different flow speeds of 1.5, 3, and 4.5 ms^{-1} respectively. Spike rate depends on direction and airspeed.

The sensilla are tapered, thinning from base to tip. The morphology of a sensor is a crucially important factor in determining its response, bestowing, for example, signal filtering or tuning properties. Modelling based on linearly tapered flow-sensing sensilla in bats demonstrated that this shape conferred relatively larger output sensitivities than hairs with uniform cross-section [25]. Bats also rely on active feedback from flow-sensing hairs to maintain flight agility [26], thus presumably the tapered shape in locusts provides similar advantage. Dickinson [25] also demonstrated that hair length was a critical design parameter, with a sharp decay in total output sensitivity as hair lengths were shifted from their optimal values. As mentioned above, the position of the hairs at the front of the head is most likely optimal for monitoring features of oncoming airflow [10].

Weis-Fogh [24] demonstrated the role of cephalic sensilla in initiating and maintaining flight in tethered locusts. Covering the hairs removed this response, however, throwing locusts into the air with covered hair fields still resulted in flight initiation. This is in agreement with Camhi [22], who found that wind stimulation of the cephalic sensilla leads to opening of the wings in approximately 45 milliseconds. Locusts in a take-off jump opened wings within 15 milliseconds after the first jump motion, suggesting the cephalic sensilla do not play a role in this scenario. Increased airflow over the cephalic sensilla also caused reduced pronation on the downstroke, resulting in an increased lift-to-drag ratio and ascending flight. Static deflection of the hairs is insufficient to initiate flight [27, 28] due to the phasic response of the hairs [29].

Weis-Fogh defined the trichoid sensilla on the head into discrete fields, numbering the fields F1-5 [24, 27], a convention which has been adopted in subsequent studies (e.g. [10, 23]) (Figure 8).

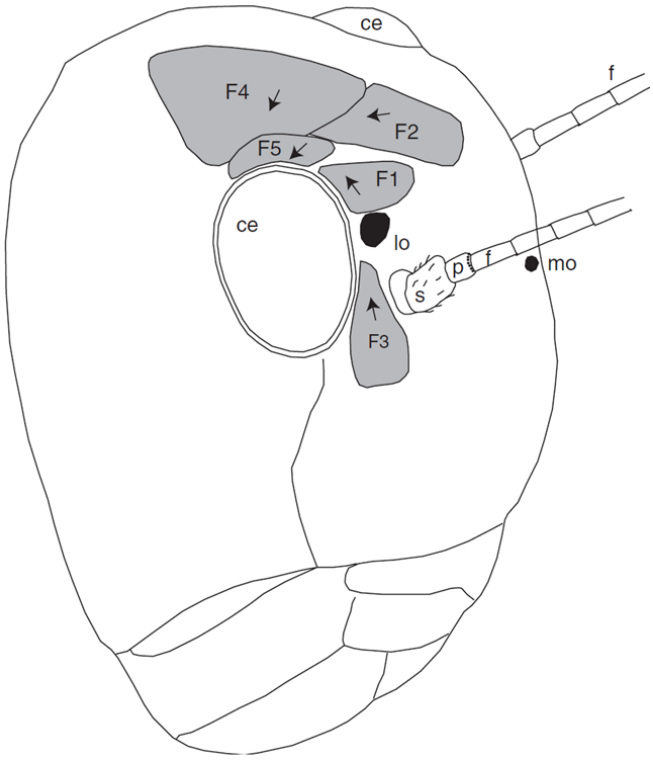


Figure 8: Five fields of trichoid sensilla for one side of the head as originally defined by Weis-Fogh [43]. Arrows denote the approximate average peak directional sensitivity of hairs within each field [6]. ce = compound eye, lo = lateral ocellus, mo = median ocellus. s, p, and f are the scape, pedicel, and flagellum of the antenna respectively. Figure reproduced from [10].

He found a role for the hairs in stabilising yaw (i.e. controlling for sideslip) by observing locusts turn into asymmetric airflows when tethered to apparatus permitting rotation in the yaw axis. Covering of the F3 field eliminated this reaction [24]. With most likely more accurate apparatus [10], Gewecke and Philippen [30] found that, so long as F1 was left intact, there was always some response, and covering F1 created as strong a suppression as covering all four of the other fields. Camhi [31] found that F2 in particular was linked to changes in abdominal position that occur with varying airspeed – with the abdomen being lowered with decreasing speeds. Covering F2 abolished or greatly reduced this response (as did covering F1 and F3, to a lesser degree). An additional study found that covering F2 also disabled the symmetric movements of the abdomen that occur when varying airspeed [32].

The rationale of Weis-Fogh's [27] discretisation of the hairs into 5 groups is a moot point as this is not necessarily reflected in the underlying neuronal arrangement. Indeed, at least one of the wind-sensitive descending interneurons receives input from the hair neurons of all five fields, and Tyrer et al. [33] define only three groups when classification is done according to innervation of central neuronal projections (F3, F1+2, F4+5).

Smola [23] and Camhi [21] both attempted to map qualitatively the peak directional sensitivity of a number of trichoid sensilla based on their curvature, but clear discrepancies arise when comparing their respective measurements (Figure 9).

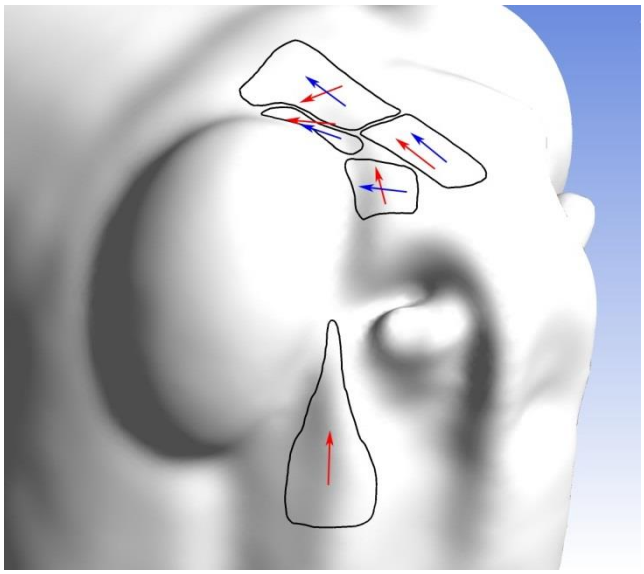


Figure 9: Peak directional sensitivity of hairs to airflow within each field from two papers, red arrows after Smola [23], blue arrows after Camhi [21]. Note, Camhi did not publish directional measurements from F3.

Camhi [22] conducted a study of descending interneurons (DNs) postganglionic to the hair neuron axon terminations, demonstrating that multiple sensilla sensory cells connect with each interneuron. Deflection of a single sensillum is not a sufficiently strong stimulus to evoke a response in the interneuron, while bending 3-4 sensilla would produce several spikes. Interneuron spike frequencies were consistently lower than those of the hair neurons. Camhi characterised four distinct categories of interneuron based on their responses to airflow stimulation of the cephalic sensilla: (i) 'wind-indicator cells' producing

a slowly adapting response to wind from a wide range of directions, with a threshold airspeed 0.1 ms^{-1}. (ii) 'wind-direction cells' also giving a slowly adapting response, but constrained to a narrow range of directions, with maximum response when wind is directed in the optimal direction. (iii) 're-centre cells'. (iv) 'acceleration cells' with a phasic response and threshold airspeed of 1.0-1.5 ms^{-1}. 'Wind-indicator' and 'acceleration' cells showed a bilaterally symmetrical response and thus cannot discriminate between wind from the left or the right. Responses therefore suggest different interneuron categories have roles in flight maintenance and yaw-correction.

Camhi's work may appear to have neatly characterised the response of the DNs, tempting us to think we have a good idea of the signal passed from the DNs onto the motoneurons. However, the role of the trichoid sensilla is part of a larger and considerably more intricate picture because all DNs currently known to receive input from the cephalic sensilla also receive input from the visual system (compound eyes and ocelli). Rowell [15] provides a concise review of the relevant DNs scrutinised so far, classifying them into several groups: directional neurons responding almost entirely to wind-sensitive inputs from the trichoid sensilla (e.g. [34]), neurons dominated by the visual system [35], directional neurons responding to both visual and wind input [36], those receiving additional inputs from neck proprioceptors [15], and those receiving inputs from multiple modalities but with little directional sensitivity.

Those exhibiting clear directionality in their response often have a further discrimination to just certain movements. For example, in the case of three well-characterised DNs , DNI, DNM, and DNC, tethered flight neuronal measurements demonstrated DNI responds maximally to ipsilateral diving banked turns, DNM to downwards pitch, and DNC to diving banked turns to the contralateral side, under simulated visual and wind stimuli rotations [37]. All three of these DNs receive input from the compound eyes, ocelli, and trichoid sensilla, and in each DN, all of these modalities were most sensitive to the same characteristic manoeuvre. In the case of DNs receiving multi-modal inputs, the relative inputs of each modality can vary and depend upon each other. In one elegant demonstration,

input from the ocelli could suppress responses to compound eye or trichoid sensilla stimuli, while in another example, the response of the trichoid sensilla in daylight was approximately one tenth that in dim light [37]. Some of these directional DNs have been well characterised in their role in corrective steering of locusts (with their output to motor neurons being shown to control wingbeat and abdomen and hind leg ruddering), acting analogously to an autopilot to deal with deviations from set course [15].

The fusion of sensory information at such an early stage makes it extremely difficult to decouple the effects of visual and mechanosensory systems on the flight motor. Therefore, the sensilla are clearly most accurately considered as one input of a multi-modal interneuronal response. However, we still do not have a thorough understanding what form this one input takes, other than to say the hairs detect deviations from straight flight [10, 37]. This leaves substantial gaps in our understanding of how the hairs are used in the stabilisation and control of locust flight. Additionally, we do not know how the flow stimulus over the head capsule corresponds to the directional sensitivity of the five groups of hairs.

Antennae

Structure and movement mechanism

As with all winged insects, locusts have a pair of antennae on the head used for mechanoreception, chemoreception, hygroreception, and thermoreception [38]. While the trichoid sensilla can provide both airspeed and directional information, the antennae appear to predominantly be used for airspeed sensing in flight control [10].

The locust antenna consists of a basal segment known as the scape, an intermediary segment called the pedicel, and a long multi-element structure, the flagellum (Figure 10). The head-scape and scape-pedicel linkages are true muscular joints, while the pedicel-flagellum junction allows only passive deflection. At the pedicel-flagellum joint, there is a Johnston's organ; a stretch-sensitive scolopalial receptor, consisting of 12 units in the migratory locust, *Locusta migratoria* [39]. There are approximately 70 campaniform

sensilla (strain-sensitive pores) on the distal rim of the pedicel. The individual units of the flagellum, annuli, lack any musculature [40].

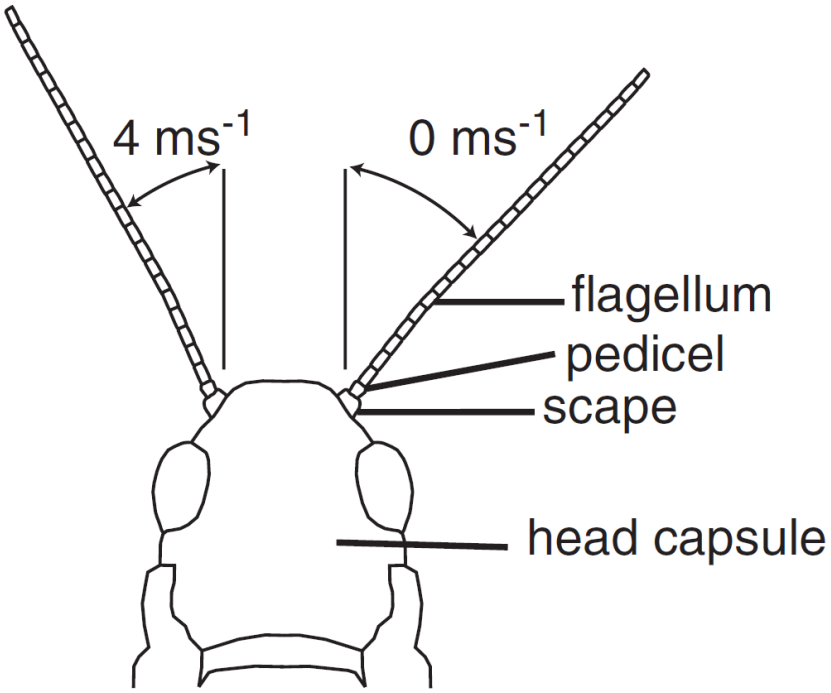


Figure 10: Structure of the locust antennae. In preparation for flight, the antennae are actively protracted forward. The angle between the antennae and long axis of the body decreases with increasing airspeed. Figure from [10].

Function

Both passive and active antennal movements are involved in flight control in what is known as the antennal positioning reaction; the active protraction of the antennae against airflow in flight (Figure 10) [41, 42]. The reaction most likely serves to keep mechanosensors in the pedicel within their optimal operating range. It starts with a feed-forward response, with the antennae being actively positioned in preparation for flight (Figure 10). Stimulation of the reaction in flight results from the passive deflection of the antennae backwards and to the side caused by drag on the flagellum, creating a torque that results in a 1.3° or less deviation at the pedicel-flagellum joint [39, 43]. This deviation stimulates the approximately 70 campaniform sensilla on the rim of the pedicel with the neuron spike rate providing information on the level of deflection at the pedicel-flagellum joint. They exhibit a phasic-

tonic response, with the tonic discharge frequency being approximately linear to the deflection [44]. This information then appears to be used to determine the active positioning of the scape-pedicel joint.

The positioning reaction serves to reduce drag on the antennae by decreasing the surface area exposed to oncoming flow, and in so doing keeps the Johnston's organ in its optimal operating range [10]. The Johnston's organ exhibits a phasic response [45] and is highly sensitive to even minute vibrations. The antennae are rotated forward about the scape-pedicel joint in opposition to the passive deflection at the pedicel-flagellum joint [41, 43, 46, 47]. The angle between the antennae and the long axis of the body decreases with increasing airspeed (Figure 10).

Other sensory structures are found on the locust pedicel (as they are in all flying insects studied to date), including basiconic, trichoid, coeloconic, and chaetical hairs [48], however, they are not necessarily involved in flight control as the antennae are multi-functional sense organs. The campaniform sensilla appear to be of vital importance in antennal positioning; elimination of the single campaniform sensillum in *Calliphora* removes the reaction entirely [41, 46].

Flight Speed

Wind tunnel experiments with tethered locusts have looked at wing beat frequency, flight speed, lift, and wing-stroke angle after antennal manipulation [49]. Immobilisation of the pedicel-flagellum joint (and thus the pedicellar mechanoreceptors) resulted in the wing stroke angle (the angular distance travelled by the wing through a whole wingbeat in the stroke plane), decreasing less with increasing airspeed when compared with non-manipulated individuals [50]. Later closed-loop apparatus experiments allowed accurate measurements of airspeed changes [49]. Here, the head capsule to the third flagellar annulum was immobilised using resin, resulting in wingbeat frequency decreasing less over time during flight, flight speed remaining consistently higher over time, and flight having

fewer stalls. Conversely, immobilising the airflow to the trichoid sensilla resulted in the opposite being observed for the same parameters.

Thus, it appears that antennae inhibit increased flight speed and its dependent parameters, while the cephalic trichoid sensilla stimulate increased flight speed, creating an antagonistic feedback mechanism. This is in contrast to other flying insects, with antennal amputation resulting in decreased speed in free-flying *Drosophila*, *Apis*, and *Aglais* [51-53], although this may just be a result of general flight degradation [10]. Antennal modulation of flight speed is likely to be important in long-distance flight or migration because metabolic rate does not increase linearly with flight speed, instead increasing approximately as the square of speed [54].

Taylor & Krapp [10] make an important note on exactly what the antennae measure. Whilst they are clearly used to regulate airspeed, they do not provide absolute measurements of airspeed. Rather, the antennal positioning reaction acts like a high-pass filter, with the Johnston's organ sensing changes in airspeed. Heran [55] pointed out that any absolute measurement of airspeed by the sensors of the pedicel–flagellum joint can only ever be as good as the estimate of the angle of the scape–pedicel joint by its sensors. This is no longer an issue if measurements are not absolute. Based on the model of antennal function above, it appears insects are able to regulate their airspeed simply by measuring changes in airspeed in a more or less linear manner.

The antennal muscles receive input from the visual system as well as from the antennal mechanosensors. Krishnan and Sane [56] have demonstrated that antennal muscles also respond to input from the visual system in *Manduca sexta* (Tobacco hawkmoth), and in locusts, there is a sensory fusion of information from the visual system and pedicel mechanosensors. A potential hypothesis of how this integrates into the positioning reaction could be that the set point for the insect's airspeed is adjusted by introducing an offset in antennal position, and that this is commanded on the basis of changes in optic flow indicating wind drift.

Flight direction

The function of locust antennae in flight is similar to that of many other insects, such as *Calliphora*. However, *Calliphora,* have a unilateral system of neural connections, allowing the antennae to be used in yaw control. For example, an unintentional turn will cause imbalanced impact pressure between the two antennae, inducing a decrease in the wingstroke amplitude on the side of the more strongly stimulated antenna, thus correcting for the turn [46, 49, 57]. Additionally, amputation of one antenna affects the stroke amplitude of the ipsilateral wing, but not the contralateral [41, 46]. Interestingly, in two locust genuses, *Locusta* and *Schistocerca*, the picture is more complicated. Unilateral amputation of antennae in *Locusta* has no effect on stroke amplitude of either wing, suggesting that they are unlikely to be used in the control of flight direction [30, 49]. However, Arbas' [58] sensor manipulation experiments in *Schistocerca* showed that the antennae are apparently responsible for downwind steering movements of the hind limbs and abdomen in response to asymmetric (in yaw) airflow. Attenuation of the antennae removed both these responses. Thus, at least in *Schistocerca*, the antennae may play some role in directional control.

Load sensing

Sensing aerodynamic loads appears to be pervasive across flying insects. Although there are many force-sensitive structures on insects, the role of campaniform sensilla in flight control is particularly well characterised.

Campaniform Sensilla

Structure

A single campaniform ('bell-shaped') sensillum consists of an oval-shaped dome and a ring of raised cuticle, (a 'cap-and-collar' arrangement) that responds to cuticular deformations [59] (Figure 11).

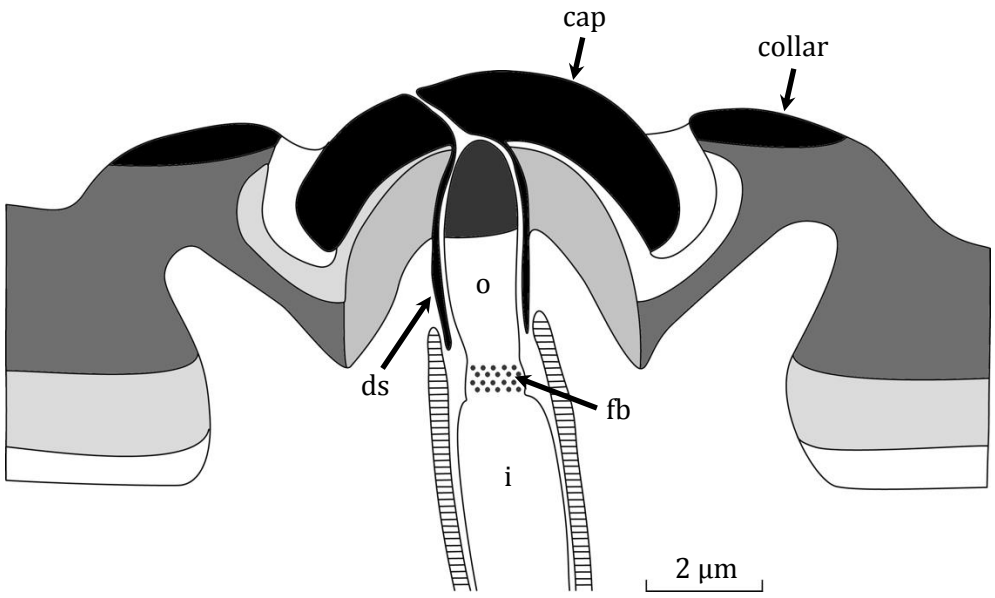


Figure 11: Structure of the campaniform sensillum. A cap-and-collar arrangement of a suspended dome surrounded by a ring of raised cuticle. A single pore runs through the cuticle which deforms under loading. ds = dendritic sheath, fb = fibrillar body, i,o = inner/outer dendrite. Redrawn after [59].

The cap in Figure 11 shows a single pore running through the cuticle, although not all campaniform sensilla have a pore. The cap deforms in response to loading, while the chitin collar is arranged in such a way that it carries the loads around it [60]. The oval shape confers anisotropic properties due to non-uniform levels of cap deformation in each direction, with maximum sensitivity to deformation perpendicular to the long axis [61-63]. As the sensilla respond to cuticular deformation, they are logically found near sites of likely deformation, with some of the highest densities being found near joints, such as the base of wings [64] and on the legs [65].

As locust wings are highly deformable and actively twisted to change angle of attack, they are obvious candidates for the placement of strain sensors. Campaniform sensilla are found on the ventral wing surface [66], specifically, 60-70 on the distal section of the subcostal veins, with their long axes parallel with the long axes of the wings, in both fore- and hindwings (Figure 2). Additionally, two smaller groups are found on the forewing; a

proximal subcostal group of 20-21 with their axes arranged in a fan shape, and a small group on the costa [63, 64] (Figure 2). The two subcostal forewing groups differ in length of cuticular dome, perhaps indicating they respond to deformations of different magnitude.

Function

Recordings in response to excitation of the campaniform sensilla have been taken from the sensory neurons leading to the wing base [63, 64, 67], individual interneurons [68, 69], and flight muscles [63, 70-72]. The sensilla are excited on each wingbeat, firing only on the downstroke, with inhibition occurring when the wing is pronated [63, 69]. Information on wing deformations caused by aerodynamic lift and thrust is thereby fed back during the depression phase of wing movement [1]. The sensilla exhibit a phasic response [63], and their firing rate is a function of wing angle of attack [64].

Destroying the campaniform sensilla on the hindwing removes the ability for locusts to twist their wings in what has been referred to, probably erroneously, as a "constant lift reaction" ([73], but see [74]). Elson [68, 69] identified an interneuron that receives direct input from sensory neurons of campaniform sensilla on one hindwing, which could be involved in regulating twisting of the forewings in response to input from the campaniform sensilla of the hindwing [1]. The forewing sensilla are key to rapid corrections in angular deviation in all three axes of the body, with their destruction resulting in sporadic and unsustainable flight [64]. However, the picture is somewhat obfuscated in that this interneuron also receives input from the medial and contralateral ocelli.

There is clearly much scope for further work on campaniform sensilla if we are to understand their integration into the flight control system. For example, although these sensors almost certainly provide a direct measure of the aerodynamic load that the wings take, it is unclear whether their primary function is to detect changes in aerodynamic load that are brought about by changes in the motion state of the whole insect (e.g. changes in body angle) or changes in the wing kinematics relative to the body (e.g. changes in the extent of wing rotation) [10]. Once again, their possible role in controlling flight kinematics

is complicated by the fact that input from the campaniform sensilla is fused with the visual system. We also do not fully understand the significance of the different groups of campaniform sensilla on fore and hindwings other than to say they are presumably measuring forces of differing magnitude and/or direction. The two sets of wings do not respond to lift equally; while the forewings change their angle of attack with increasing body angle, the hindwings are twisted less and in fact inhibit flight speed [75]. Additionally, the significance of the sensilla's directional sensitivity has not been explored in the context of insect flight control and stabilisation.

1.3 Manmade applications

Flow and load measurement for flight dynamics modelling

The review above reveals we have a surprisingly detailed knowledge of the structure and function of the trichoid sensilla (as well as the antennae and campaniform sensilla) but with obvious gaps relating to exactly what they are measuring and how this is fed back to the flight control system. However, what we do know is that locusts are receiving distributed direct measures of flows and loads in a way that is not currently used in manmade air systems. We have already discussed some of the differences and relative merits to employing a sensor rich feedback system over man's approach. Here, we briefly examine how flow and load sensing could aid in modelling the flight dynamics of manmade vehicles, particularly in the case of flapping flight, as postulated by Taylor [76].

Analysing the dynamics of an aircraft is a vital part of the design process, being necessary to understand and hone flight performance. The benefits of using direct flow and load sensing can be explained by considering that in flight dynamics the solid body motion is coupled with the aerodynamic state of the surrounding air. An aircraft's flight dynamics could therefore be calculated by solving simultaneously the coupled solid body equations of motion and Navier–Stokes equations of fluid flows [76]. However, the initial formulation of aircraft flight dynamics by Bryan at the turn of the last century was a set of differential

equations of motion in which the aerodynamic state of the flow field was not directly included [77] (Figure 12). This conveniently dealt with the problem that the Navier-Stokes equations make any solution infinite-dimensional, as they describe the motion of the fluid at infinitely many points [76]. Instead of including any aerodynamic term, Bryan represented aerodynamic forces and moments, $\mathbf{X}(t)$, as functions of the motion state variables defining the solid body motion, $\mathbf{x}(t)$: i.e. $\mathbf{X}(t) = f(\mathbf{x}(t))$. This meant that any given set of instantaneous motion state variables were assumed to map onto a unique aerodynamic state (Figure 12) [76].

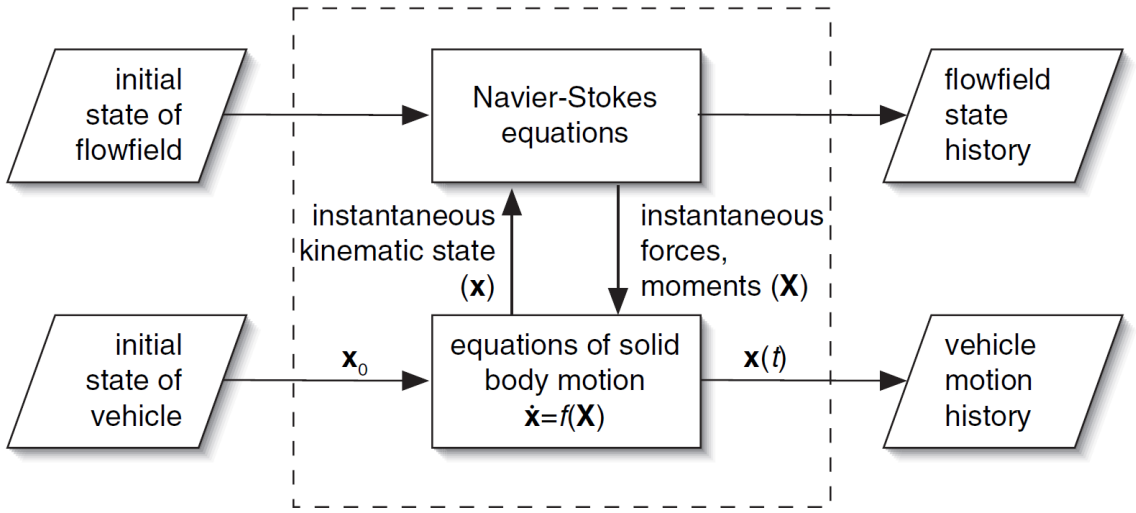


Figure 12: Bryan's model of flight dynamics, in which the aerodynamic forces and moments do not appear explicitly, but are represented as a function $\boldsymbol{X}(t) = f(\boldsymbol{x}(t))$, which associates the current values of the aerodynamic forces and moments $\boldsymbol{X}(t)$ with the current values of the system states $\boldsymbol{x}(t)$. Image from [76].

Unfortunately this causes problems when modelling unsteady flows, because in such cases the aerodynamic state of the system is defined not only by the current values of the motion state variables, but in combination with their time history [78]. Thus Bryan's formulation assumes a quasi-steady flow.

The formulation was later reworked by Tobak & Schiff [78] so that the aerodynamic forces and moments were represented as functionals of the body's motion state. This method accounts for the time history dependence as the aerodynamic forces and moments are expressed in terms of the system's current and past states. However, we once again have

the problem of infinite dimensionality, because the current state of the system is defined in reference to its prior states through infinitely many points in time [76].

A potential alternative is to include in the solid body equations of motion one or more summary variables, or 'internal states', that are sufficient to define the current aerodynamic state of the system, for example, the chord-wise position of the wing flow separation point (Figure 13) [76, 79, 80]. Using this approach, it may be possible to avoid altogether the time history dependence, because the state of the unsteady flows is included as a state in the model. This formulation so far only appears to have been used in theoretical models of flight dynamics [76, 79, 81]. However, we hypothesise that the measurements of flow state made by the trichoid sensilla can be thought of as measuring an internal aerodynamic state of the system. Campaniform sensilla likely confer similar advantage, providing an instantaneous measure of wing loading.

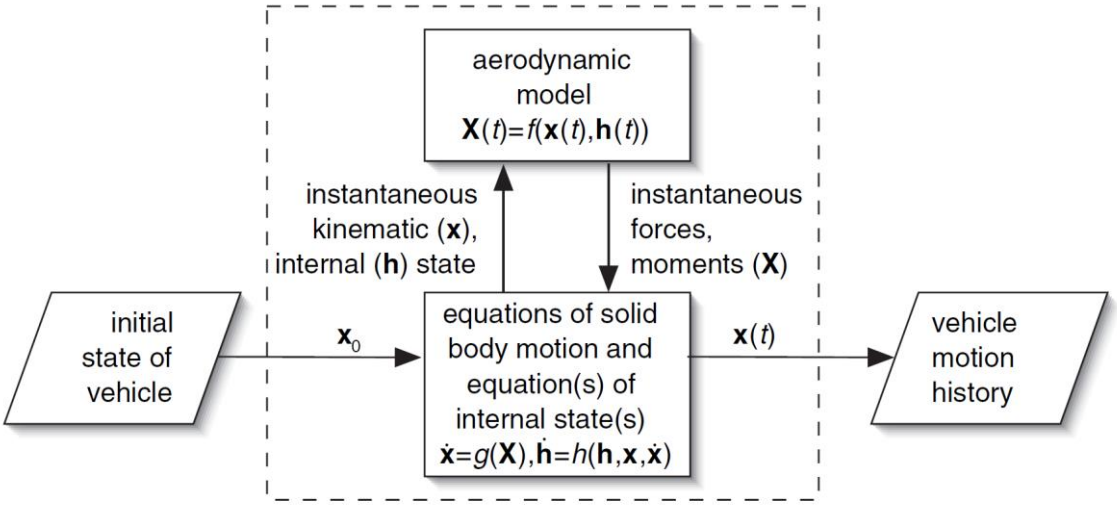


Figure 13: Goman & Khrabrov's [79] approach to flight dynamics modelling, in which the unsteady aerodynamic forces and moments are represented as functions of the current values of the motion state variables, together with one or more additional 'internal state variables' describing the current aerodynamic state of the system. Image from [76].

This alternative approach to flight dynamics modelling is directly applicable to the control systems of vehicles. Just as the equations of motion are defined in terms of motion state variables, aircraft feedback control systems typically determine control inputs based on

current values of the same variables. Therefore, including suitable additional 'internal state' terms could produce improved control systems that explicitly include the aerodynamic state around the vehicle, in a manner that avoids time history dependence.

Sensory information in insects versus aircraft

The previous section illustrates that distributed flow and load sensing could provide novel ways to model aircraft dynamics and design control systems. It is, however, important to consider the way in which insect sensors function and measure information relative to our current manmade sensors, if we are to utilise similar principles in future control designs.

In addition to the disparity in number of sensory units between insects and manmade aircraft, insect sensory systems provide information in a fundamentally different manner. Typical aircraft avionics include a Pitot tube for airspeed measurement, vanes or differential pressure probes for measuring angle of attack and sideslip, gyroscopes and accelerometers to sense angular velocity and attitude (through fusion of data from both sensors), and an altimeter. Therefore, one may be inclined to consider insect sensors as analogues of these instruments that measure similar variables. However, insect sensors typically measure *changes* in the states of these variables as opposed to an absolute state. One particularly clear example is the dependency on temperature of certain sensors, such as the head trichoid sensilla and the wing-hinge stretch receptors [82]. Although sensitivity to temperature is a common problem with manmade transducers, it can usually be controlled for, whereas insects do not appear to have any obvious independent measure of temperature with which they could obtain an absolute measure. The adaptive nature of the antennae, due to the constantly changing angle of the scape-pedicel joint, means they too are suited to measuring changes in airspeed and not absolutes.

Two other contrasting principles particularly stand out between insect and manmade sensing. The first we have already discussed above in the context of the trichoid sensilla – that insects sense and combine multiple modalities into composite signals prior to that information being processed and sent to the flight motor. Secondly, insect sensors are

typically arranged in a highly non-orthogonal (yet highly organised) fashion relative to the major axes of the body [10]. This contrasts to the orthogonal arrangement employed with manmade sensors, which we use to confer equal sensitivity to motions in any direction and to simplify signal processing [10].

Taylor and Krapp viewed these distinct features of insect sensory systems as indication of an entirely different control architecture in insects, which they explain by proposing the 'mode-sensing hypothesis' [10]. This states that the various insect sensory systems used in flight control are tuned to sense excitation of the natural modes of motion that characterise an insect's flight dynamics. The theory has been formalised and developed in the context of the visual system of flies, and put into a framework to apply to other sensory systems and other modes of locomotion [83]. It may be the case that in order to use a multi-modal and rich sensory feedback system in manmade flight control systems, a biological model such as this would be required, representing a large departure from existing ground-up engineering approaches.

Recently, a new paradigm, known as fly-by-feel (FBF) has been proposed to enable aircraft stability and performance across a wide range of conditions [84]. The vision is of a tight integration of active, distributed sensing with adaptable structures and control surfaces in order to optimise aircraft configuration as conditions change. Thereby flight performance is enhanced and disturbances, such as strong destabilising gusts, are alleviated. The increased degrees of freedom proposed under such a regime more closely resemble the various postural and elastic degrees of freedom common in flying insects. Moreover, with the tight integration of active sensory feedback, this paradigm bears remarkable similarities to natural systems. We briefly discuss below attempts to mimic biological sensors that could feasibly be used for FBF sensing and control.

Biomimetic sensors

The few sensors typically installed on our aircraft provide a spatially small amount of local information, feeding data into a handful of feedback loops, requiring a few complex and

computationally demanding controllers to estimate the state of the entire aircraft. In contrast, sensor arrays around large areas of the insect body are feeding into numerous discrete feedback systems and loops, resulting in many simple controllers [85]. The second (insect) paradigm is intuitively attractive in its potential to provide a far better state estimation (typically in terms of attitude, velocity, and angular velocity), of both the aircraft and local aerodynamic states, as well as bestowing high redundancy. On this latter point, there is likely a trade-off to the engineer between manufacturing, integrating, and maintaining many individual sensor units relative to the benefits of redundancy.

One engineering approach analogous to the arrays of insect sensors is the use of flush air data sensing (FADS) systems. FADS systems are flush pressure sensing ports used in concert to characterise the air state, providing an alternative to traditional pitot tubes or vanes mounted on air data booms. While pitot tubes and vanes have proven themselves capable and functional, air data booms have several disadvantages; measurement error can be incurred through vibration, bending, probe size, geometry, or by flow interference from the probe itself [86]. They are also exposed to the weather conditions external to the aircraft and are liable to freezing. FADS can potentially mitigate all of these vulnerabilities, whilst conferring the benefits of richer information and redundancy.

Historically FADS arrays have been placed near the aircraft nose tip to allow easy integration with the existing aerodynamic models and because this is a traditional point of measurement for air data booms. However, more recent experiments on micro air vehicles have placed arrays of FADS on the leading edge of the wing [86]. The neural-network-based model for processing FADS information in [86] demonstrates an approach to sensor integration that is increasingly analogous to what is likely happening in birds and insects.

There have also been many attempts to mimic directly the function and structure of biological sensors, including flow-sensing hairs. In the last decade or so, many research groups have attempted to build biomimetic flow-sensitive hairs with response properties and scale comparable to the trichoid sensilla of locusts (see e.g. [87-95]. These prototype

flow sensors measure the moment on a sensory hair-like structure, typically using strain gauges. For example, Ozaki et al. [95] constructed a simple two degrees of freedom biomimetic hair consisting of strain gauges near the base, mounted in cantilevers. This design allowed airspeed and direction to be measured by monitoring changes in strain gauge resistance caused by airflow against the cantilever. A simple strain gauge can still suffer from inaccuracies caused by temperature drift, however several solutions are possible to avoid this, for example, manufacturing the gauge material to compensate for thermal expansion or using multiple strain gauges in a Wheatstone bridge arrangement (either half-bridge or full-bridge) [96]. Thus, the hairs can be designed so that strain gauge resistance is a function of only airspeed and direction, and can therefore act as velocity sensors when multiple hairs with different directional sensitivity are used together.

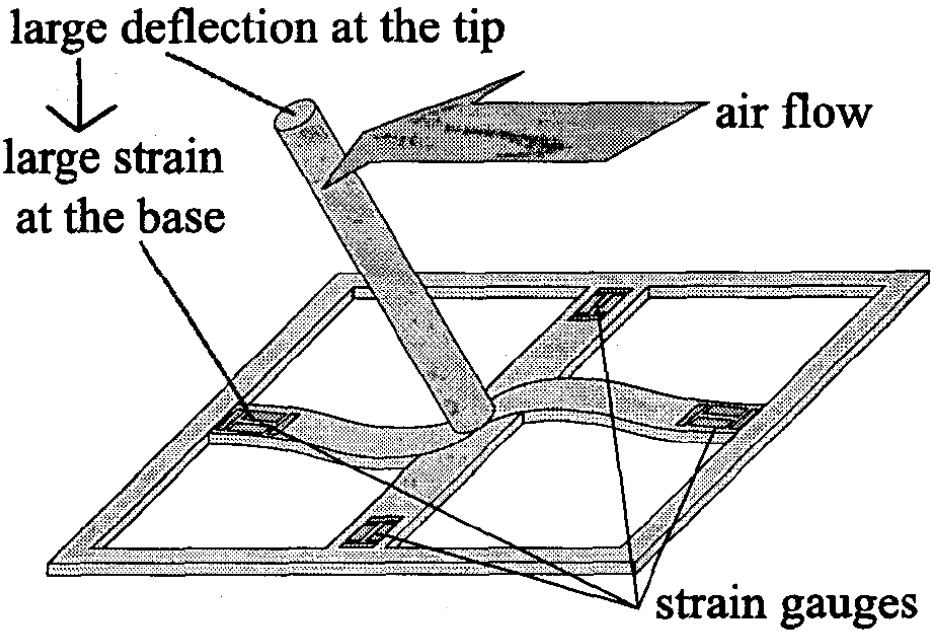


Figure 14: Two degrees of freedom biomimetic flow-sensing hair using strain gauges. Figure from [95].

Other artificial hair sensors have used different transducer mechanisms, for example optical [91] and capacitive transduction [97, 98], however, strain gauge based designs offer simpler design and integration procedures. In 2012, Maschmann et al. [92] produced carbon nanotube arrays (attached to strain gauges), with tube sizes ranging from 12 μm to 225 μm,

and densities up to 100 per mm^2. The arrays exhibited a non-linear response to airspeed, but the scale, density and range of airspeeds the arrays could measure were all comparable to those seen in locusts and are therefore a promising solution for flow sensing at the scale of insects. More recent research from the US Air Force Research Laboratories (AFRL) [99-102] is building on this work, providing ever more thorough characterisation of hair sensor designs. They are now turning their attention to the role such sensors could play in active flight control, with preliminary experiments focussing on gust alleviation [103] and detecting flow separation [104].

The AFRL's approach of using manmade carbon nanotube technology, but replicating the biological principles of flow-sensing hairs, strikes a balance between engineering and biology. Despite the rush of interest in bio-inspired technologies, several scientists have warned of trying too closely to mimic biological systems. To take the simple example of the insect ocelli, they are low resolution visual sensors primarily used for horizon detection and orientation, and could be replaced with MEMS IMUs in manmade systems. Thus, as Zbikowski [85] posits, this control architecture, '*works on the complementarity of the type of information measured, not the type of instrument used. So, the issue is not to emulate insect sensors, but to use appropriate instrumentation to extract the relevant information with the required speed and accuracy.*'.

This approach to bio-inspired design is not new, and several strategies have been suggested to best identify and reproduce features of biological systems (a comprehensive review can be found in [105]). It seems a reasonable framework for several reasons; we have developed materials, processes, and technologies that are very different to biological systems. Indeed, while biological materials are made from one or both of only two polymers – proteins and polysaccharides – we have had use over 300 polymers, including metals to generate the same range of properties [105]. Typically, manmade high-speed actuators are based on rotating mechanisms, while in biology, they are often linear (such as muscles) or oscillatory (for example cilia) [105]. Additionally, many biological structures are multi-functional, for example, antennae are used actively to control airspeed during flight, but also for chemo-

and hygro- sensing, and in courtship. This puts multiple selection pressures on these structures, potentially to the detriment of their function in flight control. Our current inability to create organic analogues to living structures may also necessitate a different approach. It is important to consider where biological structures may be inferior due to developmental constraints. For example, while wheels are advantageous over legs in many situations, the necessity for various circulatory and nervous systems in biological bodies impedes occurrence of such freely rotating structures.

It is likely a balanced approach is most appropriate for mimicking insect-scale flapping flight. While IMUs could replicate the role of ocelli, as we discussed in the beginning of our introduction, an IMU-only approach to full flight control has so far only yielded flapping vehicles of limited flight envelope.

1.4 Research questions and thesis structure

In summary, there have been some significant advances towards fabricating solutions to sensing flows akin to what is seen in natural systems. However, attention has only recently shifted to focus on how such information could be integrated into the flight control system. This reflects the continuing work to overcome current obstacles in design and fabrication processes, but also the lack of work from biological and engineering perspectives as to what aerodynamic features such sensors should measure, and how to use this information. This is the focus of the present study.

We have outlined the state of knowledge on the three locust mechanosensory systems used in flight control: the antennae, trichoid sensilla, and campaniform sensilla. Our decision to focus on the trichoid sensilla reflects the relative paucity of papers dedicated to their study, particularly alongside the compound eyes and antennae. There has also been a recent focus from other research groups on the campaniform sensilla, e.g. [106-109]. This stands in contrast to the trichoid sensilla, where the majority of the previous literature is from the 1940s–1970s. Since then, innovations in the area of anatomical and flow imaging allow

considerably more precise and quantifiable study, warranting an up-to-date analysis of these important structures.

The existing literature leaves several questions unanswered: we are yet to understand the exact flow stimuli these hairs are likely to receive, and there is a disparity in the previous attempts to classify the directional sensitivity of the hairs. In a broader flight control context, we cannot say anything more specific about the exact function of the trichoid sensilla other than to say they can detect deviations from straight flight. If we are to understand how multi-modal information is integrated, it is vital we characterise each of the inputs to the system, of which the trichoid sensilla are a key component.

From the perspective of engineers looking to mimic these biological systems, we have provided an overview of a potential model for using information on aerodynamic flows and loads to account for unsteady aerodynamics by defining additional state variables. However, exactly what variables should be used to define the aerodynamic state that we are trying to measure? And how should this information then be used to alter the kinematic state of the body or flight apparatus? A corollary of these questions is to ask how sensors should be placed on the body or wing, and in what arrangement and numbers.

The current gaps in our knowledge lead us to three overarching questions to pursue in this thesis, using the desert locust as a model species:

What aerodynamic features of the flow could the cephalic hair sensilla be measuring?

How have sensillum position & directional sensitivity been optimised to monitor features of airflow?

How is this sensory information used in flight control?

Chapter 2 seeks to answer the first question; we attempt to visualise the flow over a scale-model of the locust head using experimental wind tunnel techniques. Chapter 3 extends this work, using computational simulations of the flow to examine the boundary layer flows, following validation of the model using data acquired in Chapter 2. In Chapter 4, we develop

a computed tomography protocol to visualise all the trichoid sensilla on the head of the desert locust and two additional species. These data allow us to quantify the directional sensitivity and arrangement of every individual hair, providing unprecedented mapping of a complete sensor system. In Chapter 5 we combine the flow measurements from Chapter 3 and the sensilla measurements from Chapter 4 to analyse the relationship between sensor and stimulus. We develop a simple model of the response properties of the sensilla neurons based on previous research and discuss the role of these flow sensors in a broader context. In Chapters 6 and 7, we carry out *in vivo* force and moment measurements on tethered flying locusts before and after manipulating sensory input to the trichoid sensilla. These measurements allow us to compare the flight performance across manipulations and to characterise the locust's dynamic flight stability.

Our approach covers both ends of the sensory chain: we want to establish the stimulus to the hairs and how they are optimised to respond to this, but also the resulting effects on the locust's flight dynamics. We believe this mixture of physiological and behavioural study provides an in-depth and informative analysis of this sensory system.

Chapter 2

Flow over the locust head: an experimental approach

2.1 Introduction

The complexity in the study of flight dynamics stems from the inherent coupling of a body's dynamics with the fluid dynamics of the surrounding air. We face a similar challenge in scrutinising the trichoid sensilla: we need to understand the airflow they are experiencing, as well as their own physical properties, before we can infer their role and optimisation in flight control. In this chapter we seek to reveal the airflow to the sensilla, thereby addressing the first of our research questions posed in the Introduction: *What aerodynamic features of the flow could these sensors be measuring?* We employ an experimental approach by 3D printing a model of the desert locust head and using particle image velocimetry in a wind tunnel to visualise airflows around it. We quantify the flow with the head oriented at a range of angles of attack and sideslip ($-6° \leq \alpha \leq 14°$ and $-6° \leq \beta \leq 6°$) to simulate small disturbances from the equilibrium flight condition of free-flying locusts. We detail our methods and analyse the changes in airflow over the areas of trichoid sensilla under these varying head positions.

2.2 How can we visualise flows?

Simulations of mechanical and physical phenomena are commonplace, including for fluid-solid interactions, but there are still advantages to experimental methods. While computational fluid dynamics (CFD) simulations are generally considered to be fully reliable for many steady flow conditions, some care needs to be taken with the transitional flows of the kind flying locusts likely experience. Experimental techniques offer a valuable source of validation for these conditions, while also providing measurement of real (rather than simulated) flow phenomena.

There are many experimental techniques to visualise airflows. Of the qualitative methods, perhaps the best known is smoke visualisation. The technique is long-established and remains heavily used, providing informative flow analysis with often minimal setup or processing requirement, once the facility is in place. One advantage of smoke is that it can easily be seeded throughout a whole experimental body of air, giving an overview of flow patterns in both the near and far fields. The method is highly scalable and has been widely used in biological flight studies. Several research groups have used it to explore the aerodynamics of insect flight (Figure 15), for example, analysing leading-edge vortices on the wings of hawk moths [110], butterflies [2], dragonflies [111], and bumblebees [112]. Smoke is particularly well-suited to capture the time-periodic effects such as vortex shedding that are both prevalent and important in insect flight. There are, however, limitations to the technique – analysis is qualitative and requires interpretation, and the streaks represent a summed time history of the flow, as opposed to the instantaneous flow field (i.e. they show time-integrated path lines) [113].



Figure 15: Desert locust smoke visualisation in a wind tunnel, revealing the flows generated in the wake of the beating wings. (Image courtesy of Dr S. Walker, University of Oxford)

Subsequently, an alternative, quantitative technique, particle image velocimetry (PIV), has become widely used, including for the measurement of flows at the insect scale. PIV has been employed to inspect the wakes and vortices generated by hawk moths [113, 114] desert locusts [115, 116], dragonflies, and damselflies [111]. In all forms of PIV, the fluid is seeded with particles assumed to be near neutrally buoyant and to move faithfully with the fluid. In the simplest case, two-dimensional (2D) PIV, these particles are illuminated by a pulsed thin laser sheet of around 1-3mm in width. The area illuminated by the laser is recorded by a camera approximately normal to the sheet (after initial calibration of the distance between camera and sheet). The camera records two consecutive laser pulses of known time interval, which are subsequently split into a large number of smaller 'interrogation windows'. The displacement of the illuminated particles can then be calculated by cross-correlating the greyscale patterns between the corresponding windows in the two successive images and finding the highest correlation peak. Given knowledge of the time interval between the two frames, these measurements provide a vector of flow velocity [3], and, in concert, produce a complete grid of flow vectors for the captured area.

By using two or more cameras, stereo-PIV can produce three dimensional velocity vectors. In the simplest setup, two cameras and a thin laser sheet can be used to capture the same vector data as 2D PIV, but with the additional out-of-plane flow velocity. This methodology can be extended to capture the flow over an object wider than the laser sheet, simply by moving the position of the imaging plane relative to the test object and recording another image pair. When stacked together, this series of measured planes across the object provides a pseudo-volumetric measurement of the three dimensional flow field. This does not provide an instantaneous snapshot of the 3D flow at a particular instant. However, with steady state flow (when we assume the flow remains uniform over time), this technique is acceptable. Alternatively, the instantaneous 3D volume can be reconstructed by using multiple cameras and photogrammetric techniques in what is known as tomographic PIV [116, 117].

Using PIV for live animal aerodynamic studies finds its roots in Spedding's [118] 10 Hz measurements of the vortex wakes generated by a thrush nightingale. With the rapid advances in both laser and camera technology, we can comfortably measure flows on vastly improved temporal and spatial scales. For example, Henningsson et al. [119] achieved imaging speeds of 2 kHz, giving 1 kHz PIV, when investigating the wakes of desert locusts using large-volume tomographic PIV. With well-established methodologies to use PIV for insect-scale studies, we chose to employ the technique to define the flows around the head. We opted for stereo stacking PIV as opposed to the tomographic approach as data acquisition is quicker, more straightforward, and we assume steady, uniform flow at this scale and flow speed.

2.3 Methods

Creating a physical model

Although we could have used a real locust head, we chose to produce a 3D-printed scale model in order to resolve a larger number of flow vectors close to the head surface.

Producing an artificial model also removed the risk of tissue desiccation causing deformations in the head capsule over time, as well as potentially reducing reflections of the laser on the cuticle. The limits on achievable resolution vary hugely between different types of 3D printers, but relatively inexpensive benchtop digital light processing printers are capable of resolutions sub-50 microns in all three dimensions. While this is not high enough to allow printing of such fine structures as the trichoid sensilla, it is sufficient to capture the macro shape of the locust's head capsule.

Computed tomography

Before 3D printing, we required a suitable digital model of a real locust head. Several techniques exist for acquiring high-resolution, non-destructive 3D geometry of such a structure, including photogrammetry, confocal microscopy, and X-ray micro computed tomography (XMT, or μCT). XMT was chosen as it offers an excellent balance of simplicity, acquisition speed, and resolution. The basic theory of XMT is deceptively simple: X-rays produced from an electronic source pass through the sample under scrutiny and are recorded by a planar X-ray detector on the other side, creating a radiograph (or projection image). The sample is rotated by some small amount (typically less than one degree) and another projection image is recorded. This process is repeated until the sample has been rotated through 180° or 360°. Absorption of X-rays will vary depending on the properties of the material, and thus the number of photons reaching the detector will differ across the sensor. The resulting projection images are reconstructed to produce thin image cross sections (tomograms) that, when stacked together, produce a complete 3D model of the sample.

We used a XMT scanner within the University of Oxford at the Henry Wellcome centre for Molecular Physiology. The scanner, a SkyScan 1172F (Bruker MicroCT, Kontich, Belgium), is capable of a nominal scanning resolution of less than 1 micron - sufficient to accurately capture the shape of the locust head (measuring approximately 0.5 cm in each dimension). The scanner uses a cone-beam X-ray source, i.e. the rays are emitted in 3D in a cone pattern

and picked up by a 2D detector. This beam arrangement offers significant speed advantage over alternative fan beam sources (which produce a coplanar (2D) fan of X-rays) by sampling a much larger area in a single projection. The achievable resolution depends upon the size of the sample. Proximity of the sample to the source increases the resolution, thus a smaller sample can be scanned with a higher resolution. In order to achieve the best resolution for the head, the head was removed from the rest of the locust body, leaving just the head capsule and prothorax (Figure 16).

We scanned three individual desert locust head and prothorax sections (from Livefoods, Rooks Bridge, UK) with the tungsten target X-ray source set to 29 kV and 167 μA. The size of the samples allowed for a 3.53 μm image pixel size while keeping the whole sample within the 4000 x 2672 camera sensor. The samples were rotated through 180° in 0.25° increments, with 4x frame averaging (four frames were recorded at each angular position), and 2 second exposures per projection, giving a total scan time of approximately 9 hours. We reconstructed the complete set of projections into 2D image slices using Bruker's proprietary NRecon software (v1.6.9) which utilises the Feldkamp cone beam reconstruction algorithm [120]. The only additional reconstruction parameters used were ring artefact reduction and 40% beam-hardening correction. By stacking the 2D slices together, we generated 3D visualisations, such as Figure 16.

3D printing

Using the XMT data, we produced a model suitable for 3D printing. The *de facto* standard for 3D printed models has become STL (stereolithography) files, which are triangulated definitions of the surface of an object, consisting of vertices and an index of integers defining the order these vertices are connected to form each triangle. However, in order to retain the tomographic, slice structure of our data, we used a lesser-known and used file format, SLC (standing for SLiCe). This format consists of stacked 2D slices, with each slice specified as a line of points defining the boundary between the inside and outside of the model. Using this format was sensible not only for retaining the structure of the data, but because many 3D

printers (including the one used) work by progressively producing their models in 2D slices.

The model was created by an external contractor (Esotechnic, Oxford, UK) using their own custom software to process the CT data (received from us as the set of tomograms), produce the binary SLC file, and 3D print the file on a B9Creator printer (a 3D printer that uses a UV light to 'fix' (solidify) a resin. (B9Creations LLC, SD 57701)). The head model was scaled up by a factor of four, allowing a more favourable compromise between capturing the wide field flow around the model while attaining a high resolution in the boundary layer. The hairs themselves were too fine to resolve from our CT scan and to print.

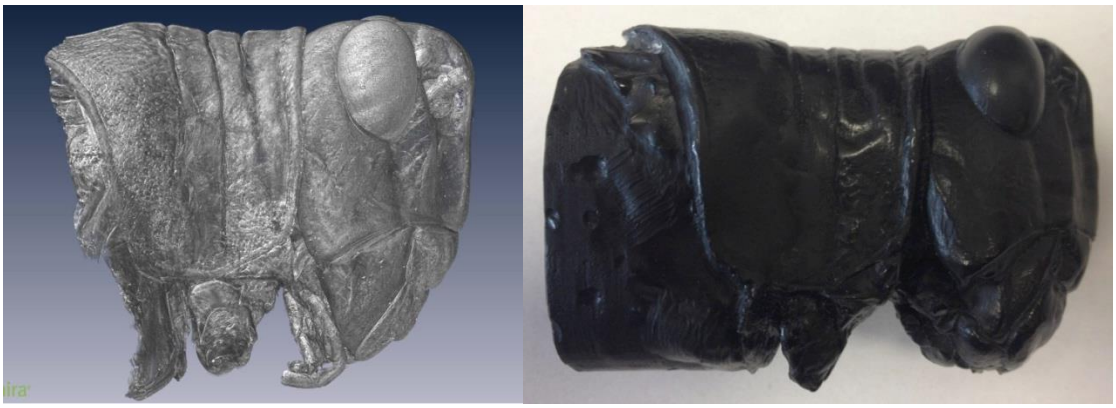


Figure 16: Left: XMT scan of a locust head, showing the remaining head and prothorax regions after dissection. Right: Model produced using a DLP 3D printer. A 'plug' section was added to the rear to provide a flat mounting point.

Particle Image Velocimetry

With the model produced, we sought to describe the likely aeromechanical sensory cues each hair field would be receiving. We recorded PIV measurements with the head in a range of positions representative of possible small disturbances from equilibrium forward flight. In order to simulate these scenarios, we rotated the head through a number of angles of attack and sideslip. Angle of attack, α, refers to the angle about the pitch axis between the oncoming airflow and some reference line on the body (often the longitudinal axis), while sideslip angle, β, is the yaw of the body from the relative airflow (it is the lateral angle of

attack). For our experiments, we define the angle of attack as the angle of the head relative to oncoming airflow in the pitch axis. While sideslip angle is the angle of the head relative to oncoming airflow in the yaw axis (Figure 17).

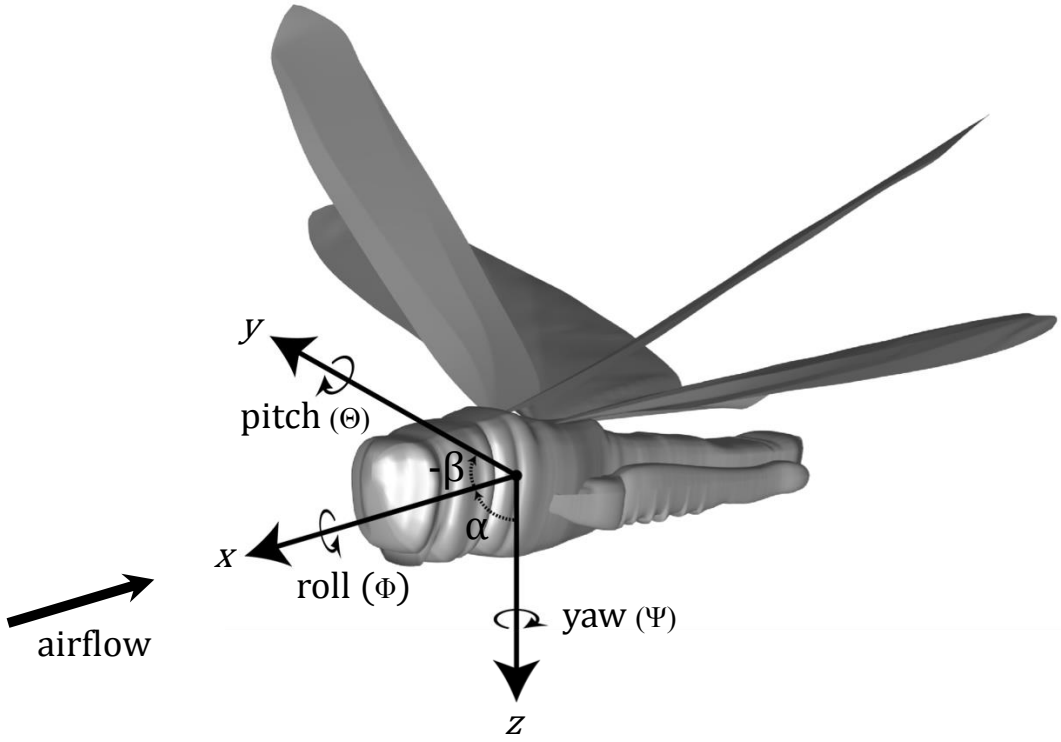


Figure 17: Axis system. Angle of attack refers to the orientation of the head relative to airflow about the pitch axis, and sideslip angle, about the yaw axis. (Locust geometry courtesy of Dr S. Walker, University of Oxford)

We utilised our wind tunnel optimised for consistent low-speed flows appropriate for insect-scale aerodynamic study [111-116, 121-123].

The head was mounted on a custom sting mount allowing adjustment of α and β and horizontal traversing. During steady, forward flight, the locust holds its head at about -2° angle of attack and 0° sideslip (based upon our wind tunnel observations and [124], see Figure 18), which we define as the equilibrium or reference flight condition. We chose a range of α and β angles to represent deviations about this equilibrium value to simulate varying head orientation (with respect to the oncoming airflow). The angles were $-6° \leq \alpha \leq 14°$ and $-6° \leq \beta \leq 6°$, in 2° intervals and were selected based on free-flight data [125, 126]. The method of generating small 'disturbances' about the equilibrium flight condition is

common in engineering studies of flight dynamics [127] and we use this approach in later chapters to characterise the dynamic stability of the locusts.

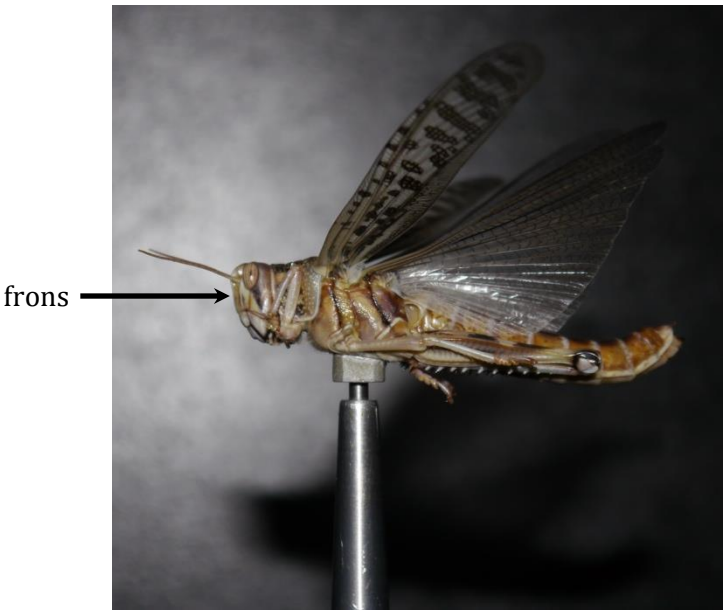


Figure 18: Locust in full flight posture. Although the thorax is held at an average angle of 7° (in the pitch axis, relative to the oncoming airflow) during steady forward flight, the head is held approximately perpendicular to the oncoming airflow (using the frons as the point of reference). We take 0° angle of attack as when the frons is held perpendicular to the oncoming airflow; the sideslip angle of 0° as when the locust's sagittal plane is parallel with the oncoming airflow.

Air tunnel flow speed was set to 0.825 ms^{-1}, four times less than the 3.3 ms^{-1} equilibrium (preferred) flight speed of locusts [121]. This decrease was necessary to account for the consequences of scaling the head, in terms of how we expect the air to behave relative to the *in vivo* locust head. By decreasing by a factor of four, the Reynolds number (*Re*) is kept constant. This dimensionless number defines the ratio of inertial to viscous forces, and the relative importance of these two quantities for given flow conditions. It provides a description of how the flow acts, based on velocity, a characteristic length of the object it is interacting with, and the kinematic viscosity of the fluid. This relationship is represented by the simple ratio:

$$Re = \frac{Ul}{v}$$

Where $U = velocity$, $l = length$, $v = kinematic\ viscosity$. The Reynolds number of the locust head and scale model at their respective flow speeds is approximately 1,000, based on the head width.

We used stereo high-speed PIV to measure the airflow in the wind tunnel test section 1.0 x 0.5 x 0.5 m. A vertical light sheet was generated in the centre of the test section with a 10 mJ pulsed laser (Nd:YLF, 527nm, Litron LDY-300PIV; Litron Lasers Ltd, UK) guided by a custom rig of three 45° mirrors and a 10 mm plano-cylindrical lens (focal length of 75 mm) (Figure 19). The resulting sheet had a thickness of 0.5 mm and provided an imaging area of around 100 x 100 mm^2. Near neutrally buoyant smoke particles were produced from olive oil in a compressed air particle generator (LaVision GmbH, Germany). The generator was situated upstream of the inlet fans and therefore the smoke travelled through the whole wind tunnel before reaching the test section, ensuring uniform dispersal.

The laser sheet was recorded using two high-speed CMOS cameras (Photron SA3, 1024 x 1024 px, 2000 fps, Photron Ltd, Bucks, UK) equipped with 50 mm lenses (AF Nikkor 50 mm, *f*/1.8) and situated perpendicular to the laser sheet. Trigger control, camera calibration (using a 105 x 105 mm calibration plate), and all data acquisition were done through the software package DaVis (ver. 8). The cameras and pulsed laser were synchronised using a high-speed controller (LaVision GmbH, Germany) and the pulse separation interval was set to 480 μs for the freestream airflow velocity of 0.825 ms^{-1}, giving a mean particle displacement of approximately five pixels (Figure 19).

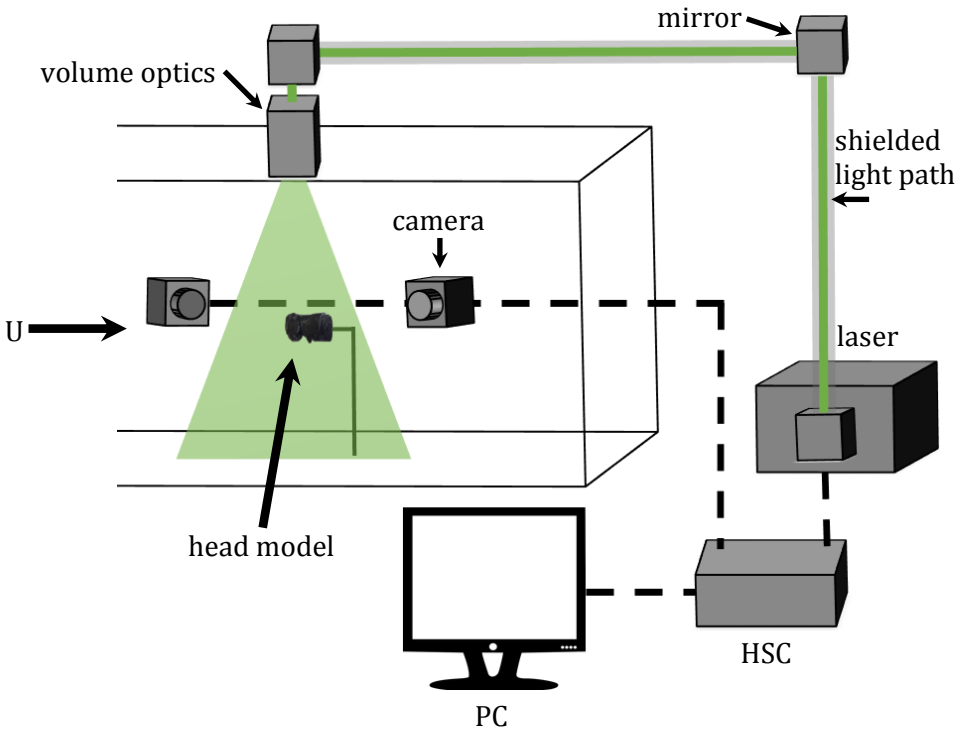


Figure 19: Wind tunnel PIV schematic showing position of the sting-mounted 3D model, direction of airflow (U), cameras, beam delivery, and laser sheet. The cameras and laser were synchronised using a high-speed controller (HSC).

We sampled 25 planes across the model at intervals of 1 mm starting from the sagittal plane and working outwards on one side. Only a single side of the model was sampled as we reasonably assumed the head to be symmetric in the sagittal plane. At each 1 mm interval, the flow was sampled 500 times (i.e. 500 image pairs) at 1 kHz to allow temporal averaging.

Vector fields were calculated from the image pairs in DaVis 8 using multi-pass stereo cross-correlation stitching, starting with interrogation windows sized 32 x 32 (equally sized windows across each image) then reducing to 16 x 16 and 8 x 8. This yielded vector maps of 128 x 128 vectors within an imaging area of 54 x 54 mm^2, corresponding to a resolution of 0.42 x 0.42 mm^2. We used a custom MATLAB program to mask out the erroneous data in the head model area by defining a boundary using the reflection of the laser off the surface of the head. Vectors affected by, or within, this boundary were then removed, leaving just the flow data around the head. Stacking the processed vector fields produced the final pseudo-volumetric 3D visualisation of the flow.

2.4 Results and discussion

Although we could display the entire set of 3D vector fields recorded at each point along the head, for clarity, Figure 20 and Figure 21 show single vector fields along the head's sagittal and transverse planes respectively. While Figure 20 represents a temporal average of a single stereo-PIV sequence taken at a fixed position on the head, Figure 21 is a cut-through of all 25 planes sampled non-simultaneously across the head.

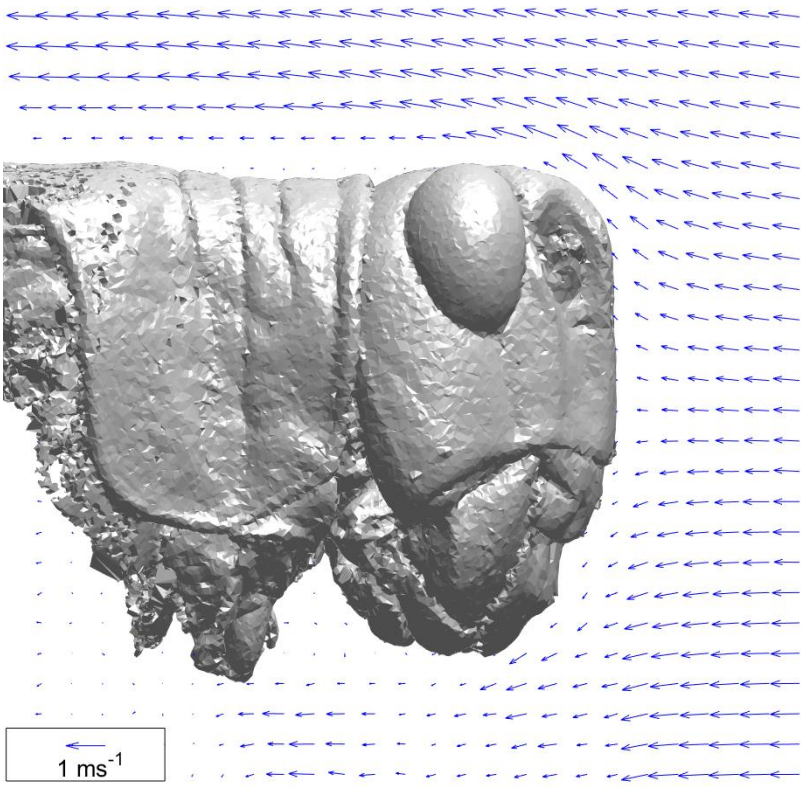


Figure 20: Visualisation of a single PIV vector field (one of 25) with simulated position of the locust head model. This plane was sampled at the sagittal plane of the model. A subsample of the data is shown for clarity (every fifth vector of the 128 x 128 grid). Vectors are scaled by their relative magnitude (airspeed).

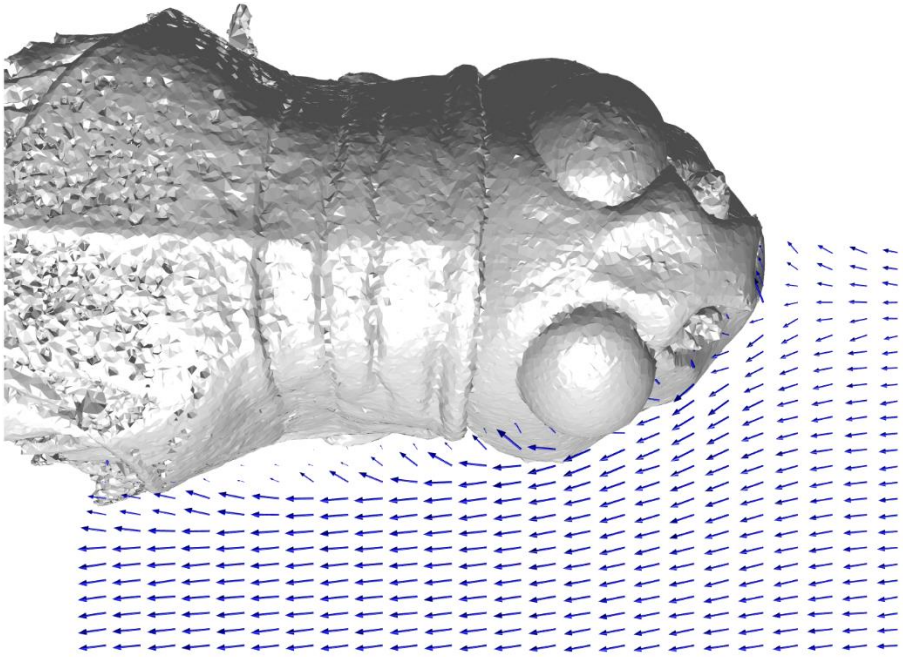


Figure 21: Vector field in the transverse plane, produced by sampling through all 25 unique planes of PIV data. A subsample of the data is shown for clarity (every fifth vector of the 128 x 128 grid).

In Figure 20 the pattern is very clear: flow slows as it approaches the front of the head, forming a stagnation point, and either flows over or under the model. Focussing on the flow above the head (where the trichoid sensilla are present), the flow initially accelerates as it is forced around the head. Vectors are smaller closer to the surface, indicating a characteristic boundary layer behaviour. Figure 21 illustrates the same stagnation points, flow acceleration, and boundary layer gradients in the transverse plane.

Using the complete set of 3D vector fields, we mapped the stagnation point of the flow at each angle of attack and sideslip (Figure 22). The figure illustrates the central position of this point at zero degrees angle of attack and sideslip and its movement as the head was rotated through the range of angles. The stagnation point shifted in a linear and predictable fashion.

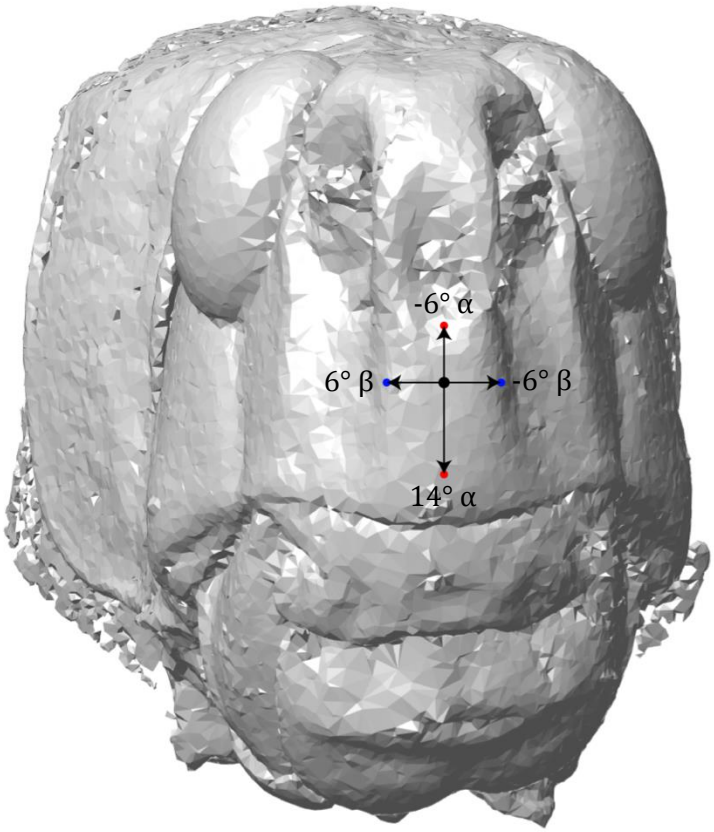


Figure 22: Flow stagnation points. The black dot represents the stagnation point (in both horizontal and vertical axes) at 0° α and β. Arrows show the direction of movement of the point through the range of head angles. Coloured dots (red = α, blue = β) represent the stagnation points at the extreme angles of attack (-6° and 14°) and sideslip (-6° and 6°).

In this study, the regions of flow that we are most interested in are those over the fields of trichoid sensilla. The five fields presented in Figure 23 are based on Weis-Fogh's original drawings [24, 27], those of Smola [23], and the few hairs visible on the XMT scan.

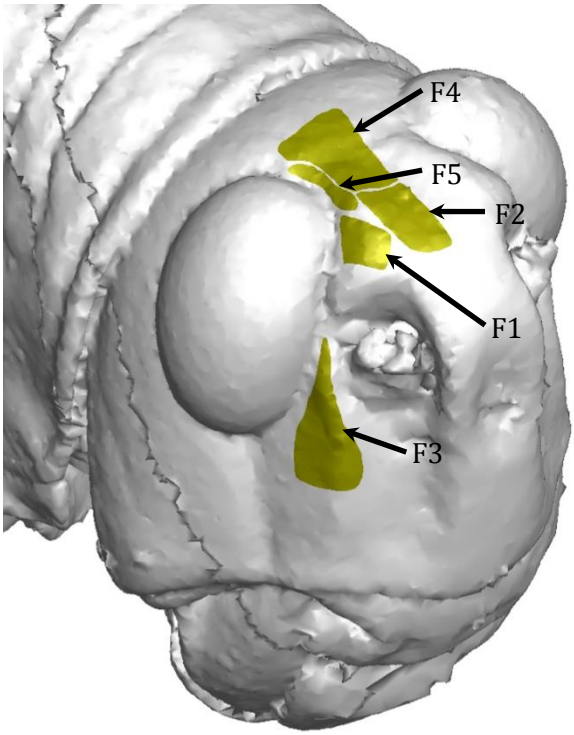


Figure 23: The five fields of trichoid sensilla, re-drawn after Weis-Fogh [24, 27], Smola [23], and XMT observations.

Flow data over the fields were extracted by searching for vectors at a chosen distance above the surface (using the mean normal of the polygons defining the field surfaces to provide a direction).

Figure 24 plots the mean airflow vectors for each hair field, on a single side of the head at a distance of 2 mm above the surface. As the head model was scaled up by a factor of four, 2 mm is equivalent to 500 µm above the surface *in vivo* - slightly beyond the length of the longest trichoid sensilla (350 µm, [23]), although we expect flow direction to be reasonably consistent over these small distances. We were unable to resolve reliable flow data closer to the surface as the laser used to illuminate the smoke particles created significant surface glare on the head model (Figure 25). This glare prevented the cameras from accurately capturing the seeded particles near the head surface and, as a result, flow vectors could not be visualised deep inside the boundary zone where the trichoid sensilla are present. Examination of the flow increasingly close to the head surface revealed greater erraticism relative to neighbouring vectors than would be expected with the low Reynolds number

airflow used in this experiment, likely indicating glare has affected the measurement. Glare varied depending on the position of the laser plane on the head and therefore was difficult to characterise and control.

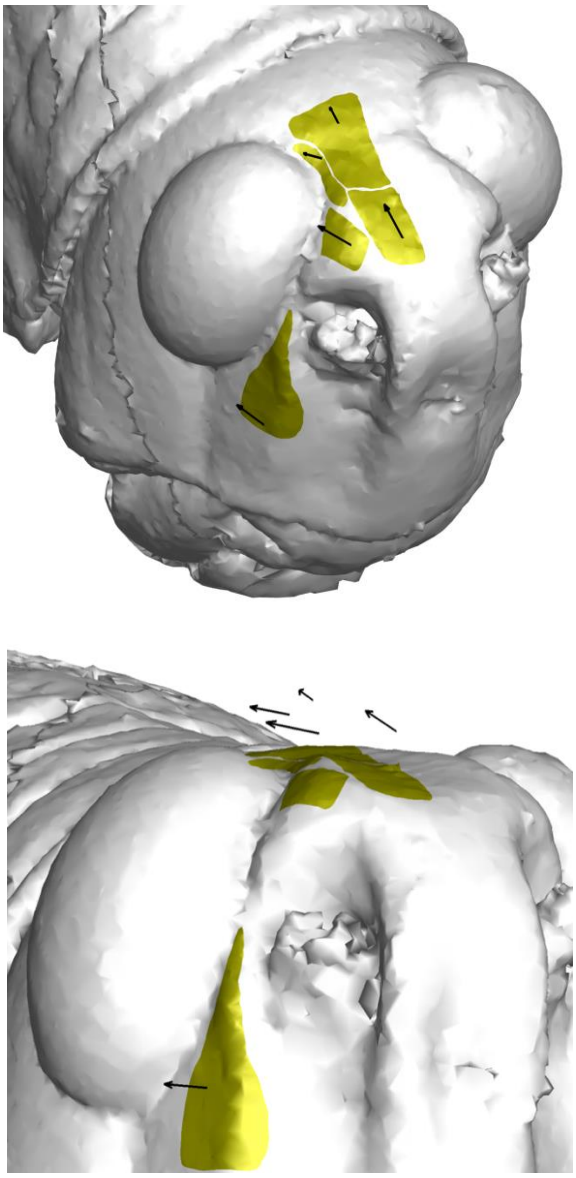


Figure 24: Mean flow vectors over each hair field, on one side of the head, at a distance of 2 mm above the head surface. Top: Dorsolateral view. Bottom: Anterolateral view.



Figure 25: Glare from the laser obscured reliable flow calculations very close to the head surface.

Despite not being able to resolve flows further down in the boundary layer, the data provide an excellent quantitative description of the flow field round the head, showing several key aerodynamic features. For example, boundary layer separation is clearly visible when viewing individual vector planes at differing pitch angles (Figure 26): at $\alpha = 14^{\circ}$, flow has separated from the front of the head, as indicated by the low speed (note the relative vector magnitude), recirculating flow. In contrast at $\alpha = -6^{\circ}$ the boundary layer remains attached and flow runs smoothly along the top of the head.

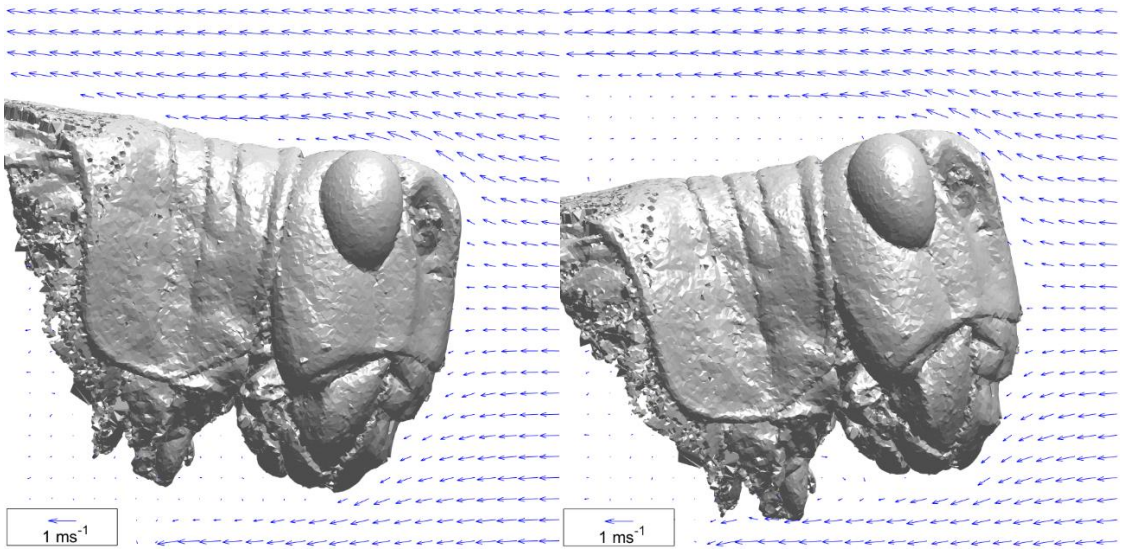


Figure 26: Sagittal plane of vectors at -6° (left) and 14° (right) angles of attack. Flow separation is evident when the head is at 14° α by the relative size of flow vectors.

Inspection of the vector data at each angle of attack revealed that flow separation began at 6° *α*. By mapping the separation point at each subsequent angle up to the maximum of 14°, we can illustrate how this point moved (Figure 27). These observations enable us to hypothesise about the possible roles of different fields of sensilla.

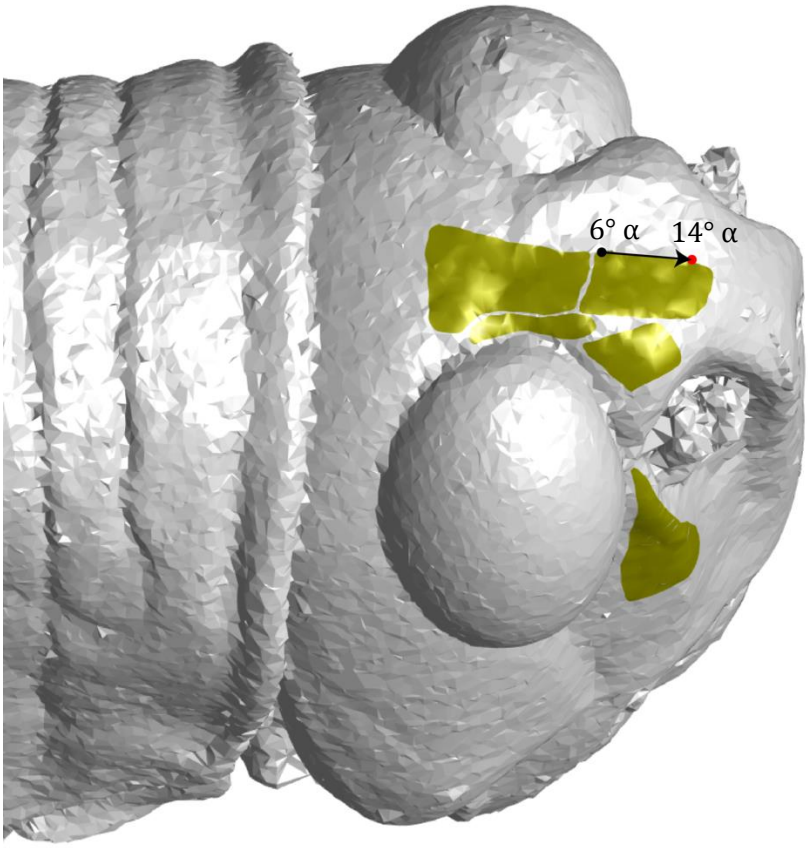


Figure 27: Flow separation points. The black dot shows the point of separation at 6° angle of attack. The arrow shows how this point shifts as α increases up to the top value of 14° (red dot).

The figure demonstrates that, even at 6° angles of attack, the sensilla further back on the head (F4 and F5) will not be receiving significant oncoming airflow. Instead, they will largely be receiving the slowly recirculating air resulting from boundary layer separation. F4 and F5 may therefore act as sensors of extreme angles of attack (and thus possibly indicate stall) if their response properties change at the high angles of attack. In contrast, F1 and F2 hairs seem likely to be receiving relatively constant airspeed flows at the range of angles explored (even at the maximum 14° α the hairs at the front may receive some oncoming flow stimulus) and so may provide a more constant measure of oncoming airflow. F3 is the only field on the vertical plane, and therefore the flow it receives is not susceptible to separation caused by high angle of attack. As a result, F3 in particular may be well placed to provide a consistent measure of attack angle.

Our range of sideslip angles was not large enough to cause flow separation in the yaw axis. However, if separation did occur at higher sideslip angles, F3 could provide a similar role as we have suggested for F4 and F5, but for sensing extreme sideslip conditions.

2.5 Conclusion

In this chapter, we successfully demonstrated experimental flow visualisation around a 3D printed scale model of a locust head using stereo-PIV. The data obtained provide valuable information on features such as flow separation points and stagnation points, revealing the effects of the locust head geometry on local airflows. This information is crucial in answering our questions about the role of the trichoid sensilla, and we have begun to theorise about the possible distinct roles for different fields. In order to obtain details of the flow within the boundary layer into which the trichoid sensilla protrude, we use a computational approach in the next chapter to calculate the predicted flows. The experimental data gathered in this chapter are vital in validating these simulations.

Chapter 3

Flow over the locust head: a computational approach

3.1 Introduction

The particle image velocimetry data presented in Chapter 2 provided an examination of the gross flow features around the locust head. In order to predict airflows further down in the boundary layer – where PIV is a less appropriate technique - we moved from experimental to simulated methods by using computational fluid dynamics (CFD). In this chapter we detail the construction and solution of the CFD model, an analysis of the airflow in the region of the sensilla at a range of angles of attack and sideslip ($-6° \leq \alpha \leq 14°$ and $-8° \leq \beta \leq 8°$), and examine what features of airflow each area of sensilla could sense.

In a similar fashion to the breaking down of PIV images into interrogation windows, CFD simulates flow conditions by discretising the fluid domain into a grid of cells (known as a mesh). Flow variables are calculated only at these grid points, with variables in other areas determined by interpolation. In 3D simulations, cells are typically tetrahedrals, hexahedrals, or prisms, and grid points can be defined at either the centre of the cell or at its vertices (we use the latter) [128]. CFD simulations aim to solve approximations of the Navier-Stokes

equations; a set of coupled partial differential equations that describe the motion of viscous fluid in terms of velocity, pressure, temperature, and density [129]. There are a variety of methods to solve the equations, the most common being finite difference, finite element, and finite volume. In our simulations we use the finite volume method, which finds a solution such that mass, momentum, and energy are all conserved for each cell. Initial creation of a CFD simulation can be an exacting process, particularly in terms of defining high quality meshes and geometries. However, once established, the technique offers a high degree of flexibility for varying input parameters, as well as the ability to extract variables beyond just flow speed and direction, such as pressure or shear. CFD is widely used for insect flow studies, including for simulating the aerodynamics of flapping wings [130-132] and to calculate the stability derivatives necessary to analyse dynamic flight stability [133, 134].

3.2 Methods

Mesh generation

Our CFD model consists of two geometries: a region of air and a surface representation of the head (forming a no-slip boundary of the fluid domain). The latter was produced with the same XMT scan data used to print the solid model for PIV in Chapter 2. Despite CFD solvers becoming increasingly robust, the quality of the solid/surface geometry is crucial for a realistic solution. Initial simulations identified problematic shallow angles caused by concave sections around the mouthparts. We manually removed these sections using the commercial software Amira (ver. 5.6, FEI, USA). We also removed the prothorax (the portion posterior to the head) as this section does not contain trichoid sensilla and would greatly increase the complexity and calculation time of the simulation. In order to prevent vortex shedding from the bluff section resulting from the removal of the prothorax, we extruded an ellipsoid posteriorly from the head in MATLAB of approximately the same dimensions as the prothorax. The polygons defining the entire surface were re-meshed

using isotropic vertex placement [135] in Amira to provide consistent surface quality. Twenty rounds of low-pass filter (of curvature variation) smoothing [136] minimised any remaining small geometric features around the antennal bases and mouthparts that could be problematic for the solver. The final product of these subjective manipulations still closely resembled the natural shape of the locust head (Figure 28).

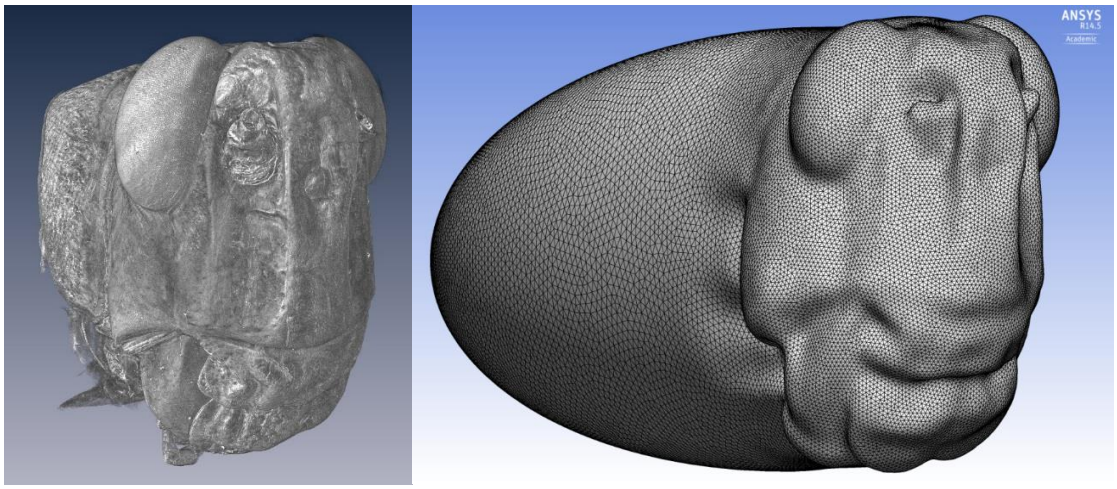


Figure 28: Left: 3D visualisation of a XMT scan of the locust head and prothorax. Right: Final geometry used in the CFD simulation. The prothorax has been removed and replaced by a simpler ellipsoid. Mouthparts have been removed and simplified and the entire geometry has been iteratively smoothed.

Using the commercial software ICEM-CFD (ver. 15, ANSYS Inc., USA) we generated a cuboidal region around the head model (Figure 29) to bound the fluid domain. The cuboid measured 15 x 12 x 12 the size of the model, sufficiently large to eliminate any effects from the walls of the cuboid on the local flow around the head. The head model was placed centrally in X and Y dimensions, but further upstream (towards the flow inlet) than centre in the Z dimension in order to capture as much wake as possible from the head. The wake shows the resulting flow patterns after passing over the complete head model, enabling us to check that our simplified prothorax does not produce any unexpected behaviours.

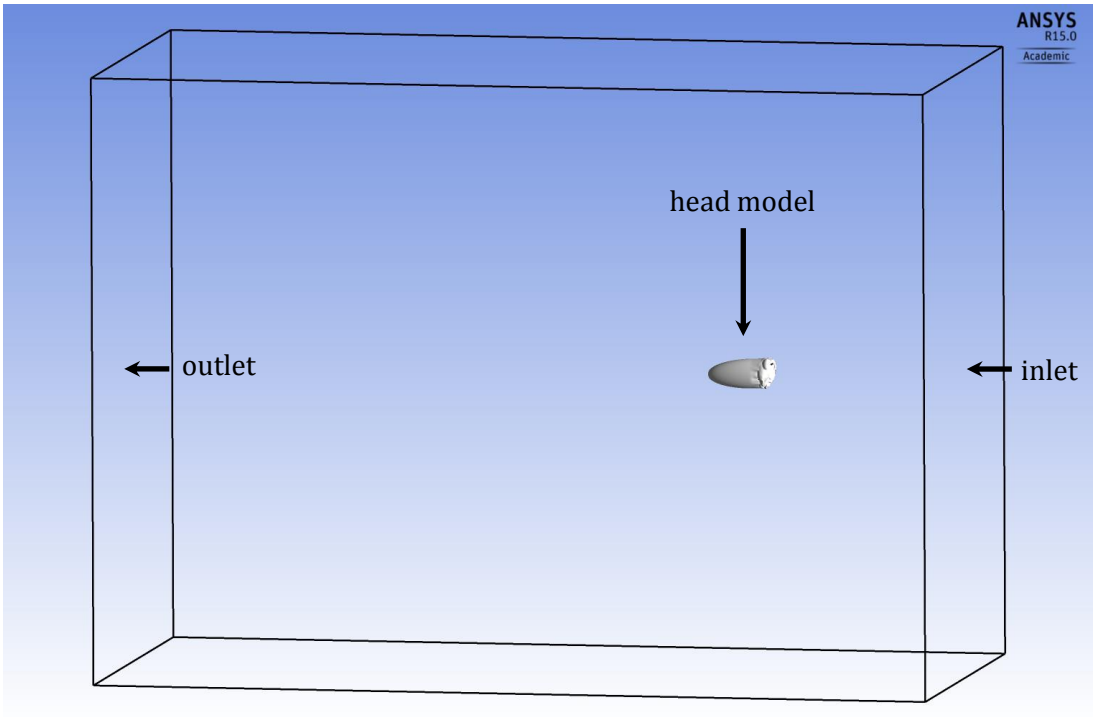


Figure 29: Head model inside cuboidal fluid region, placed centrally in x and y dimensions, but further upstream than centre in z.

The triangulated surface defining the head model was directly converted to a surface mesh for the CFD solver. The boundaries and interior of the cuboid fluid region were meshed with triangulated and unstructured tetrahedral meshes respectively, using an automated procedure in ICEM-CFD.

As discussed in Chapter 2, the boundary layer between a viscous fluid and surface can exhibit steep gradients in flow properties. To capture the boundary layer in fine detail, we inflated three layers of high aspect ratio prisms (each layer 5×10^{-5} m in height), conferring high resolution and effective capture of the boundary layer without incurring excessive (and computationally intensive) stream-wise resolution (Figure 30).

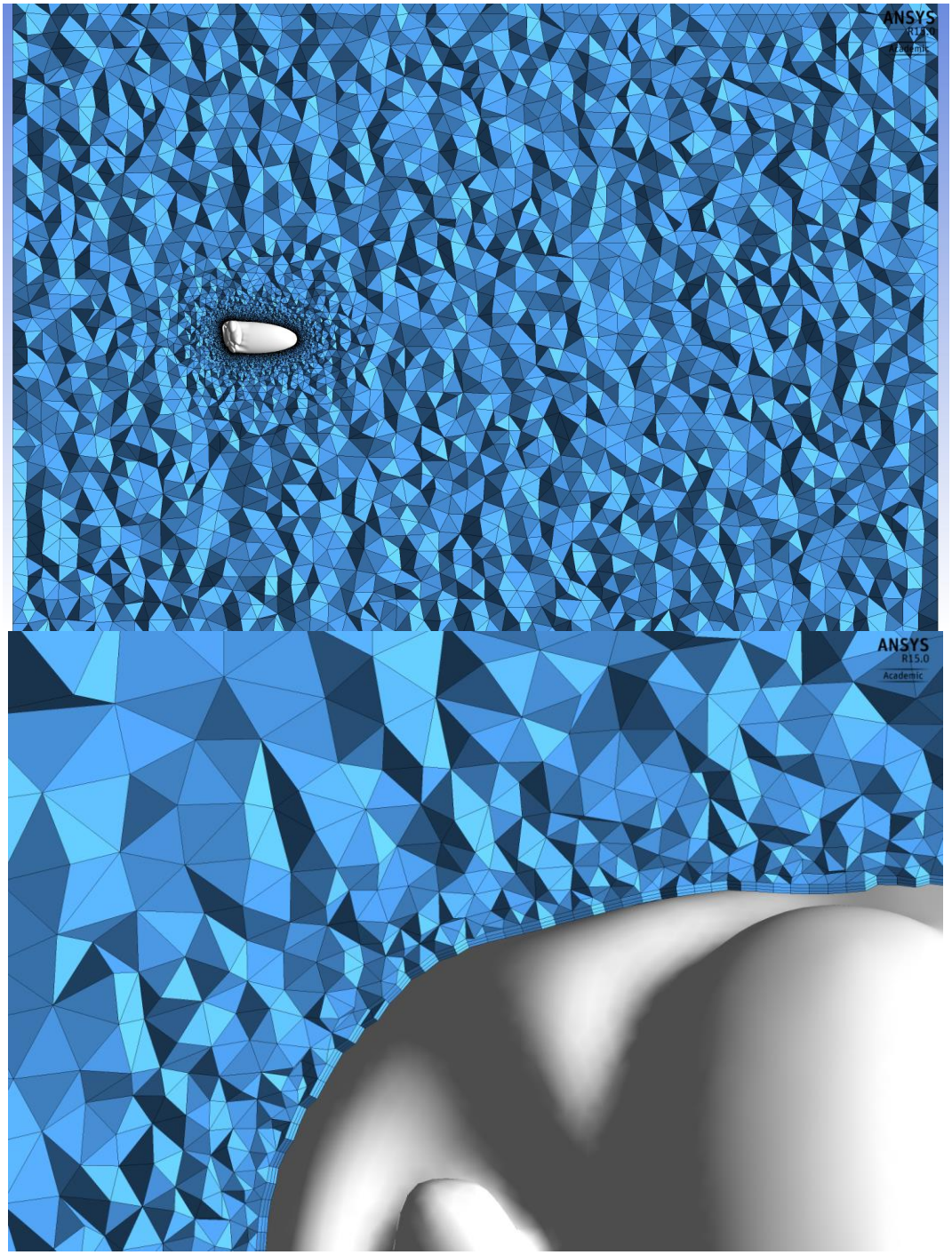


Figure 30: Top: Sagittal plane showing unstructured tetrahedral mesh. Note, cell size decreases closer to the head model in order to capture the steeper gradients in flow properties in the boundary layer. Bottom: Close-up of the boundary layer showing three prism layers at the head surface.

Numerical technique and validation

The unsteady incompressible Navier-Stokes equations were solved using the commercial software package Fluent (ver. 14.5.7, ANSYS Inc., USA), assuming laminar flow. Second-

order spatial discretisations were used, and the pressure-velocity coupling was via the PISO algorithm. Residuals were reduced by at least three orders of magnitude at each time step. Airflow at 3.30 ms^{-1} was allowed to flow for 1 s, using a timestep of 0.0001 s (10,000 timesteps), with a maximum of 40 iterations per timestep (residuals generally converged within 10 iterations).

After the first completed solution, the mesh was validated by comparing coarser (800,000 cells) and more refined (4 million cells) meshes to the default mesh (1.35 million cells). The key comparison was between the refined and default meshes, as it was important that our mesh was suitably fine that further refinement had no significant effect. There were no significant changes in flow properties between all three meshes and therefore we chose the medium mesh as this was generated using default parameters for the given size of the head geometry and fluid region. Validation was also carried out experimentally by comparing the calculated flow fields with the PIV measurements described in Chapter 2. In particular, we verified that the points of flow separation using the two methods matched closely (e.g. Figure 31).

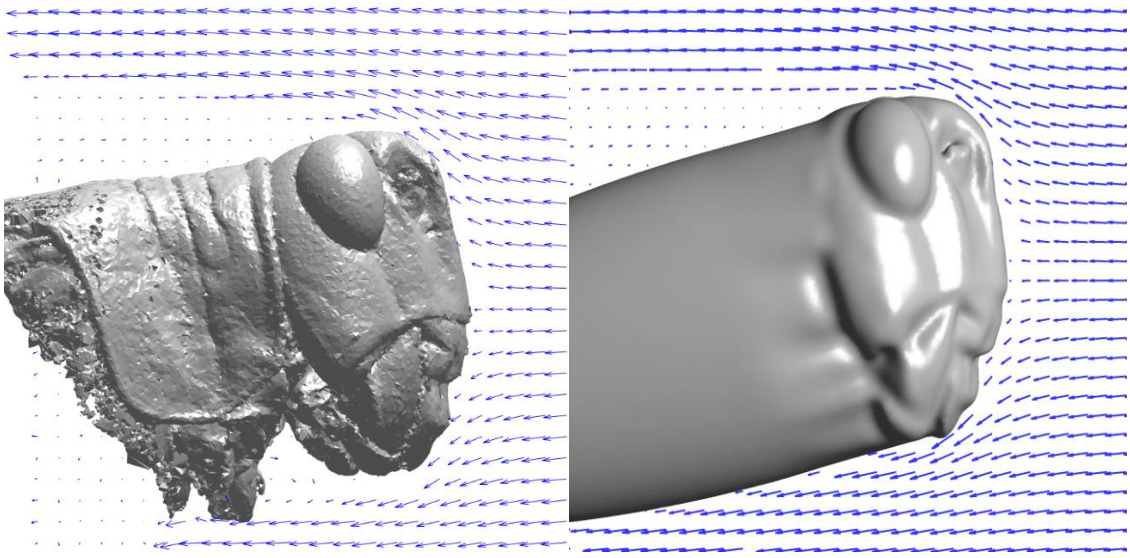


Figure 31: Flow vectors in the sagittal plane from PIV data (left) and CFD simulations (right) at 14° α. Flow patterns are qualitatively similar over the front and top sections of the head, including the points of flow separation, between experimental and simulation techniques. In the region of the mouthparts, which we have simplified in the CFD model, the pattern of separation is different. However, this area is not of interest. Vectors are scaled based on flow speed.

The validated CFD model was used to simulate airflow with the head at a number of different orientations, in the same manner as the PIV experiments (Chapter 2). As CFD allows for rapid changing of geometry orientations, we used a wider range of sideslip angles than with our PIV experiments: $-6° \leq \alpha \leq 14°$ and $-8° \leq \beta \leq 8°$, in 2° increments. As in Chapter 2, angle of attack, α, refers to the angle of the head relative to oncoming airflow in the pitch axis, while sideslip angle, β, is the yaw of the head relative to oncoming airflow (the lateral angle of attack) (see Figure 17). We define 0° angle of attack as when the frons is held perpendicular to the oncoming airflow (see Figure 18) and the sideslip angle of 0° as when the locust's sagittal plane is parallel with the oncoming airflow.

3.3 Results and discussion

Figure 32 displays a sample of flow vectors close to the surface of the head model. A stagnation point (where local flow velocity is zero) can clearly be seen on the centreline of the model. Flow speed gradually increases from this point as the air slips around the sides of the model.

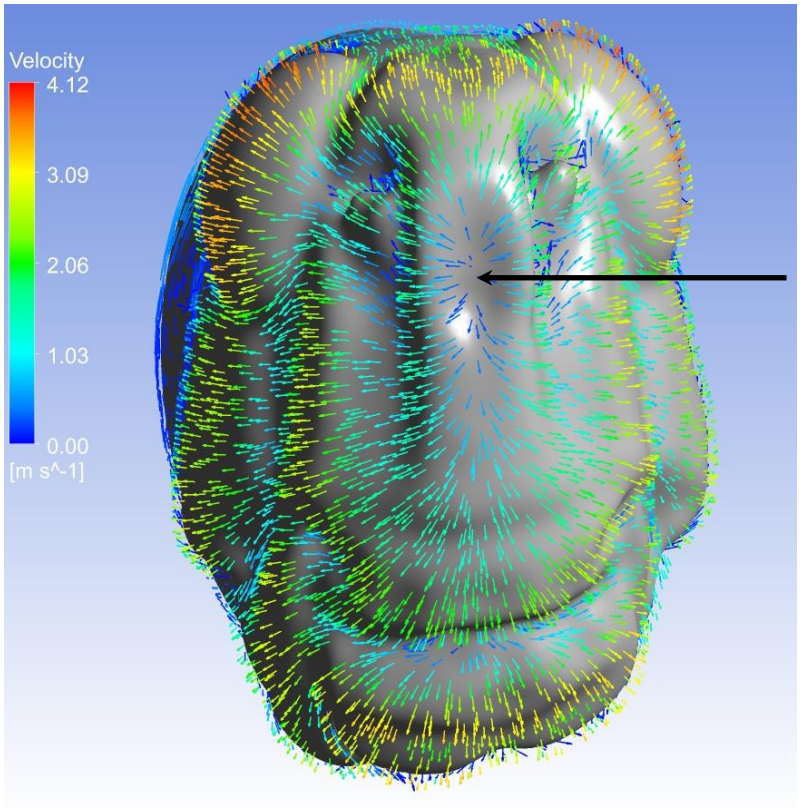


Figure 32: Velocity vectors close to the surface of the head model. A stagnation point is visible on the centreline. Colour signifies flow speed.

A planar view (Figure 33) also clearly illustrates the stagnation point and flow gradients through the boundary layer, as well as the wake flow gradients created as flow sheds from the model. The figure demonstrates that the wake has no influence on the flow over the anterior sections of the head.

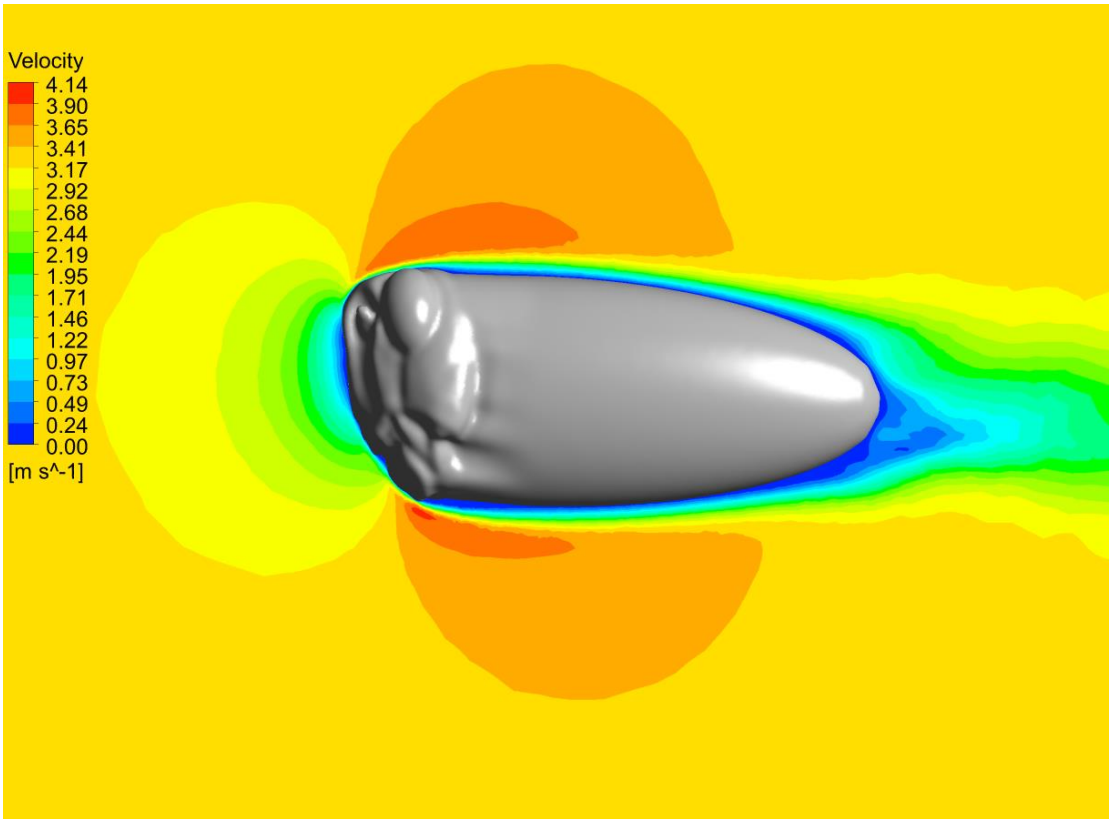


Figure 33: Flow velocity contours around the sagittal plane of the model. Head is oriented at 0° α and β. Note the stagnation point at the front of the head, flow gradients, and growing boundary layer thickness as flow proceeds posteriorly.

The contours around the model in Figure 33 demonstrate the growing height of the boundary layer as flow progresses downstream along the geometry. The common definition for the height of the boundary layer is when it reaches 99% of freestream velocity (3.3 ms^{-1}). We followed this convention while inspecting the boundary flow over the areas of trichoid sensilla (Figure 34). At 0° α and β, we measured an average boundary layer height of approximately 300 µm, with a range of 180 µm to over 450 µm (calculated from regularly spaced sampling over the relevant areas). These values are of the same order of magnitude as the maximum recorded length of trichoid sensilla, 350 µm [23], demonstrating the hairs are potentially responding to flows solely in the boundary layer.

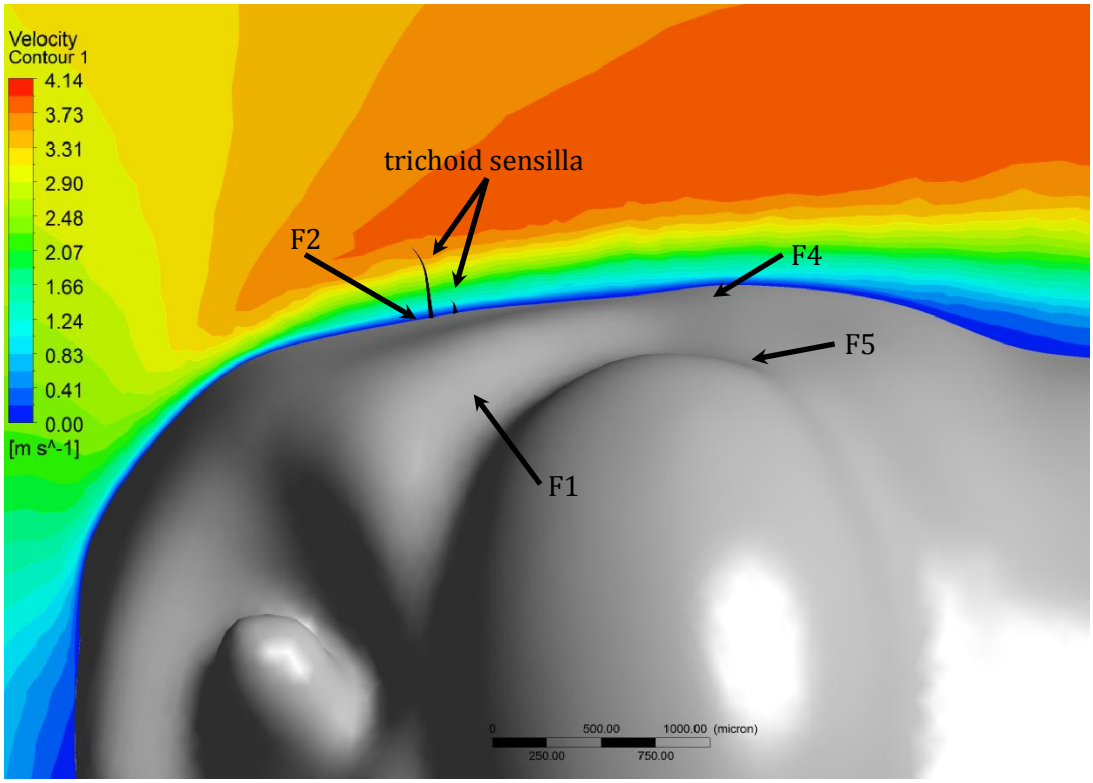


Figure 34: Close-up of the boundary layer over the approximate areas of trichoid sensilla, demonstrating the growth in the height of the layer as the flow progresses along the head. Two trichoid sensilla at the extreme range of heights (50 µm and 350 µm) found by Smola [23] are superimposed for reference. The location of these example hairs would correspond to field F2.

Flow over the trichoid sensilla

In order to scrutinise further the flow over the areas of trichoid sensilla, we redrew the five fields (F1-5) previously defined by Weis-Fogh [24, 27]. Rough sketches of these fields have been drawn for *Schistocerca gregaria* (e.g. [24, 27]), and more accurately for *Locusta migratoria*, the migratory locust [23]. We redefined the fields accurately (improving upon our definitions from Chapter 2) for *S. gregaria* based upon high resolution XMT scan data (see Chapter 4) in which all hairs were visible. Fields are shown and analysed for only one side of the head (Figure 35), as it is reasonably assumed to be symmetrical in the sagittal plane.

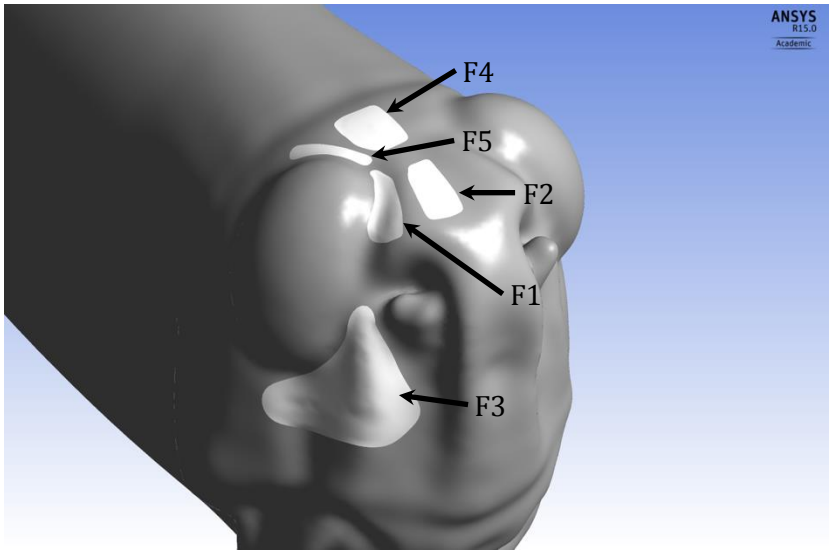


Figure 35: Dorsolateral view of the five fields of trichoid sensilla on the right side of the head, drawn from XMT scans.

We noted that flow direction changed negligibly through the range of trichoid sensilla heights (50 – 350 µm [23], Figure 36), above the surface of the head and therefore opted to extract airflow over the five fields at a distance of 200 µm - the midpoint of this range [23]. Figure 37 displays an example of the flow data across just the five fields at this distance from the head surface.

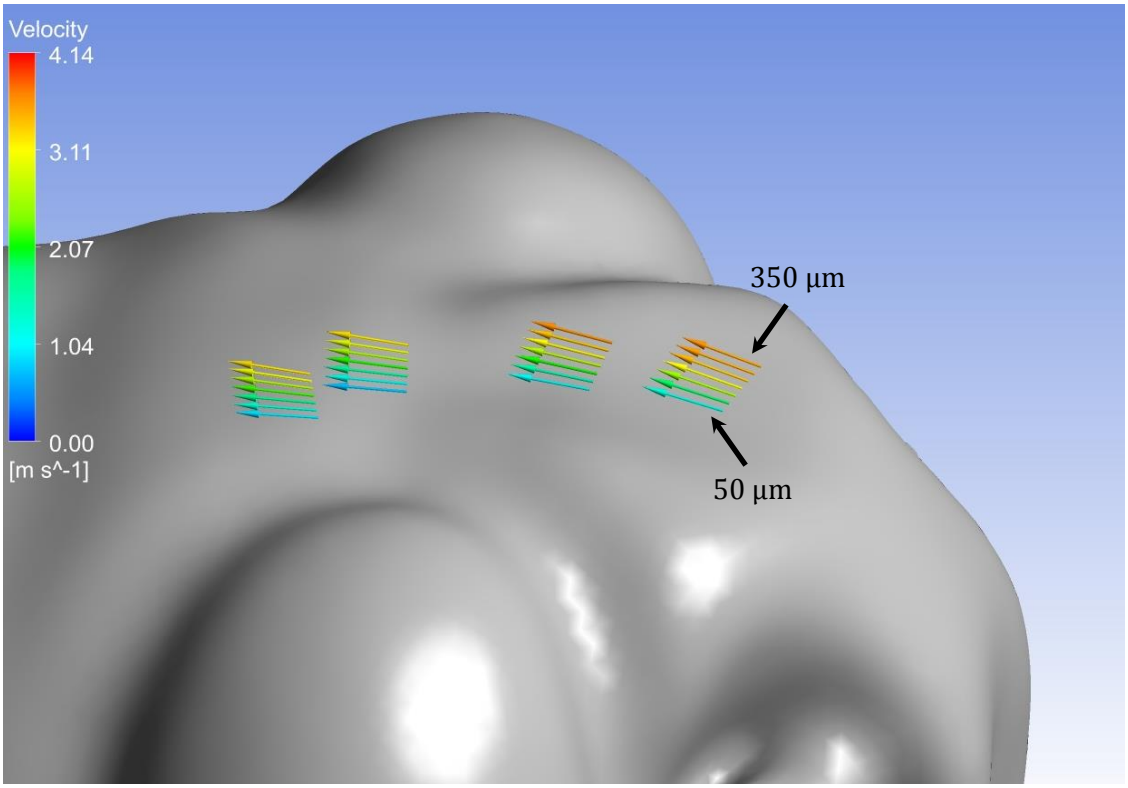


Figure 36: Dorsolateral view of four stacks of flow vectors over the top of the head at distances of 50 – 350 µm above the surface. Note the consistency of flow direction between all heights. The two anterior stacks are over field F2, while the posterior are over F4. The stack locations were randomly generated within each field. Only four stacks are shown here for clarity.

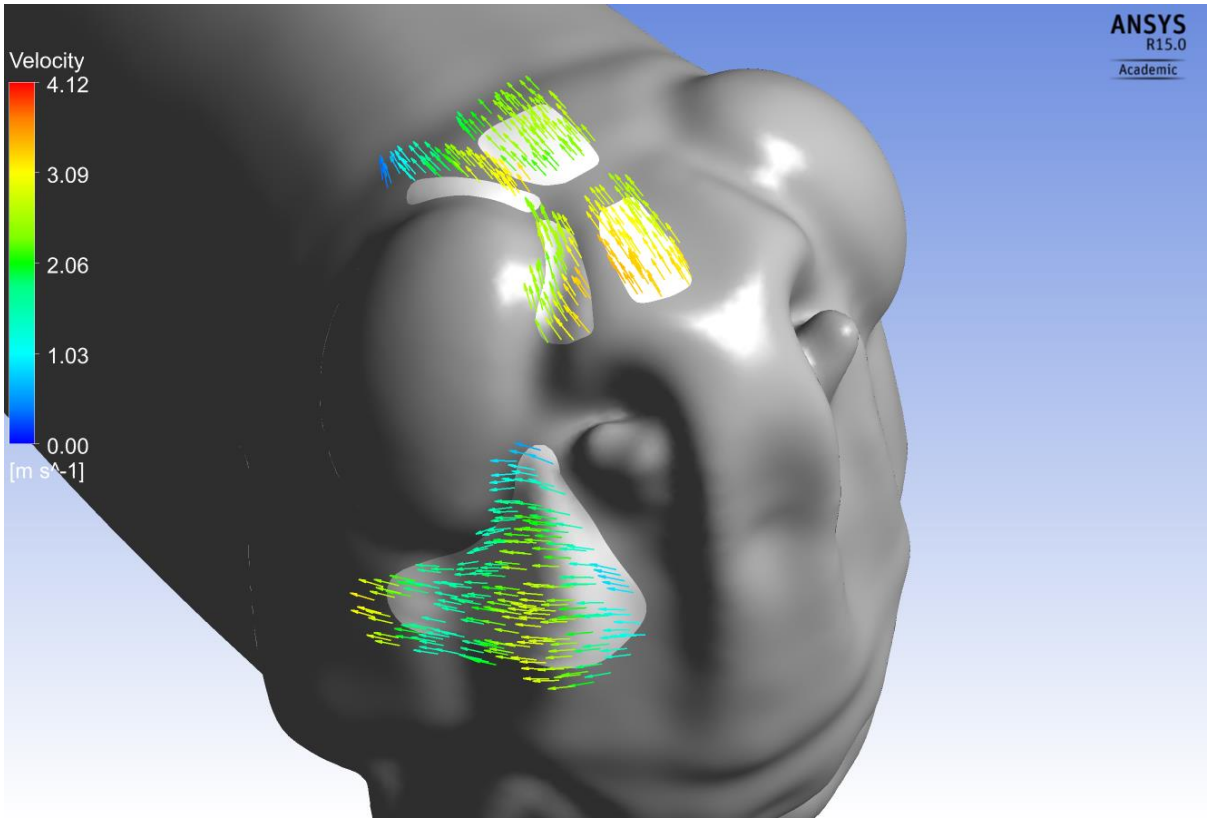


Figure 37: Flow vectors over the five hair fields at 200 microns above the head surface for 0° angle of attack. Note the consistency in vector direction within each field. For clarity, only a sample of the total number of vectors is shown for each field.

The flow direction across an individual field also exhibited minimal variation at any given orientation of the head (e.g. Figure 37). In fields F1, F2, F4, and F5 flow direction was consistent across angles. There was some variation in F3 under changing angle of attack due to the compound eyes causing vectors in the upper section of the field to flow dorsally. However, these vectors represent a small portion of the total number. Therefore, to examine the flow changes induced by varying angle of attack and sideslip, we use solely the mean flow vector within each field at each angle. Plotting the mean flow vectors for all of the head angles on the same figure allowed easy interpretation of the flow changes (Figure 38).

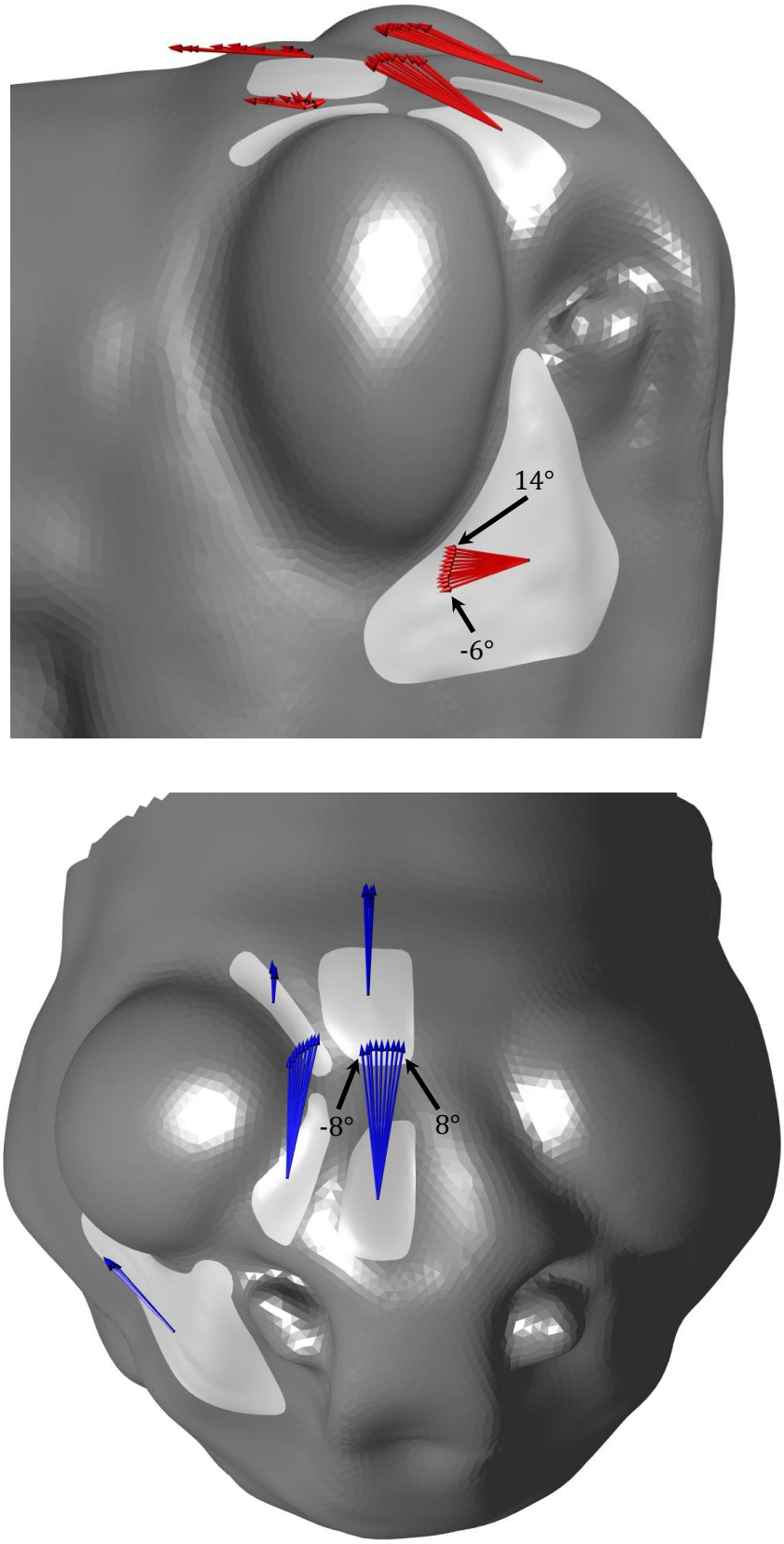


Figure 38: Top: Lateral view of the mean flow vectors over each hair field at each angle of attack (α). Bottom: Dorsal view of the mean flow vectors over each field at each sideslip angle (β). Flow vectors at the extreme angles used are indicated.

Figure 38 reveals interesting differences in the airflow over different fields. Under changing angle of attack, the flow over F1, F2, F4, and F5 varied in magnitude as well as direction. The differences in magnitude are most pronounced over F4 and F5, as demonstrated by the changing vector length. The diminishing magnitude is the result of flow separation at high angles of attack, creating an area of stagnant and recirculating flow over these fields, as illustrated in Figure 39. F1 and F2 also show some change in magnitude but to a lesser degree, while changes in flow direction are evident. F3, which is on a vertical plane, does not experience flow separation under changing angle of attack, hence its flow data displays consistent magnitude vectors and the majority of change in vector direction.

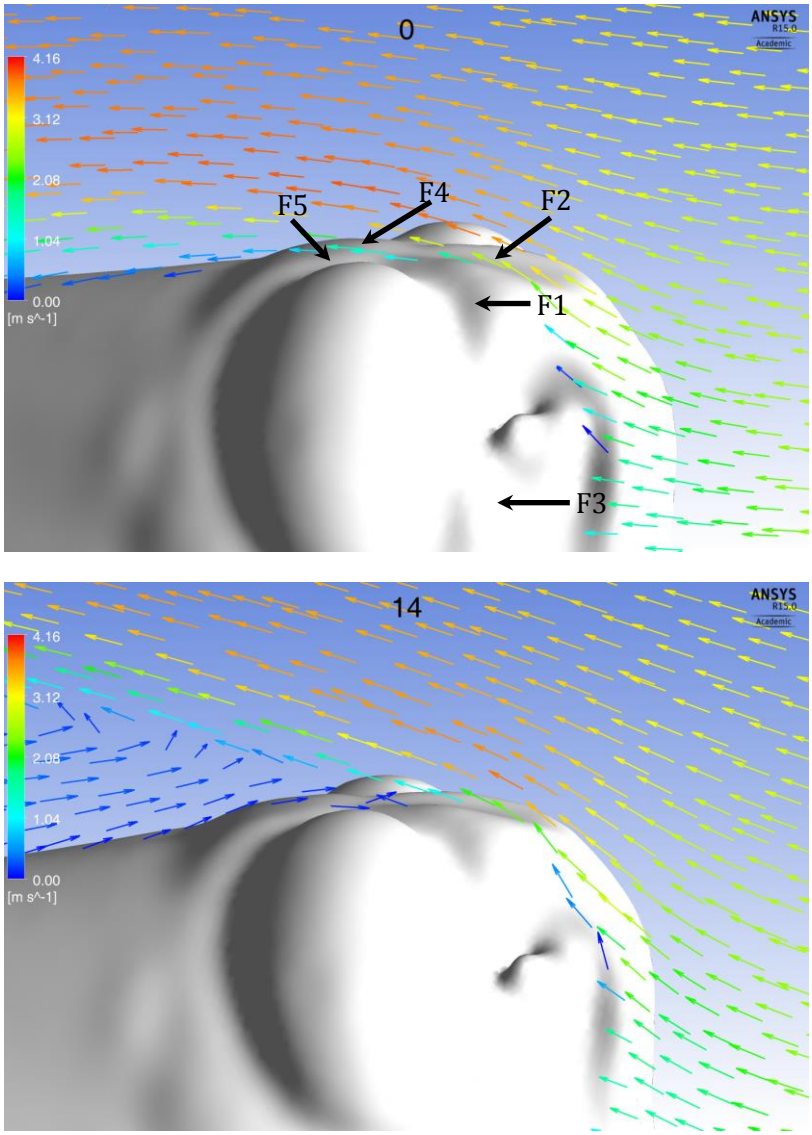


Figure 39: Sagittal plane of flow vectors at 0° (top) and 14° (bottom) angle of attack. Flow separation and recirculation are clearly visible at 14° and covers areas corresponding to F4 and F5, but does not stretch further forward to the areas containing fields F1 and F2. Colour key indicates flow speed. Vector magnitude (length) has been normalized in this figure.

Under changing sideslip, the average vectors for F1 and F2 show a pronounced directional response to changing sideslip angle as is clear from their fan-like arrangement. In contrast, F3-5 all show a tight bunching of the vectors. Thus, although the entire head has been moved through the range $-8° \leq \beta \leq 8°$, the local flows over F3-5 do not reflect these changes. In all fields, magnitudes appear to be highly consistent.

Figure 40 plots solely the magnitude (airspeed) component of the flow vectors shown in Figure 38, illustrating the patterns we have described for α and β.

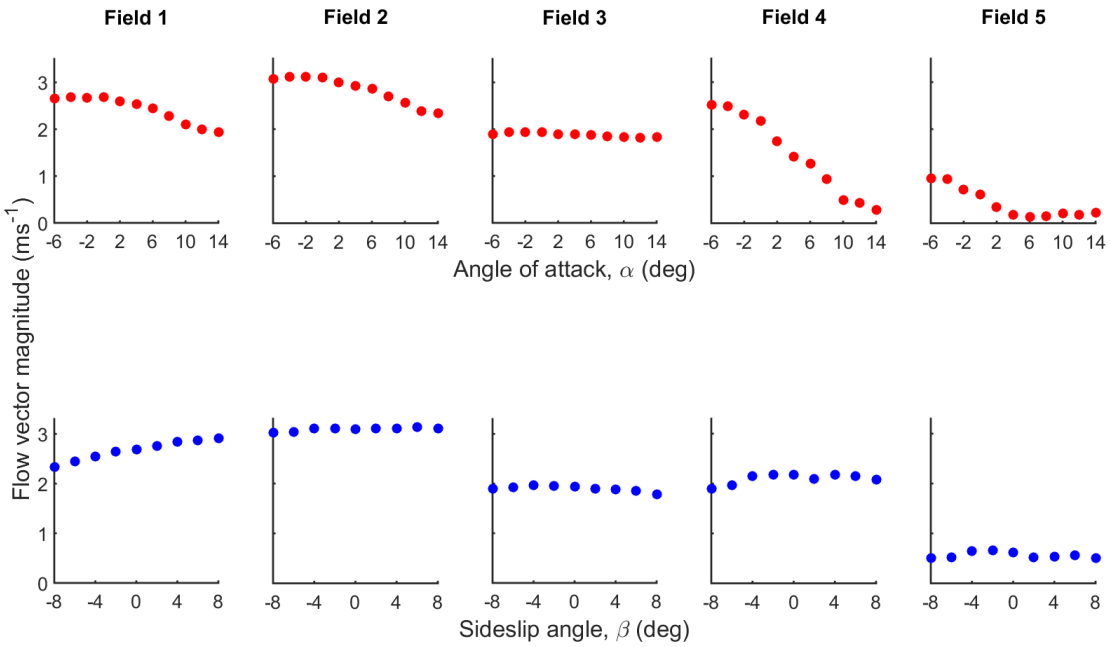


Figure 40: Magnitude (y-axis) of the average flow vectors measured over each field at each angle of attack, α (top row), and sideslip, β (bottom row) of the head (x-axis). Column number corresponds to hair field number.

To isolate and analyse solely the direction component of the flow vector, we quantified the relative changes between the angle of the head and the angles between mean flow vectors over each field, using gain plots (Figure 41).

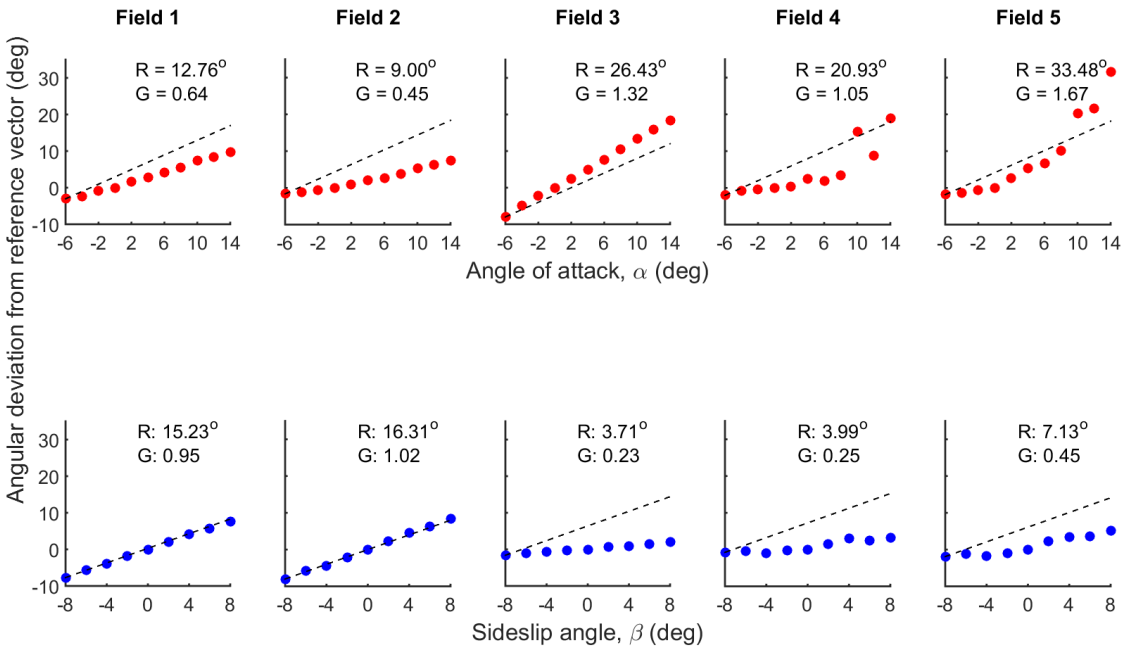


Figure 41: Gain plots. x-axis corresponds to the experimentally changed angle of the head. y-axis refers to the angular deviation from the reference flow vector, defined as the vector measured at 0° for both α and β. The first data point for the top row of graphs is therefore the angle between the vector measured at 0° and the vector measured at -6° α. Column number corresponds to hair field number. Text annotations give the range of angles (R) for each hair field under changing angle of attack and sideslip, along with their linear gains (G), the average gain over all measurement conditions) relative to the experimentally changed head angle. The dotted line corresponds to a gain of 1.

Under changing angle of attack, F3 shows a near linear response to changing head angle, with an overall gain of 1.32. The gain >1 signifies that the angle between the mean flow vectors at -6° and 14° over F3 was greater than the range of angles the head was moved through (20°). Therefore, local flow directions are amplified over F3 relative to the overall changes in head angle. F1 and F2 show similarly linear responses but with smaller gains of 0.64 and 0.45 respectively. In contrast, F4 and F5 show a different pattern of small, approximately linear increases for the first few changes in head position, followed by sporadic jumps, reflecting the unsteady flow conditions caused by flow separation.

With changing sideslip angle, F1 and F2 show a similarly linear change in average vector direction as with changing angle of attack, both with gains of approximately 1. However, F3-

5 all exhibit only very small changes in sideslip angle, with even some decreases in the angle between successive vectors.

What aerodynamic features do the fields experience?

The collective assessment of the gain and magnitude plots, and qualitative examination of the airflows (Figure 38), allowed us to form predictions as to what aerodynamic features each field seems best suited to sense. The similarities in response properties between certain pairs of fields led us to treat the five spatially distinct fields of sensilla as three groups in our predictions: {F1 and F2}, {F4 and F5} and {F3}. Interestingly, the fields form these exact three groups when classified according to their central neuronal projections to the descending neurons (DNs) [33].

F1 and F2 sense changes in sideslip and angle of attack

F1 and F2 are well-suited to act as consistent sensors of sideslip. They both exhibit gains of around 1 to changing sideslip (in local flow angle relative to overall head angle), with highly consistent vector magnitude. This results in a simple stimulus signal composed almost entirely of the direction component of the flow vector.

These fields also exhibit a similar response to varying angle of attack – approximately linear changes in vector direction, although with smaller gains relative to the sideslip case (0.64 and 0.45 for F1 and F2, respectively). The stimulus signal is also more complex as there are also changes in magnitude caused by flow beginning to separate from the top of the head at high pitch angles. Therefore, F1 and F2 could theoretically provide angle of attack sensing through changes in both flow vector direction and speed, although with lower sensitivity and a more complicated signal than sensing sideslip.

F4 and F5 sense high angles of attack

F4 and F5 could sense changes in angle of attack through the large and sudden declines in magnitude of airflow at high angles of attack caused by flow separation. This step detection

could be effective in sensing high body angle of attack, which itself could be a useful indicator to the locust in preventing aerodynamic stall.

As local flows over F4 and F5 respond little to sideslip, with minimal changes in magnitude and small angle gains, these fields may be effective as solely angle of attack sensors. In contrast, the response properties of fields F1 and F2 may make it difficult to isolate changes in just α or β. For example, during a combined pitch and yaw rotation (a common manoeuvre in flying insects), F1 and F2 would experience changes in sideslip through varying flow direction and changes in angle of attack through varying magnitude, creating a complicated stimulus.

F3 senses consistent changes in angle of attack

F3 is distinct due to its location on the vertical plane, leading to clear differences in the flows it experiences. Under changing α, vector magnitude remains highly consistent, while direction changes in a linear fashion. As we have mentioned, F3 significantly amplifies the local flow direction relative to the changes in overall head orientation. With varying β, vector magnitude remains highly consistent, as the range of angles was not sufficiently large to cause lateral flow separation, and changes in vector direction were minimal, with a range of only 4°. Therefore F3 could provide an effective sensor for angle of attack, providing a clean stimulus caused almost exclusively by changes in flow direction.

Airflow stimuli in the context of flight

We have discussed above the different aerodynamic stimuli each area of trichoid sensilla may sense, but not the context of how these stimuli may emerge during flight. If a locust is flying forward in an atmosphere of still air, the only airflow the trichoid sensilla would receive would be from the movement of the locust through the air and perhaps from the induced flow caused by the beating wings (see e.g. [137]). In this theoretical case, the hairs may play several roles: excessive angle of attack could cause flow separation from the top of the head and this could be indicated by a changing response of the sensilla. Secondly, if

the orientation of the head is different from the body, for example in sideslip, this discrepancy could be fed back by the response of the sensilla. Knowing the relative position of both head and body is likely crucial for flight control, given that the major sensory systems used in flight are located on the head, while the actuators (wings) are thoracic appendages. Additionally, keeping the head in alignment with the body may be crucial for accurate operation of certain sensors, such as the antennae, that function as a pair to detect airspeed based on oncoming flow (see review in [10]). Proprioceptive systems in the neck are known to be involved in measuring the angular position of the head relative to the body in various insect species (e.g. see review in [138]), but the hairs could also be involved in this role.

When the surrounding air is not still, significantly large gusts relative to the airspeed of the locust may also activate a response from hairs, thereby indicating external flow conditions that may need to be counteracted for stable flight. In this way, the sensilla may feed forward input to wing actuators, providing information on flow features before they even reach the wings. If locusts need to fly across the prevailing wind, the hairs could be used to monitor and maintain the sideslip flow. Additionally, locusts often fly at night, when visual cues are greatly reduced, and the hairs could be key in monitoring and counteracting wind drift. Locusts also often fly in swarms, and it has been demonstrated that a locust flying in the wake of another will couple its wing-beat to match the leader, with this information being transmitted in the wing-beat wake and detected by the head trichoid sensilla [139]. The wake is complex and turbulent (and no doubt more so in a swarm), therefore it may advantageous to have groups of sensilla that respond to different stimuli (as we have hypothesised here) to capture this information accurately.

3.4 Conclusion

Our CFD data provided detailed simulations of the expected airflow over the fields of trichoid sensilla under equilibrium flight conditions, and at a range of small rotational disturbances about this point, building on the experimental data from Chapter 2. The

simulations revealed that the flow around the head acts to amplify locally the effect of changes to the inflow conditions. Specifically, the angular amplification of the local flow makes F3 well suited physically to sensing angle of attack, and F1 and F2 particularly suited to sensing sideslip angle. In addition, the magnitude amplification of the local flow over fields F4 and F5 caused by flow separation on the back of the head makes these fields ideally located for detecting when the body angle exceeds a certain threshold.

Our discussion and hypotheses on the roles of the fields have so far solely been in reference to the characteristic airflows measured over each area. In Chapter 4, we consider the physiological and response properties of the hairs themselves, and the implications these have for our proposed functions.

Chapter 4

Head trichoid sensilla imaging

4.1 Introduction

Insect sensory systems are typically anisotropic – they are tuned to particular directions of motion. This has been elegantly demonstrated for the tangential cells of the compound eyes [140], the campaniform sensilla [62], and the flow-sensing trichoid sensilla of locusts [21]. In the case of the trichoid sensilla, the directional bias of each hair is readily revealed phenotypically by its direction of curvature, thus offering a simple method of characterising the neural response of each hair without the need for further neurophysiological testing. Therefore, simply by visualising the head sensilla of the desert locust, we can consider whether they are optimally oriented for sensing the aerodynamic features we have suggested in Chapter 3. Specifically, that flows over F1 and F2 vary in relation to sideslip and angle of attack, F4 and F5 to step changes in angle of attack, and F3 to changes in angle of attack.

Building upon our prior experience with XMT imaging (Chapter 2), we return to, and optimise, this method as it offers a good balance of simplicity, acquisition speed, and resolution to acquire 3D geometries. Although our previous scans were not of sufficiently high resolution to resolve all the trichoid sensilla cleanly, we identified several parameters that could be improved to allow higher resolution and clarity imaging: (i) the sample was larger than necessary to scan just the hair areas (reducing overall resolution), (ii) the sample was not stained to maximise contrast, and (iii) we used largely default scanning settings; applying only some minimal ring artefact reduction and beam hardening correction. In this chapter we detail the XMT refinements and techniques used to scan several locust heads of three different species, followed by presentation of the scan data. We then quantify the inferred peak directional sensitivity for every trichoid sensillum on each locust's head and discuss these data in the context of our proposed roles for each hair field. Earlier light microscope work by Camhi [21] and Smola [23] provided qualitative characterisation of the sensilla, although in the former case, of only a small number of the longest hairs. In contrast to these studies, our XMT scans provide a quantitative dataset for visualising the hairs and determining their response properties using a method that can be rapidly repeated across multiple individuals. Having a numerical quantity is key in understanding and formally testing the relationship between the hair sensors and the flow stimuli they receive, which we explore in Chapter 5.

How do we expect hairs to be oriented?

At the end of Chapter 3, we described the flow changes that each field experiences under varying orientations of the head. However, whether the hairs themselves are able to sense these changes is the crucial question in understanding the role of the trichoid sensilla. Camhi's [21] work demonstrated that the trichoid sensilla respond to airflow by the hair shaft deflecting at the base, with the deflection encoded by the number of spikes in the cuticular neuron below. The spike rate is a function of airspeed, but also of direction, with the highest number of spikes created when the hair is stimulated by airflow directly

opposite the direction of the hair shaft curvature, and decreasing spike rates with airflow either side of this point (Figure 42). It is important to note that Camhi recorded the 'plateau spike frequency' of the hairs, that is, the spike frequency recorded after the initial 0.25 s of stimulation by airflow. As an example, Camhi demonstrated that a hair stimulated at 4.5 ms^{-1} initially produced a frequency of 200 spike per seconds, but this rapidly fell to 125 spikes per second within 0.25 s. Therefore, the tuning curves in Figure 42 represent the adapted responses under static flow conditions. What implications do these response properties have on our proposed roles for each field, and how would we expect hairs to be oriented for sensing these features of airflow?

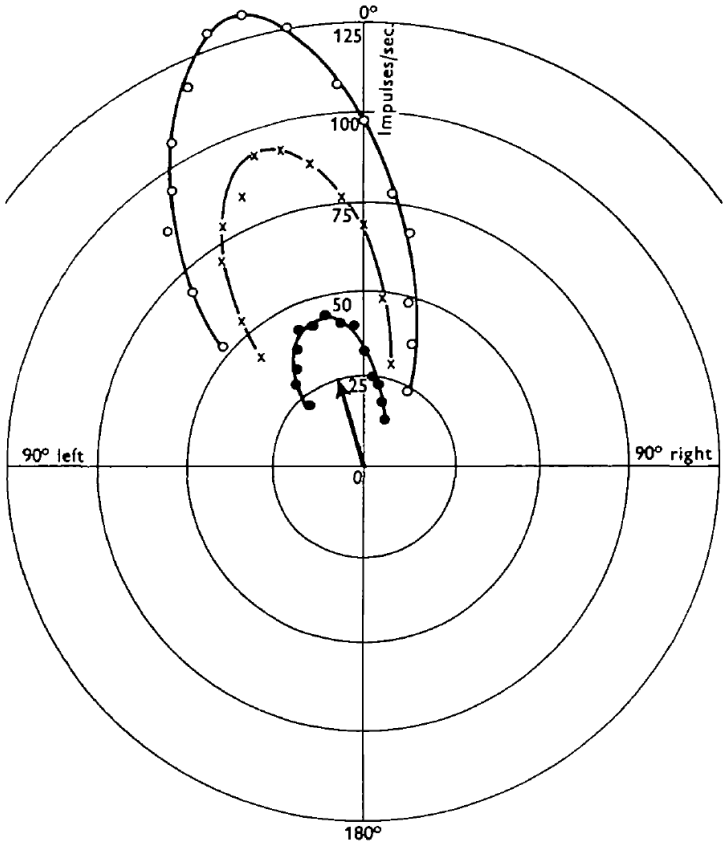


Figure 42: Tuning curve showing number of impulses in a hair neuron relative to angle of airflow. The arrow represents the direction of this particular hair's curve. Filled dots, crosses, and open dots represent three different flow speeds of 1.5, 3, and 4.5 ms^{-1} respectively. Spike rate depends on direction and airspeed. From Camhi [21].

F1 and F2

The hairs' placement on the horizontal, dorsal surface of the head suggests they are well placed to act as a sideslip sensors. If they were oriented to curve into oncoming flow at a sideslip angle of 0°, the neurons would fire maximally at this angle, with deviations either side of this point causing a decrease in spike rate. This orientation would allow hairs to capture changing sideslip in either direction, but this would be energetically costly as neurons would be firing for a great deal of flight. Additionally, the constant stimulation may lead to further adaptation of the response (Camhi recorded a further 10% decline in the plateau spike frequency over the course of five minutes). The alternative scenario would be for the hairs to be curved at some offset relative to the equilibrium flight condition of 0°. For example, at 45° (the approximate maximum angle causing spiking according to Camhi's tuning curve (Figure 42)), the hair neuron would have very little/zero spiking at 0°, but the spike rate would gradually increase as sideslip angle increased (with maximum spiking at 45°). This offset would allow discrimination of flow direction, as the hairs would only respond to changing sideslip from rotations in one direction. In order to detect changing sideslip from either direction, another set of hairs could be placed with curvature in the opposite direction (i.e. reflected in the sagittal plane of the locust). This could be the case as hair fields are present in pairs – one on each side of the head. Such an arrangement would be favourable both energetically and in terms of discriminating the flow changes, as only one of these two fields would be spiking at any one time for a particular non-zero sideslip angle.

In Chapter 3, we demonstrated that the local flow over F1 and F2 also exhibited clear variations in flow direction and magnitude under changing angle of attack. However, the hairs are not suited to monitoring the changing flow directions. This is because the dorsal location of the hairs (which protrude vertically from the surface) means the flow direction in the response plane of the hair is constant, irrespective of the angle of attack (i.e. the only directional airflow change that will change the response of the hair is in sideslip). Nevertheless, Camhi's tuning curve shows that the hair neuron spike rate is also a function

of airspeed. Therefore changes in flow magnitude caused by changing angle of attack could be sensed by the hairs in F1 and F2. We believe the step change response of F4 and F5, and consistent response of F3 (discussed below) are better suited for monitoring changes of angle of attack. However, F1 and F2 could provide a constant measure of airspeed at consistent orientations. For example, we might expect the hairs to be oriented directly parallel and curving into oncoming flow around the equilibrium 0° case, as this would allow consistent airspeed measurement.

F4 and F5

Fields F4 and F5 could provide step detection of flow separation on the head, by sensing changes in speed. As the spike rate of hairs is a function of airspeed, increasing angle of attack would translate to gradually decreasing spike rate, until there was very a low/zero spiking. In order to fulfil this role, it would make most sense for hairs in F4 and F5 to be oriented curving directly into oncoming flow at a sideslip angle of 0°. This would result in low angles of attack causing significant stimulation of the hairs, with the response declining as the angle increases. The downside to this arrangement would be that hairs are likely stimulated relatively constantly at low α, potentially causing neuronal adaptation. Nevertheless, the switch from high neuron spike rate to low/zero spiking could still be used to indicate critical angle values.

F3

Flow patterns over F3 demonstrated that hairs are very well placed to sense changes in angle of attack by detecting the flow direction, which is locally amplified by the geometry of the head. For this role, we might expect that hairs will be oriented such that their curvature is offset, for example by 45°, relative to oncoming flow for the energetic advantages mentioned above. As already described, because the hairs are only able to respond in one 180° plane (flow must be opposite the direction of curvature to cause spiking), if they are oriented at an offset to the equilibrium flow condition at 0°, they could only respond to changing angle of attack in one direction (either pitching up or pitching down). If the aim

was to measure changing angle of attack relatively constantly, the hairs could be oriented curving directly into oncoming flow at the equilibrium 0°. In this scenario, as angle of attack changes in either direction, spike rate will gradually decrease (as we predicted for F1 and F2 under sideslip changes). However, this constant excitement again exposes the neurons to energetic costs and adaptation, and may not allow for easy discrimination between pitch up or pitch down manoeuvres.

4.2 Methods

In order to image the hairs, and thus test our predictions, we scanned locust heads using two X-ray micro computed tomography (XMT) techniques:

Benchtop XMT

When using XMT, it is preferable to optimise contrast between structures of different density in order to distinguish each material easily. With such fine structures as the trichoid sensilla, it is particularly important to maximise contrast with the surrounding air and we therefore developed a simple staining technique using elemental iodine, detailed elsewhere [141].

We chose to scan two other species of locust to allow comparative study of the trichoid sensilla. Adults of *Schistocerca gregaria, Locusta migratoria* (Blades Biological, Edenbridge, UK), and *Nomadacris septumfasciata* (wild caught by BugzUK, Norwich, UK) species were first killed by freezing at -20°C. They were then thawed overnight and placed individually or in pairs on the bottom of a 250 mL widemouth glass-stoppered reagent bottle (Schott AG, Mainz, Germany) or a glass-lidded weighing bottle (Lenz Laborglas GmbH & Co. KG, Wertheim, Germany) with 5–10 pellets of elemental iodine, each pellet having a mass of around 25 mg. To prevent gas leaks, we sealed the ground glass joint with a thin layer of PTFE grease (HGT100, Solent Lubricants, Leicester, UK). After incubating at room temperature for 20 h, 7 d, 14 d, or 30 d, locusts were carefully decapitated by dissecting around the neck membrane and through the soft tissues of the neck [142] with fine scissors.

We mounted the head for XMT by melting dental wax around the mouthpieces and the exposed section of the neck, then attaching the wax to a cut-down cryo-tube fitted to the rotation stage stub. Using a Skyscan 1172F (Bruker MicroCT, Kontich, Belgium) with its tungsten target X-ray source set to 59 kV and 167 lA, and 0.25 mm Al filter, we positioned the locust head in the beam so as to achieve 1.9–2.5 μm nominal pixel spacing while maintaining the full diameter of the head within the 4000 x 2672 detector element of the camera. The head was rotated through 180° or 360° at 0.10° – 0.15° increments with 1–4x averaging and 3.5–14 s total exposure per projection. Tomographic reconstructions were produced with NRecon (SkyScan, v1.6.9) on the GPU (NVIDIA GTX 680, EVGA) using the Feldkamp cone beam reconstruction algorithm [120] and visualised in Amira (ver. 5.6, FEI, USA). Iodine vapor staining imparted strong positive contrast to insect cuticle and muscle, moderate positive contrast to neural tissue of the eye, nerves, ganglia, and brain, and allowed segmentation and identification of fine tissue structures. No practical difference in staining efficacy was noted after 7 d; however, an overnight exposure of 20h was insufficient to generate adequate contrast for XMT [141].

Visual comparison of pilot scans using the variety of parameters listed above led to a final protocol of 360° scans with 0.10° degree rotation increments, 4x averaging, 0.25 mm Al filter, 3.5 s exposure per projection, and approximately 2 μm nominal pixel spacing, requiring scan times of over 17 hours. Over such long periods, it was extremely difficult to avoid minute movements of the specimen, caused by tissue shrinkage due to dehydration or the sample shifting in its mount, and these created movement artefacts in several scans. The artefacts manifested themselves as either doubling of objects, or long streaks of noise. Streaks are a particular problem at high contrast edges, and therefore are most likely to occur at the head surface, where the hairs are present [143]. The chance of movement is highly reduced by decreasing scan time, however, pilot scans on a considerably faster (due to higher power) Metris X-Tek HMX ST 225 scanner yielded similar streaking patterns despite efforts to reduce any chance of movement. The final protocol using the SkyScan

machine and 17 hour scans produced the cleanest results, perhaps due to the effect of 4 times averaging.

Synchrotron XMT

Subsequent to acquiring benchtop XMT scans, we were able to acquire scans at the Swiss Light Source (SLS) synchrotron. The TOMCAT beamline at the SLS offers orders of magnitude higher brilliance and coherence X-rays, and reductions in acquisition time relative to benchtop XMT sources. The methodology was substantially similar to previous SLS tomographic scans produced in our research group, as detailed in [144].

The X-ray source was a superbending magnet located 25 m from the sample and used in a monochromatic beam configuration. A double crystal multilayer monochromator placed 7 m downstream of the source extracted X-rays with a bandwidth of 2% at 16 keV photon energy and ring current of 401.29 mA. The beam was 5.43 mm wide and 4.68 mm high at the sample site. A 150 μm thick, LuAG:Ce scintillator was placed at a distance of 350 mm behind the sample to convert the transmitted X-rays into visible light. The resulting edge-enhanced image was magnified 2x using a custom-made, high numerical-aperture microscope (Elya solutions, s.r.o). Projection images were acquired with a pco.dimax 12-bit CMOS detector system recording at 2,500 Hz. The locust heads were rotated through 180° in 0.12° increments with 0.08 s total exposure per projection.

The projections were subsequently despeckled to remove bright pixels produced by scattered X-rays hitting the detector, and were flat field corrected. Phase retrieval utilised a single-image non-iterative algorithm developed by Paganin et al. [145] and implemented in the software ANKAPhase [146]. Tomographic reconstruction was performed using a Fourier transform-based algorithm [147], with the resulting voxels having an isotropic spacing of 3.24 μm.

4.3 Results and discussion

Of the 15 individuals scanned using both methods, the four best *Schistocerca gregaria* scans from the desktop XMT, one synchrotron *S. gregaria*, and one *Locusta migratoria* were chosen for analysis based on clarity of the data. Each scan revealed several hundred trichoid sensilla. Figure 43 illustrates the resultant 3D imagery for a single locust from the synchrotron scan, demonstrating the clear visibility of the hairs. Figure 44 provides an overview of the complete scans from the synchrotron and benchtop scanners. Note, the increased noise in the benchtop data.

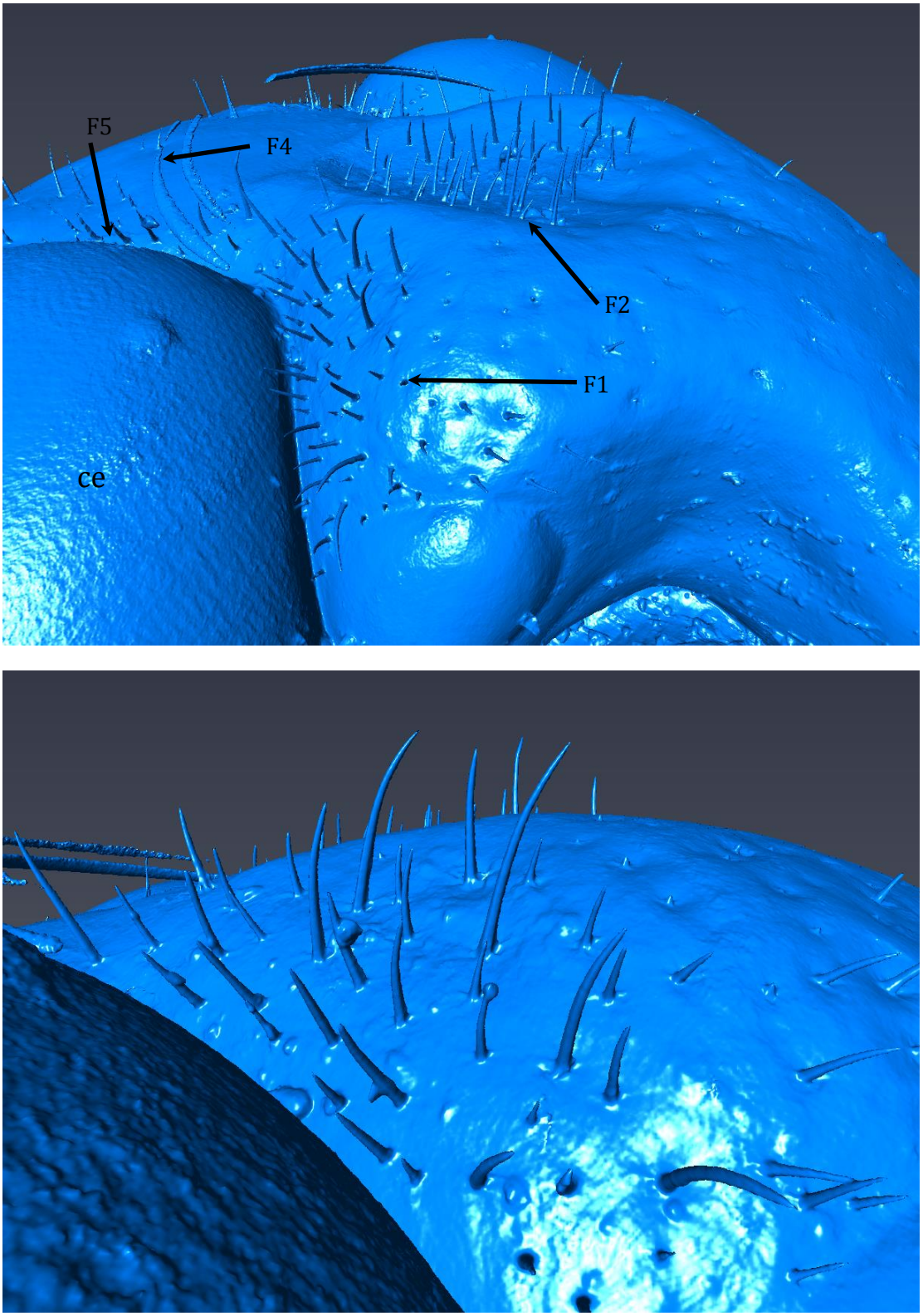


Figure 43: Dorsolateral view XMT visualisations of a S. gregaria from synchrotron data, generated using Amira. ce = compound eye. Top: the dorsal surface of the head. Hairs in F1, F2, F4, and F5 are visible. Bottom: Close-up of hairs in F1 on the right side of the head, demonstrating the hairs' pronounced curvature.

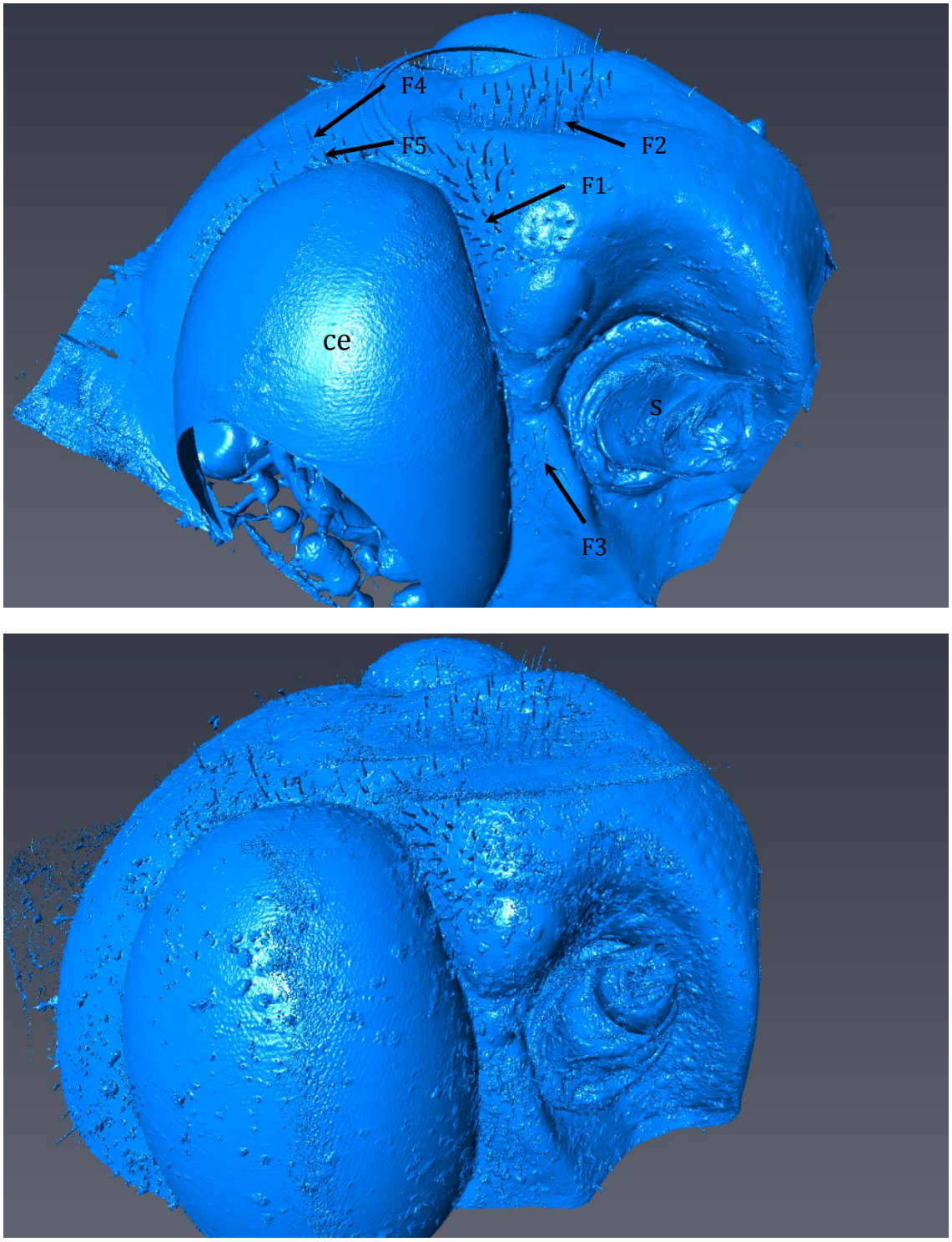


Figure 44: Lateral view XMT visualisations of a S. gregaria from synchrotron (top) and benchtop (bottom) scanner data, generated using Amira. ce = compound eye, s = scape (a segment of the antenna). Note the greatly increased noise in the benchtop case. A small amount of ring artefact noise can be seen dorsally on the synchrotron scan. In both cases, only the top half of the head was scanned due to constraints on the field of view relative to pixel resolution.

Many hairs show very pronounced curves and neighbouring hairs tend to curve in a comparable direction, while the degree of curvature appears to vary considerably. The majority of hairs also exhibit a lean (relative to the head surface), seemingly corresponding to the direction of the curvature. Although no distinction is made between curve and lean in previous literature, as lean appears to correlate to the direction of curvature we predicted it was likely to also be a good indicator of the peak directional sensitivity of the hairs.

The hairs are not densely packed – neighbouring sensilla are generally at least several diameters (in reference to the base of the sensilla) apart. The densest areas of hairs are found in F1, F2, and F5, with very few hairs particularly over F4. F3 shows a high density of hairs proximal to the antennal base, but with vary sparse hairs ventrally. These patterns were consistent across all the different individuals visualised. As the hairs function by deflecting in response to wind, the spatial separation may serve to reduce mechanical coupling.

F2 and F3 are the most discretely grouped. F2 is clearly separated from neighbouring F1 by a prominent ridge in the head cuticle, while F3 is the only field on the vertical plane. In the case of F1 and F5, and F5 and F4, the phenotypic separation of the hairs is less distinct, but we have maintained the historic nomenclature for ease of discussion.

Calculating peak directional sensitivity

We calculated the direction of curvature and the lean for all hairs. For both methods, the first step was to define the entire length of every hair in 3D space using a skeletonisation function [148]. For each hair, this required choosing three points (by clicking on the isosurface visualisation in Amira), corresponding approximately to the tip, middle, and base. These points provided a guidance area for the function to find the centreline (the skeleton, outputted as a set of 3D Cartesian points) using a fast-marching distance transform [148]. Figure 45 illustrates an example of this operation on a single hair. Every hair was manually checked and the skeleton clipped to ensure only the hair itself was

captured by the function – occasionally the skeleton continued into other structures in the cuticle when reaching the base of the hair.

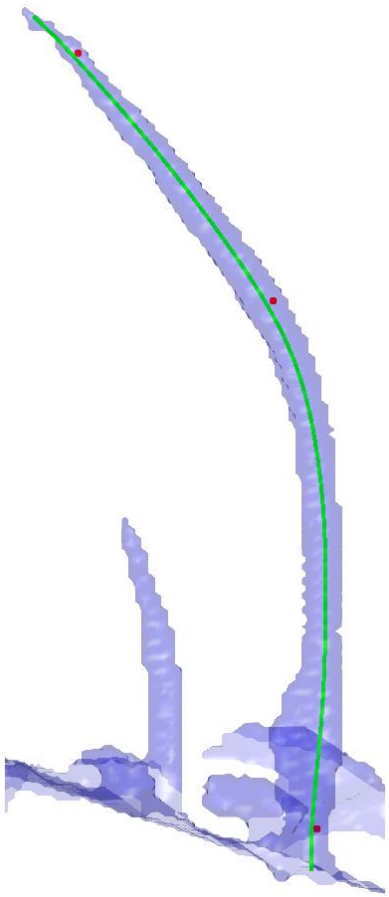


Figure 45: A single hair is shown as a semi-transparent isosurface (purple), along with the three points defining tip, middle, and base (red dots), and resulting centre-line (green trace) from the skeleton function.

Figure 46 displays skeletons for all hairs of one individual, with a separately rendered surface of the top of the head.

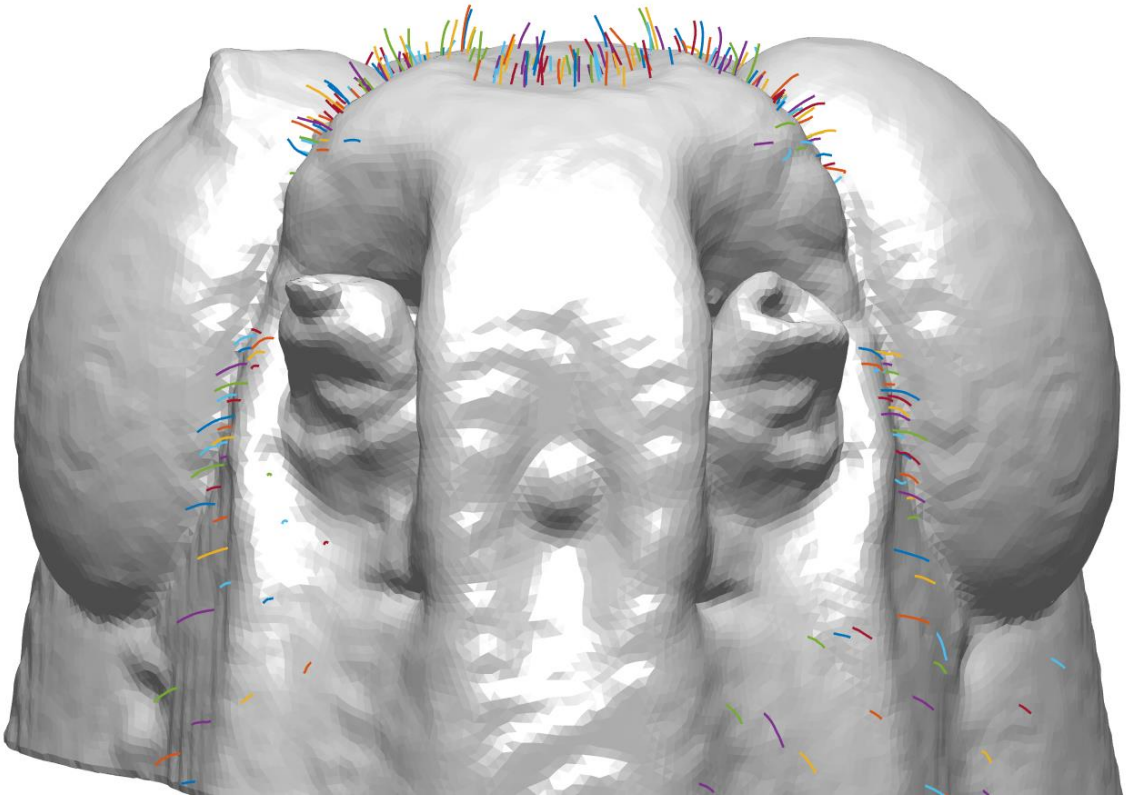


Figure 46: Anterior view of the centrelines (skeletons) computed for the hairs on the head surface of an individual S. gregaria. For clarity, the hairs are coloured arbitrarily.

Using the skeleton data, we developed separate methods to calculate the directions of curvature and lean for every hair:

Finding the direction of hair curvature

1. For each hair, we fitted the 2D plane that minimised the sum of squares of the orthogonal distance from the plane to all the points of the skeleton. This represented the plane of curvature for the hair, but did not provide a specific direction within that plane.
2. We defined another plane that was normal to the straight line between the base and tip of the hair.
3. We found the line of intersection between these two planes. The vector of peak sensitivity will lie on this line, but we need to define its sign and magnitude.

4. To find the magnitude and direction, we use the camber of the curve relative to the line between the base and tip. To find this, we project all the hair skeleton points onto the line of intersection (from step 3). The projected point lying furthest from the base point along this line represents the widest part of the curve, and therefore the camber. The distance between this point and the base of the hair defined the magnitude of the peak sensitivity vector, and the sign of this difference defines the direction (along the line in step 3, along which the vector lies).

This resultant vector (hereafter referred to as the hair sensitivity vector, HSV) defines the direction of the hair's curvature. The vector is equivalent to the shadow that would be cast by a distant light source on the line joining the hair tip and base onto the plane normal to this line. The vector magnitude provides an indication of the extent of curvature, although it also encapsulates the camber of the hair and therefore cannot be used to exclusively measure curvature. It is not known whether the extent of curvature bears any relation to the strength of the response, although intuitively hairs of any given length that are more curved will have less surface area exposed when the flow is directly opposite the direction of the curve, thus less drag force would be expected to act upon them. However, the surface area exposed will also change as the hair deflects in its socket under wind stimulation. Longer hairs would also be subject to greater drag forces than shorter ones.

Finding the direction of hair lean

1. We found the local head surface tangent plane for each of the 10 hair fields (F1-5 on the left and right) by minimising the sum of squares of the orthogonal distance between the plane and all the hair base points (from the skeletons) belonging to each particular field.
2. We averaged the planes for each side so as to not introduce unnecessary variation. E.g. For F1 on the left and the right, we average the plane normals, accounting for the need to first mirror one of the normals in the sagittal plane of the locust. The

average normal was then reflected back to define the new averaged plane for the other side of the head.

3. The tip and base points for each hair were then projected onto the plane relevant to the field it belongs to.
4. The direction of lean is the line between these two points, signed by the difference between them, and the distance between the points defines the extent of lean.

This vector is equivalent to the shadow that would be cast onto the tangent plane to the head (defined separately for each field) by a distant light source directly overhead.

We therefore had the option to analyse two different measures of the HSV – curvature and lean. The visualisations below use curvature as this is well-established in previous literature [21, 23], but in the next chapter, we test for differences between both measures.

HSV plots

Each of the green arrows in Figure 47 illustrates the direction of airflow that the hair in that location is most sensitive to, based on its curvature, while Figure 48 plots solely the mean HSV for each field. We show dorsal and lateral views of the HSVs for a single *S. gregaria* (Figure 47 and Figure 48), dorsal views for four other *S. gregaria* (Figure 49), and dorsal and lateral views for a single *L. migratoria* (Figure 50).

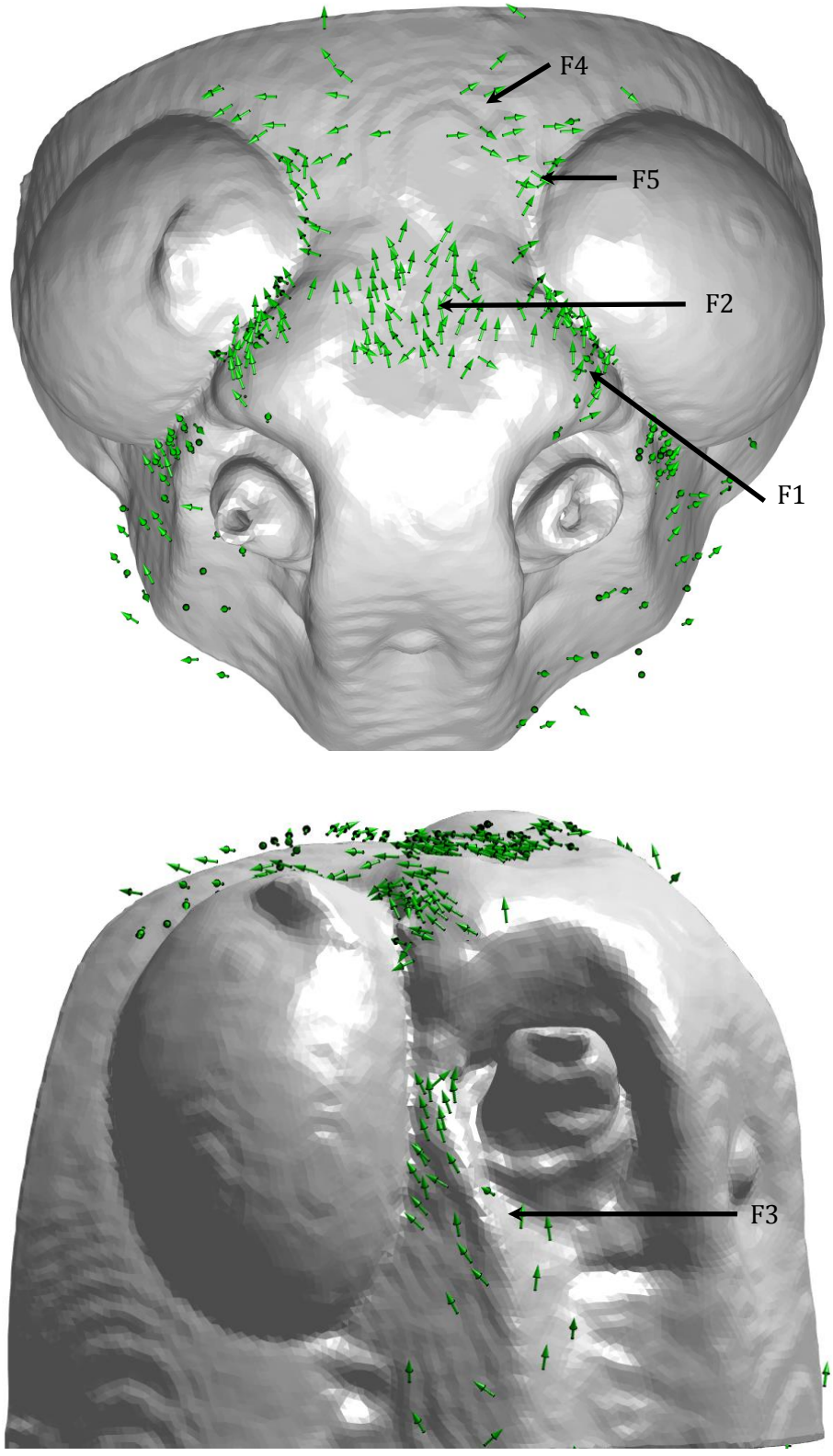


Figure 47: Dorsal (top) and lateral (bottom) views of a XMT scanned S. gregaria head. Large bulges are compound eyes. Each green arrow marks the position of a hair, and the direction of airflow to which it is most sensitive, based on the direction of the hair's curve.

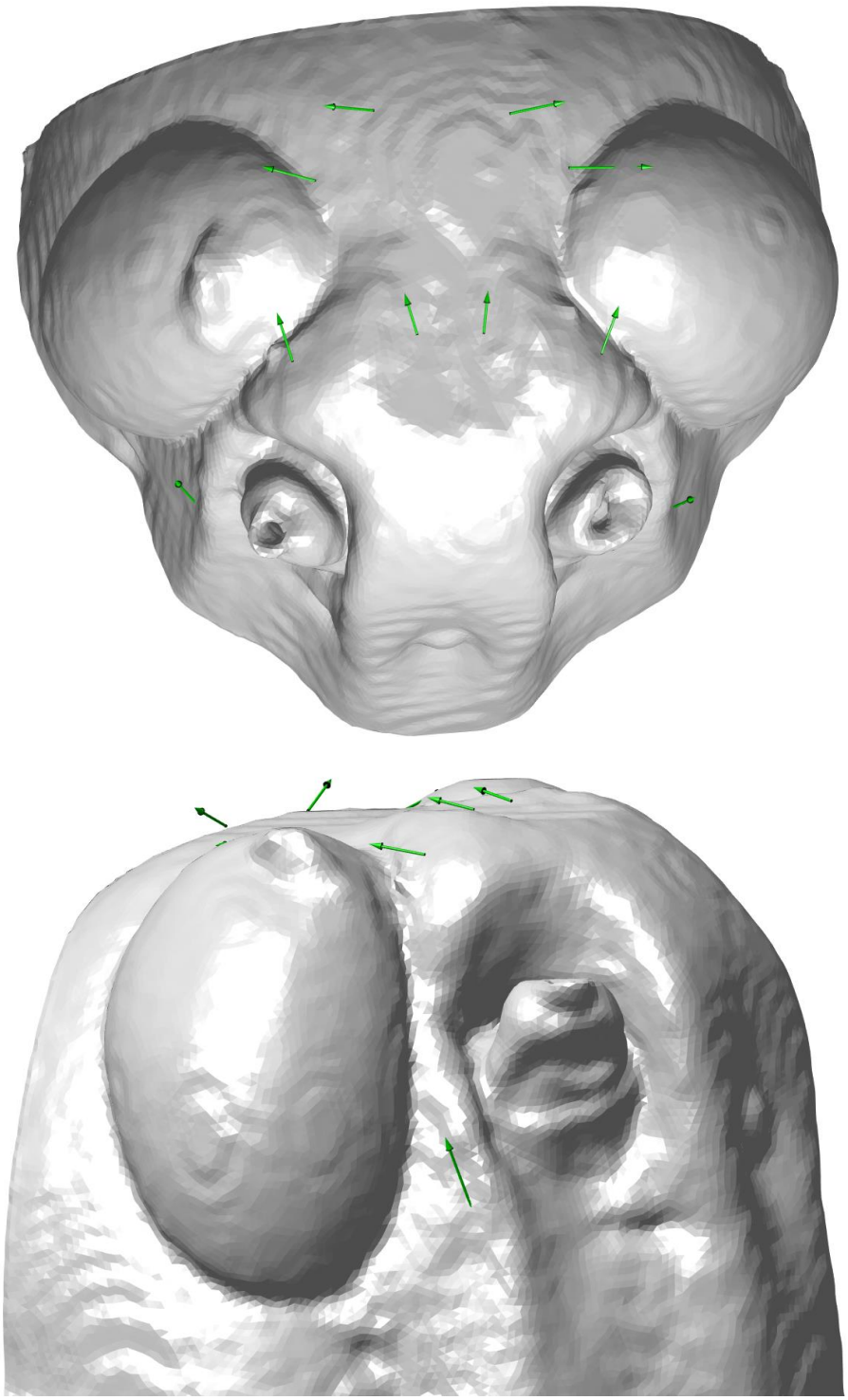


Figure 48: Dorsal (top) and lateral (bottom) views of a XMT scanned S. gregaria head, displaying the mean HSV for each field. Vector length has been uniformly increased for clarity.

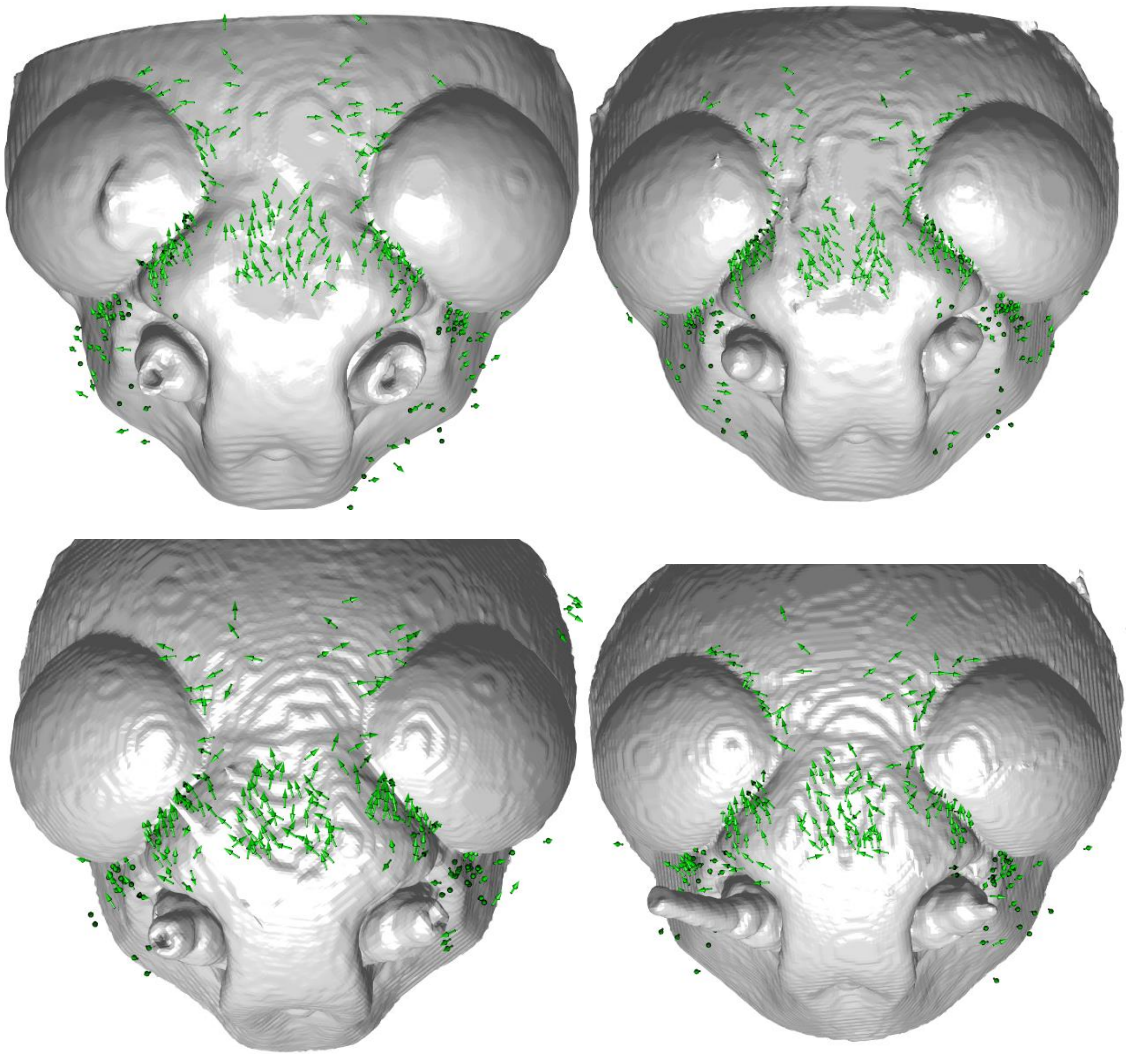


Figure 49: Dorsal views of four XMT scanned S. gregaria heads. Each green arrow marks the position of a hair, and the direction of airflow to which it is most sensitive, based on the direction of the hair's curve. Note the overall consistency of HSVs between individuals.

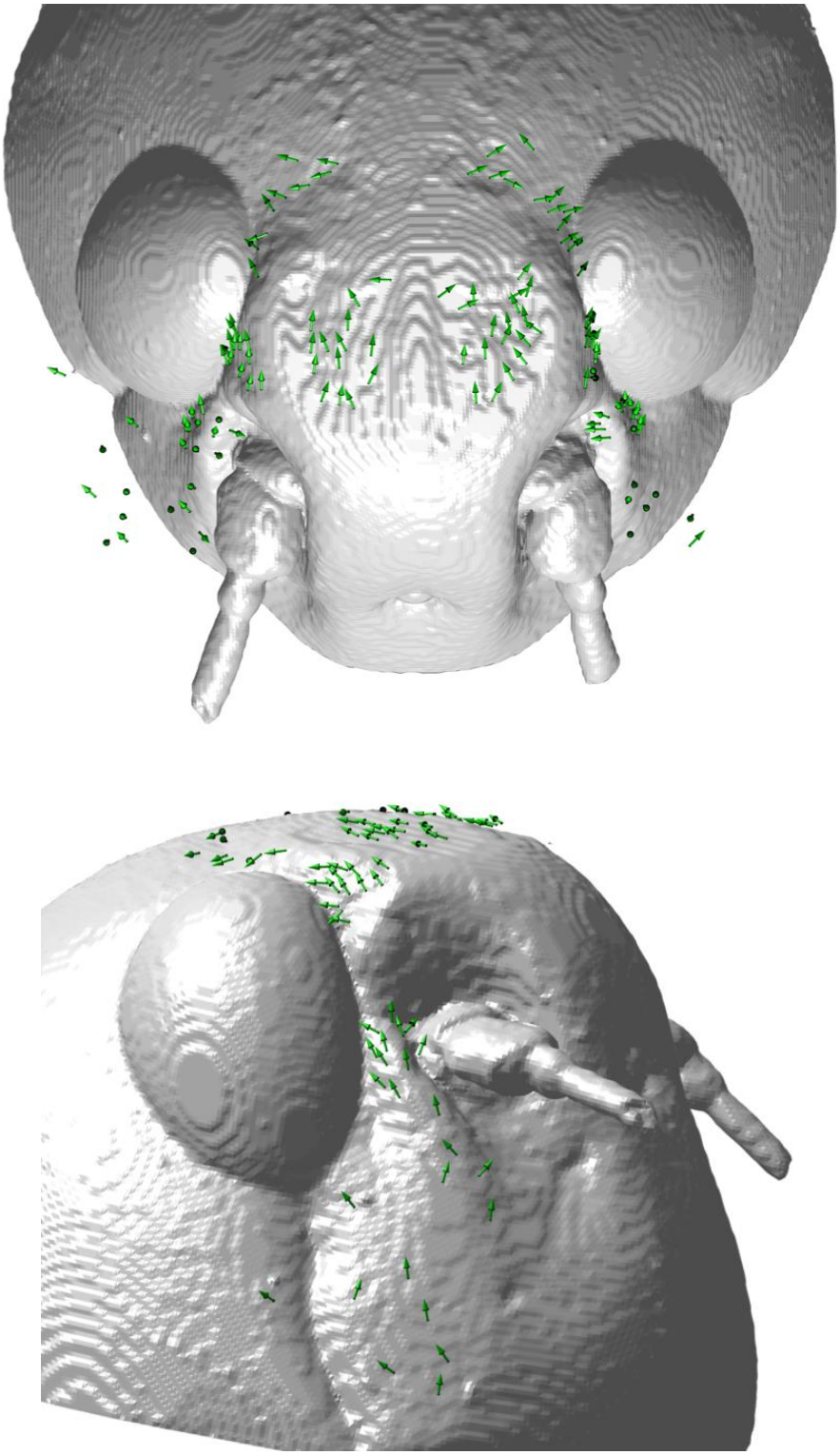


Figure 50: Same dorsal (top) and lateral (bottom) views as Figure 47, but this time of a L. migratoria head. Each green arrow marks the position of a hair, and the direction of airflow to which it is most sensitive, based on the direction of the hair's curve.

Figure 47 illustrates the consistency of HSV direction within each field. Whilst there are occasional outlying HSVs, neighbouring hairs tend to point in a similar direction. F1 and F2 HSVs largely point posteriorly with a smaller lateral component, F4 and F5 HSVs tend to point laterally, and F3 HSVs point approximately dorsally (Figure 48). The HSVs of pairs of fields on each side of the head (e.g. F1 on the right and left sides) are clearly reflected in the sagittal plane of the locust. The orientation of trichoid sensilla in F1 and F2 appears to be in agreement with our hypothesis that they could be used for sensing sideslip: the mean HSVs suggest the hairs are oriented at a slight offset relative to the airflow at the equilibrium flight condition. F3 hairs seem to point orthogonally to the airflow we expect at the equilibrium flight condition. This would be in accordance with our hypothesis that the orientation is offset relative to the flow at 0° and that they are therefore tuned to sense changes in angle of attack in one direction relative to the equilibrium condition (pitching up in this case). However, the offset is much larger than predicted, suggesting they are oriented at an angle relative to oncoming airflow that is beyond the maximum spiking angle demonstrated in Camhi's tuning curve. HSVs in F4 and F5 also point roughly orthogonally to the expected flows over these areas. This does not conform to our suggestion that hairs should curve directly into oncoming airflow to provide consistent detection of flow separation.

Figure 49 illustrates that there appears to be minimal intraspecific variation in hair curvature. We find a similar pattern when looking across species (Figure 50); although there are considerably fewer hairs present on the *L. migratoria* head (see Table 1 below), the overall direction of hairs within each field appears closely aligned with *S. gregaria*. XMT scans were also taken of wild-caught *Nomadacris septumfasciata*, however, the scans proved too noisy to extract hair measurements. Nevertheless, qualitative light microscope observations revealed a similar arrangement of HSVs. These consistencies suggest that the response properties of the hairs have been well conserved, implying they are of some importance to the locust.

The next step in our analysis is to explore these data under a quantitative framework by combining our HSV data with the CFD flows presented in Chapter 3. This allows us to

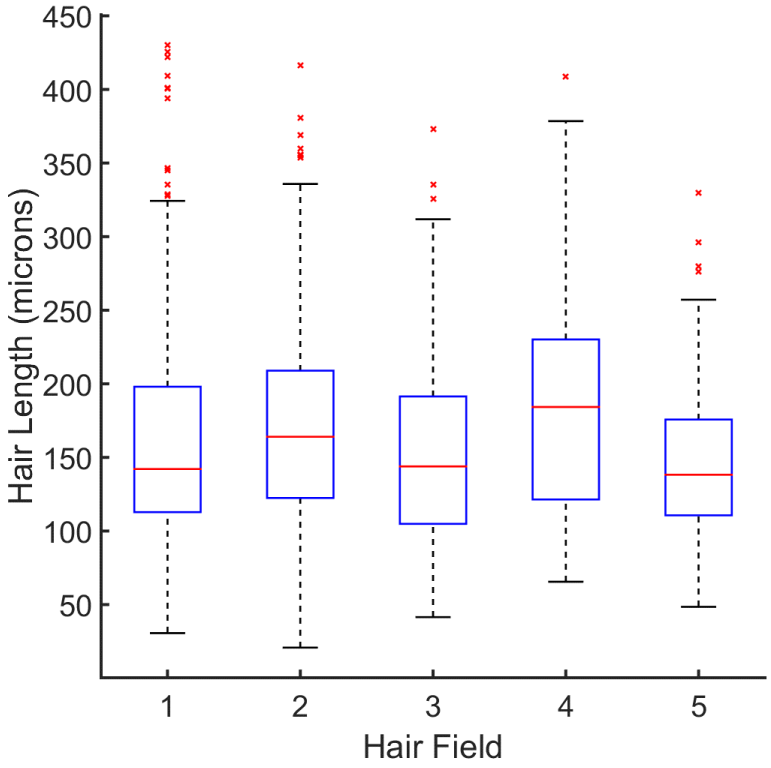
statistically test the relationship between sensor and stimulus, as well as any differences between fields, individuals, and curve and lean HSVs. We present this analysis in Chapter 5. The remainder of this chapter explores other quantities of interest extracted from our detailed characterisation of the trichoid sensilla.

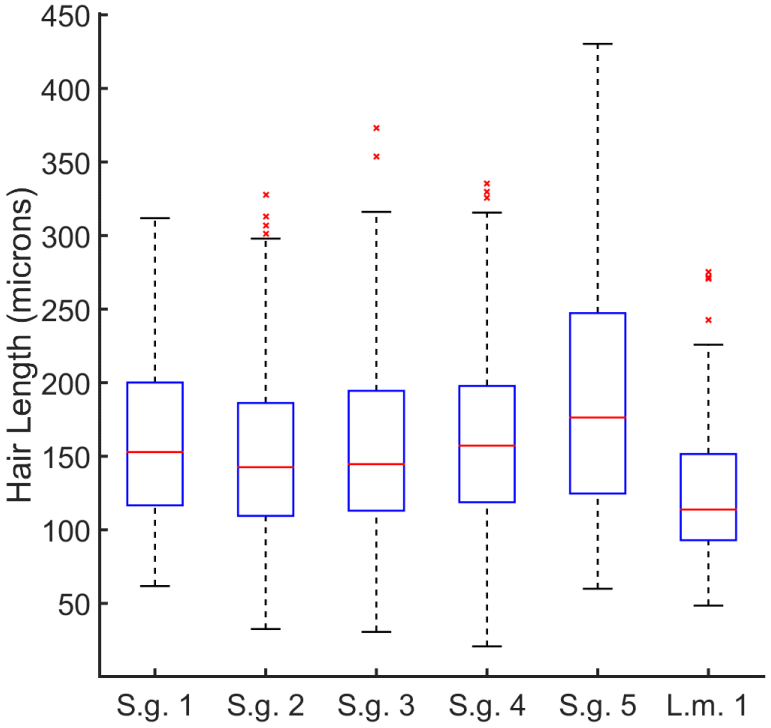
Hair metrics

In addition to curve and lean calculations, the skeleton data allowed enumeration and length calculation of all hairs. Table 1 displays this data, organised by field number.

Specimen	Number of hairs (by field number)						Length of hairs (μm)		
	F1	F2	F3	F4	F5	Total	Min	Max	Mean±SD
***S. gregaria* 1**	78	53	85	16	32	264	62	312	163±59
***S. gregaria* 2**	85	52	89	9	22	257	33	328	152±58
***S. gregaria* 3**	91	61	70	7	26	255	31	373	159±61
***S. gregaria* 4**	76	53	78	9	27	243	21	335	165±60
***S. gregaria* 5**	86	51	44	13	34	228	60	430	195±87
L. migratoria	25	33	44	9	14	125	48	275	126±47
Mean±SD	74±24	51±9	68±20	11±3	26±7	229±52			

Table 1: Number and length of all hairs across all individuals analysed.


Hair Length (microns)
450
400
350
300
250
200
150
100
50
1
2
3
4
5
Hair Field


Hair Length (microns)
450
400
350
300
250
200
150
100
50
S.g. 1
S.g. 2
S.g. 3
S.g. 4
S.g. 5
L.m. 1

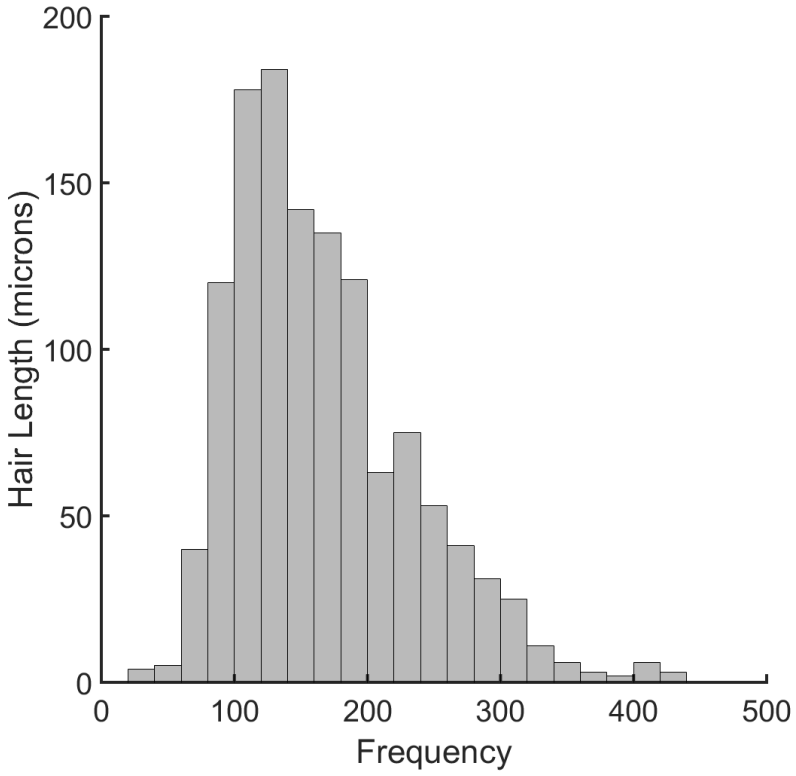


Figure 51: Top: Boxplot of hair length classified by field number. Middle: Boxplot of hair length compared across specimens. S.g. = Schistocerca gregaria. L.m. = Locusta migratoria. Red points denote outliers on both boxplots. Bottom: Histogram of hair lengths across all specimens and fields.

Figure 51 displays hair lengths across field, individual, and frequency. These data exhibit the consistency in total numbers and mean lengths of hairs across different *S. gregaria* individuals, although there is clear variation around the mean lengths. In contrast, the *L. migratoria* specimen had approximately half the total number of hairs and distinctly shorter lengths. Despite covering a large area of the head, there were very sparse numbers of hairs in F4, while F1 and F3 had the highest numbers. Hair length shows little sign of systematically varying between fields. The range of hair lengths spanned from 21 to 430 μm, with the highest frequency of hair lengths between 120 and 140 μm. Smola's 1970 study of *L. migratoria* [23] found 76% of hair lengths were < 150 μm, 17% between 150 and 230 μm, and 7% > 230 μm. Across five *S. gregaria* specimens and one *L. migratoria* we found corresponding values of 50%, 34%, and 16% respectively. The longest hairs recorded by Smola were approximately 350 μm, with a mean number of 436 hairs per individual, while our figures were 430 μm and 229 respectively. Therefore, although we found longer hairs,

the overall number is considerably less. Interestingly, our single *L. migratoria* had the smallest number of all specimens. Hair length was significantly shorter in *L. migratoria* than *S. gregaria* (two-sample t-test: $p < 0.0001$; $t_{1371}=6.54$), meaning the hairs will not protrude as high through the boundary layer. However, as we demonstrated in Chapter 3, flow direction is consistent through the range 50 – 350 μm (Figure 36), thus shorter hairs are still likely able to detect similar flow changes to longer hairs.

4.4 Conclusion

In this chapter we developed a successful methodology for imaging five *S. gregaria* and one *L. migratoria*. Although the trial parameter experiments were time-consuming, our final protocol and simple staining technique have allowed us to map the entire array of trichoid sensilla. These data enabled us to characterise the length, number, and, crucially, the peak directional sensitivity of each hair. The latter provides us with a 3D map of the directional tuning of the entire flow sensing system on the head. These highly detailed results are vital in understanding how the locust's sensory systems are locally optimised for their role in flight control. The qualitative analysis presented above demonstrates that the HSVs in fields F1 and F2 largely point posteriorly, with a slight lateral offset, suggesting the hairs are well oriented to sense sideslip. F4 and F5 HSVs tend to point laterally, while F3 HSVs point dorsally. These data suggest the direction of curvature of sensilla in F3-5 are approximately orthogonal from the flow direction expected during equilibrium forward flight. In the next chapter, we combine HSV and CFD data to explore these relationships quantitatively.

Chapter 5

Tuning of sensilla directional sensitivity to airflows

5.1 Introduction

The final and unifying step in our analysis of the role and optimisation of the trichoid sensilla is to examine whether the hair sensitivity vectors (HSVs) are tuned to the local flows they receive in flight. Our analysis begins by aligning our averaged CFD flows from Chapter 3 with the HSVs from Chapter 4, and projecting these vectors onto the main 2D plane of interest for each field, thus simplifying comparison between datasets. By using established techniques for circular statistics, we test for significant patterns in the distribution of HSVs relative to the respective airflow over each field. We also look for significant differences between fields and individuals, as well as evaluating the correlation between curvature and lean measurements, and between both sides of the locust head.

Following these tests, we develop a simple model to quantify the expected hair neuron spike rate based on flow direction and speed. The basis for the model is the set of neurophysiological recordings made by Camhi on a small number of trichoid sensilla [21].

Camhi made recordings using pipette electrodes slipped over the cut tip of individual sensilla while they were stimulated by a continuous airstream varying between through three airspeeds (1.5, 3.0, and 4.5 ms^{-1}) and a wide range of sideslip angles. We have presented his resulting tuning curve in Chapters 1 and 4, which demonstrates a clear dependence of hair neuron spike rate on airspeed and flow direction. As noted in Chapter 4, because Camhi recorded the 'plateau spike frequency' (the spike frequency recorded after the initial 0.25 s of stimulation by airflow), his data represent the partially adapted responses of the hairs under static flow conditions. This distinction is important in considering the roles of the hairs based on our model.

Having applied our static model, we examine the response properties of the hairs and follow with a discussion of flow sensing in the broader context of multi-modal sensing for flight control. In particular, we consider the fusion of information from the trichoid sensilla with that from the visual and force modalities also used in flight control, at the level of the descending interneurons.

5.2 Methods

Before any comparison of HSVs and CFD flows, the orientations of the XMT and CFD geometries were first aligned. Although separate locust heads were used for the CFD and XMT scanning, it was possible to match accurately the heads' orientations given the high degree of similarity in geometry between individuals. The point clouds defining the XMT and CFD head surfaces were rotated and translated with respect to each other, under a rigid body transformation, so as to minimise the mean squared distance between them using an unconstrained nonlinear minimisation. All HSV vector data were then rotated using the final output Euler angles of the matching process, thereby orienting them relative to the CFD vectors (Figure 52). All five *S. gregaria* heads were aligned in this manner.

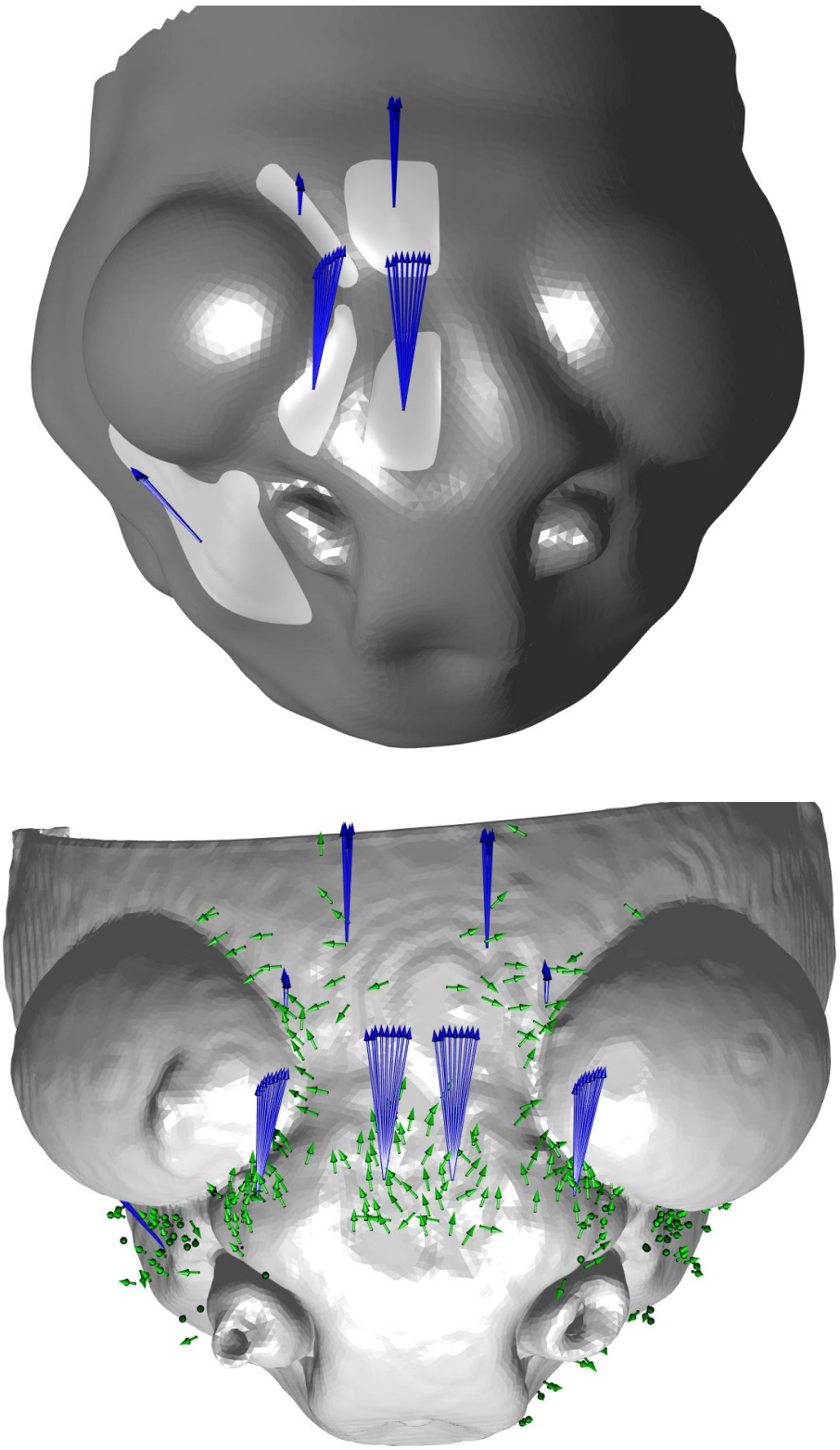
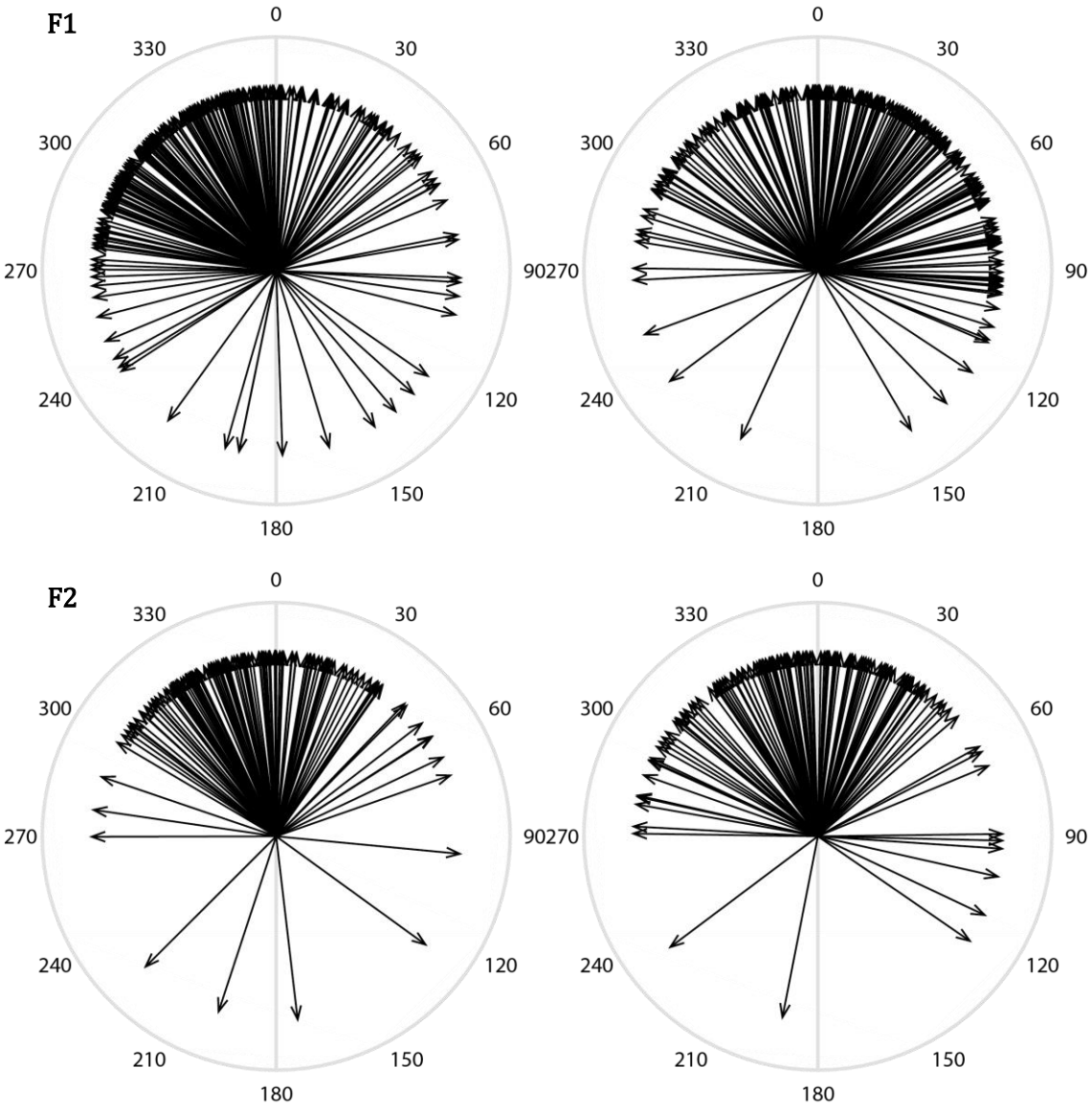


Figure 52: Top: Dorsal view of the CFD head geometry and measured flow vectors over each of the five hair fields at every sideslip angle. Bottom: A XMT head, with all HSVs (green) and all sideslip flow vectors (blue), demonstrating that the XMT data have been accurately rotated to match the CFD data, allowing direct comparison. Note, CFD vectors are shown on both sides of the head for the XMT case.

5.3 Results

In order to compare each hair's peak sensitivity vector with the CFD flow vectors for its respective field, we first reduced the dimensions from 3D to the main 2D plane of interest by projecting all the CFD and HSV vectors onto the 2D planes defined for each field when calculating the hair lean (see Chapter 4: Finding the direction of hair lean). The compass plots in Figure 53 display the relationship between these 2D projected curvature HSVs and the reference CFD flow (i.e. the flow vector at 0° angle of attack and sideslip for that particular field).



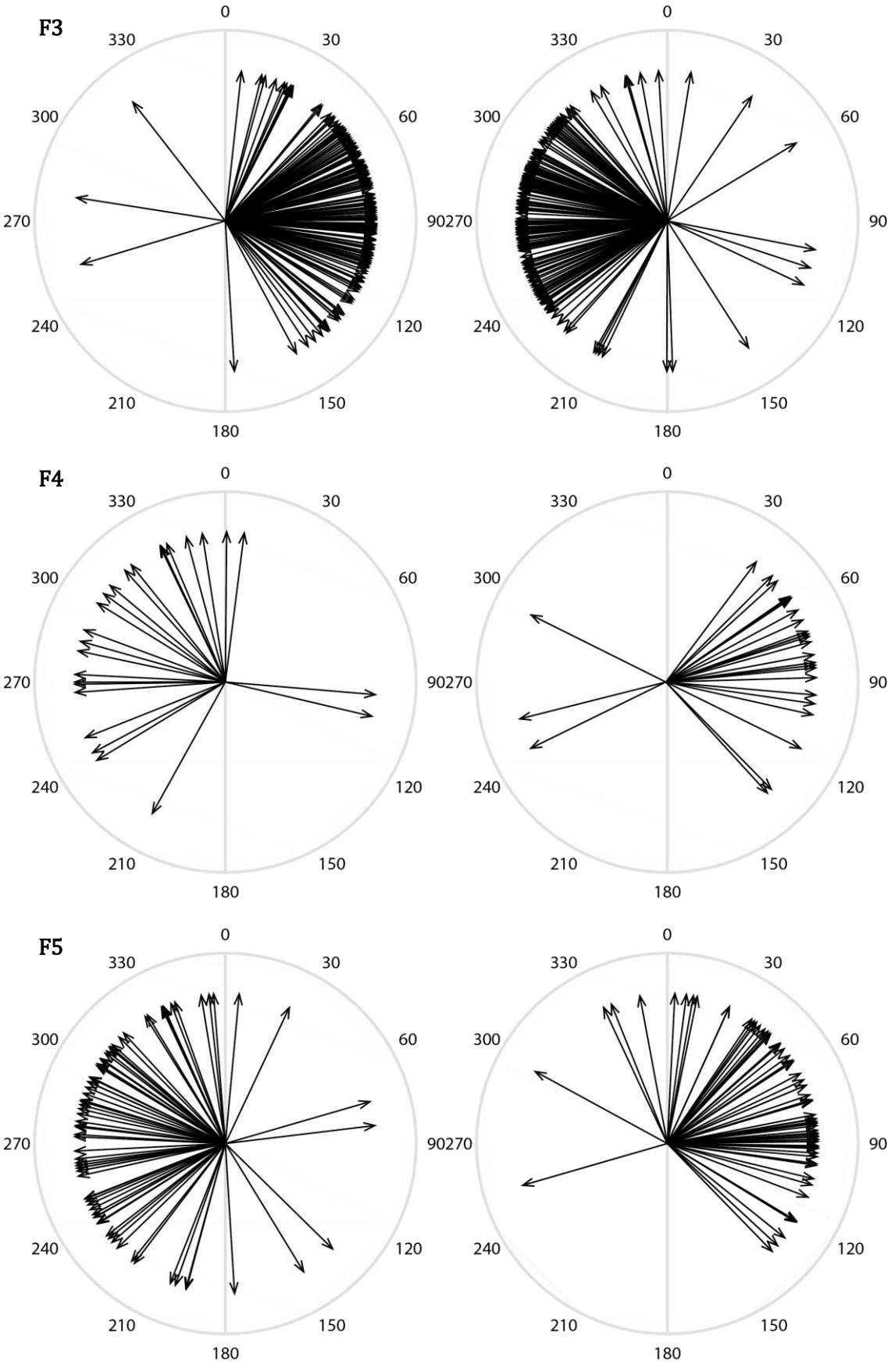

F3
F4
F5
0
30
60
90
90270
120
150
180
210
240
270
300
330

Figure 53: All curvature HSVs from all S. gregaria for each field relative to the reference CFD flow (the flow at 0° angle of attack and sideslip) over that field. Left hand column is the five fields from the locusts' right side, and the right hand column from the locusts' left side (i.e. the top row displays the HSVs from F1 on both sides of the head). The magnitudes are normalised as the effects of the degree of curvature on the response of the hairs are not known.

It is clear from comparing pairs of fields on each side of the head that they appear approximately symmetrical (in the sagittal plane of the locust). This pattern is particularly evident for F3-5, where HSVs tend to have a large offset relative to the 0° medial line. As we do not expect any systematic differences between pairs of fields on different sides (other than this symmetry), the statistical tests presented below use HSVs averaged across both sides of the head (accounting for the symmetry), giving just five sets of data for the five numbered fields. To condense the data in Figure 53, the compass plots in Figure 54 display just the circular mean HSVs (by field) relative to the reference CFD flow using the combined HSVs from both sides of the head.

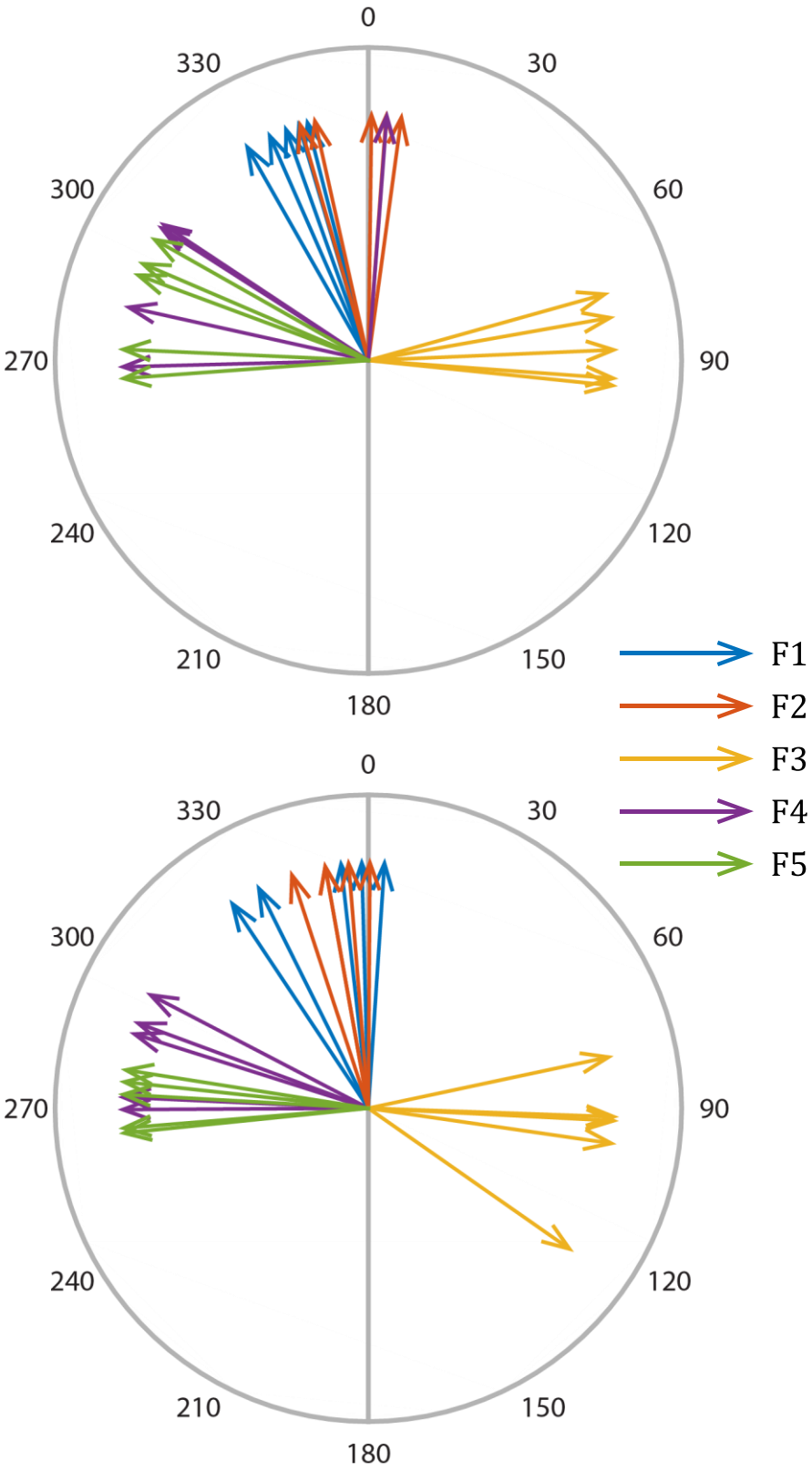


Figure 54: Mean HSV (top: curvature, bottom: lean) for each field relative to the reference CFD flow (the flow at 0° angle of attack and sideslip) over that field. Colour designates field number, with five arrows for each field as we have data from five individuals. As in Figure 53, vector magnitudes are normalised.

Figure 54 demonstrates the relative consistency of HSV direction between different individuals within a particular field; they all point approximately the same direction. Additionally, both curve and lean measurements yield similar overall directions.

The maximum difference between the mean HSVs of hairs in F1 and F2 is within 35° relative to the reference airflow over their fields for both curvature and lean. There is also an overall directional offset away from the medial line. F3-5 HSVs clearly point approximately orthogonally to the airflow they would receive at 0° angle of attack and sideslip. There is one discrepancy to this pattern – a single F4 arrow in the curvature dataset is pointing at approximately 0° (Figure 54, top). This discrepancy is not found in the lean dataset, signifying a clear difference between the two measures. In the following section we test for correlation between curvature and lean HSVs between all fields. The vector length (signifying the amount of curvature/lean) varies within and between fields, however, it is not known whether this translates to varying response properties of the hairs.

The significance of the apparent patterns in the complete (Figure 53) and averaged (Figure 54) data were tested using the circular statistics toolbox by Berens [149] for use in MATLAB. This toolbox is based on established techniques for circular statistics, most of which can be found in [150].

Are HSVs distributed uniformly?

Although qualitatively clear from the above compass plots, we can test numerically whether the arrangement of HSVs has some directional bias. The appropriate test was the Rayleigh test [149, 150] and asks the question, whether a population of vectors is distributed uniformly around the circle (the null hypothesis). Using the complete dataset, we combined all HSVs across all individuals and tested for uniformity separately for each field. At the 95% confidence interval, p-values for all fields were significant, rejecting the null hypothesis and confirming HSVs of all hairs within each field are not distributed uniformly (i.e. they do have some directional bias) (Table 2).

We also quantified the level of variability in each field by calculating the mean resultant vector length (R). This quantity describes the concentration of the data around the mean direction and is crucial for measuring circular spread and hypothesis testing in directional statistics [149]. The closer the value is to one, the more concentrated the data. The value is directly related to the circular variance (S): $S = 1 - R$. Our calculated resultant vector lengths reveal all fields show a high degree of concentration about the mean direction, with the highest value found in F3 (0.84) and lowest value in F4 (0.66) (Table 2).

Field	Sample size	z-statistic	p-value	Resultant vector length (R)
F1	416	190.61	<0.001	0.68
F2	270	166.86	<0.001	0.79
F3	367	256.25	<0.001	0.84
F4	54	23.83	<0.001	0.66
F5	141	69.42	<0.001	0.70

Table 2: Output of Rayleigh's tests for each field (combining data from all five locusts) and resultant vector lengths.

Do HSVs vary across hair fields and between individuals?

The key question we want to ask is do the HSVs of different number fields (F1-5) differ from each other? It is also important to determine whether there are significant differences in the HSVs across individual locusts. Although both these questions could be addressed in separate one-way ANOVAs, we can test for both, and their interaction, using a Harrison-Kanji test – the equivalent of a two-way ANOVA for circular statistics [149, 151, 152]. Once again, this test was carried out using the complete dataset containing every individual HSV.

The output from the Harrison-Kanji test yielded $p < 0.001$ ($X^2_8=255.76$) for field number and $p = 0.65$ ($X^2_8=5.94$) for individual. We can therefore conclude that there are significant differences in the mean HSV between different field numbers, and no significant difference between individuals. There is, however, a significant interaction effect between field and individual (Table 3).

Source	d.f.	X^2	p-value
Field	8	255.76	<0.001
Individual	8	5.94	0.65
Interaction	16	42.42	<0.001

Table 3: Output from Harrison-Kanji test (sample size = 1248). Degrees of freedom are multiplied by two as a necessary correction for the small kappa value (describing the concentration of the data points about the circular normal distribution) calculated from the dataset (see [151]).

Do different side fields have similarly oriented HSVs?

Although we pooled pairs of fields in the above analysis, we can explore the relationship between HSVs of the two separate sides. Figure 55 plots the mean HSVs for all five fields on both sides of the head using both curvature and lean data, using the same colour scheme as the earlier compass plots (colour denotes field number).

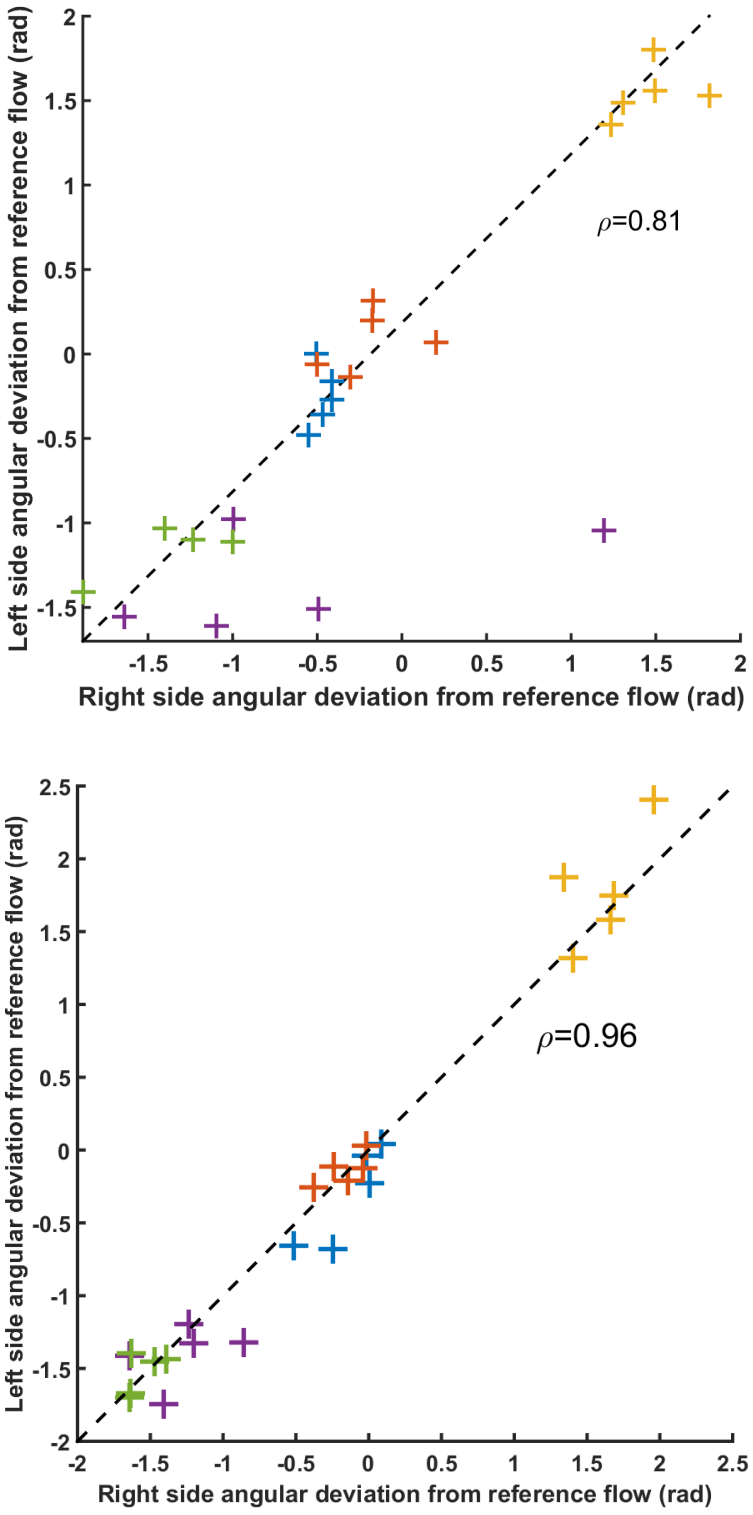


Figure 55: Exploring the relationship between HSVs (based on direction of curvature) on the left and right sides of the head relative to reference flow vector (angles in radians). There is a clear positive correlation over the datasets for both direction of curvature (top, ρ=0.81) and lean (bottom, ρ=0.96). Colour indicates field: F1 = Blue, F2 = Red, F3 = Yellow, F4 = Purple, F5 = Green. The dotted line has a slope of 1:1 (i.e. where points would fall under perfect correlation).

The plotted values of the circular-circular correlation [153] demonstrate a strong correlation between the two sides, with coefficients of 0.81 and 0.96 for curvature and lean measures respectively. Therefore, we can conclude pairs of fields have HSVs arranged at very similar offsets relative to reference flow (both sides are highly symmetrical). However, we do see clear differences in the angular deviations for F4 (purple) between the sides with the curvature measurements. The low number of hairs in F4 (n = 11) makes any statistical comparison less robust.

Do curvature and lean measurements show correlation?

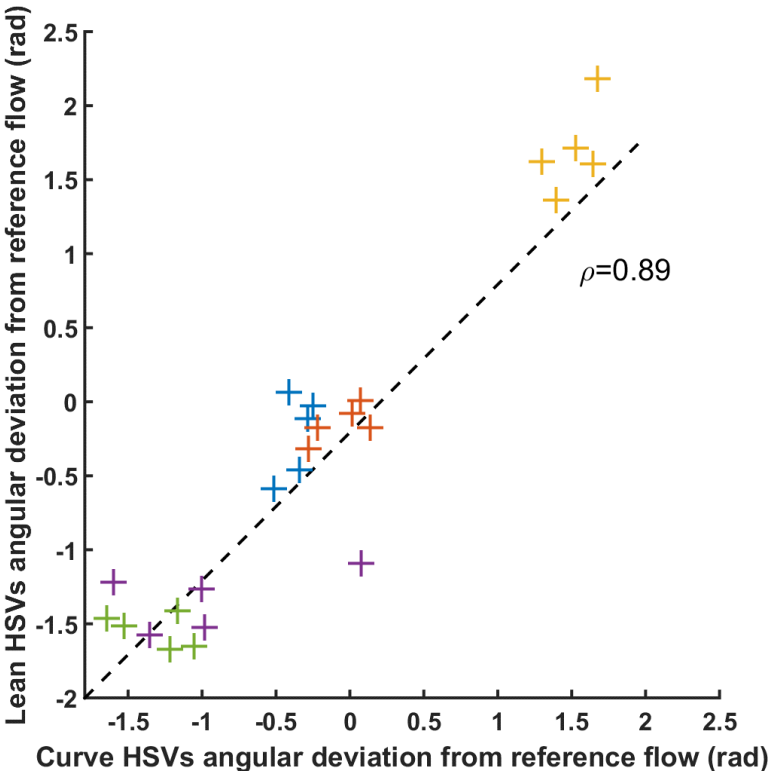


Figure 56: Exploring the relationship between curvature and lean HSVs relative to reference flow vector (angles in radians). There is a clear positive correlation over the whole dataset (ρ=0.89). Colour indicates field. The dotted line has a slope of 1:1 (i.e. Where points would fall under perfect correlation).

Using the identical approach, Figure 56 explores the relative angles between curvature and lean hair measurements. Again, we see a strong correlation (ρ=0.89), confirming there is little difference between direction of curvature and lean measures. They therefore both

likely provide an accurate measure of the peak directional sensitivity of hairs, as the direction of curvature is already an established method to calculate this quantity. The single discrepancy between curvature and lean that we noted in Figure 54 is evident in Figure 56 (one purple data point is some distance from the line of 1:1 correlation), however, this is appears to be the only outlier.

5.4 Discussion

How are airflow stimuli transduced by the locust?

At this point, we can infer how we might expect hairs to interact with airflows when considering their peak directional sensitivity (HSVs). We can say with some confidence that locusts have airflow sensors that will be stimulated under distinctly different conditions – F1 and F2 to small deviations from the reference forward flight conditions, and F3-5 to larger, orthogonal perturbations (Figure 54). Sensors are often arranged orthogonally (in relation to other sensors, and to the major axes of the vehicle) in manmade aerial vehicles because this confers equal sensitivity to motions in any direction, in addition to simplifying signal processing, whilst non-orthogonality is common in insects [74]. Our data suggest that locusts exhibit both regimes: HSVs in F1 and F2 are arranged non-orthogonally relative to the flow expected during equilibrium flight, while F3-5 are arranged orthogonally.

However, we know from previous neurophysiology work that the hair neurons will also be firing at a range of angles around the peak HSV measures, and therefore we should consider situations other than just our reference condition. Camhi's [21] work demonstrated the response properties of hair neurons elegantly, generating a symmetrical and clear tuning curve of the number of spikes relative to airflow sideslip angle under static conditions (Figure 57 (i)). The arrow in Figure 57 (i) represents the direction of the hair curve (13°) relative to the longitudinal axis of the locust, and it is clear maximum spiking occurs from airflow in that direction. Each of the three sets of points in Figure 57 (i) correspond to

different airspeeds, revealing the approximately linear relationship of spiking with flow speed.

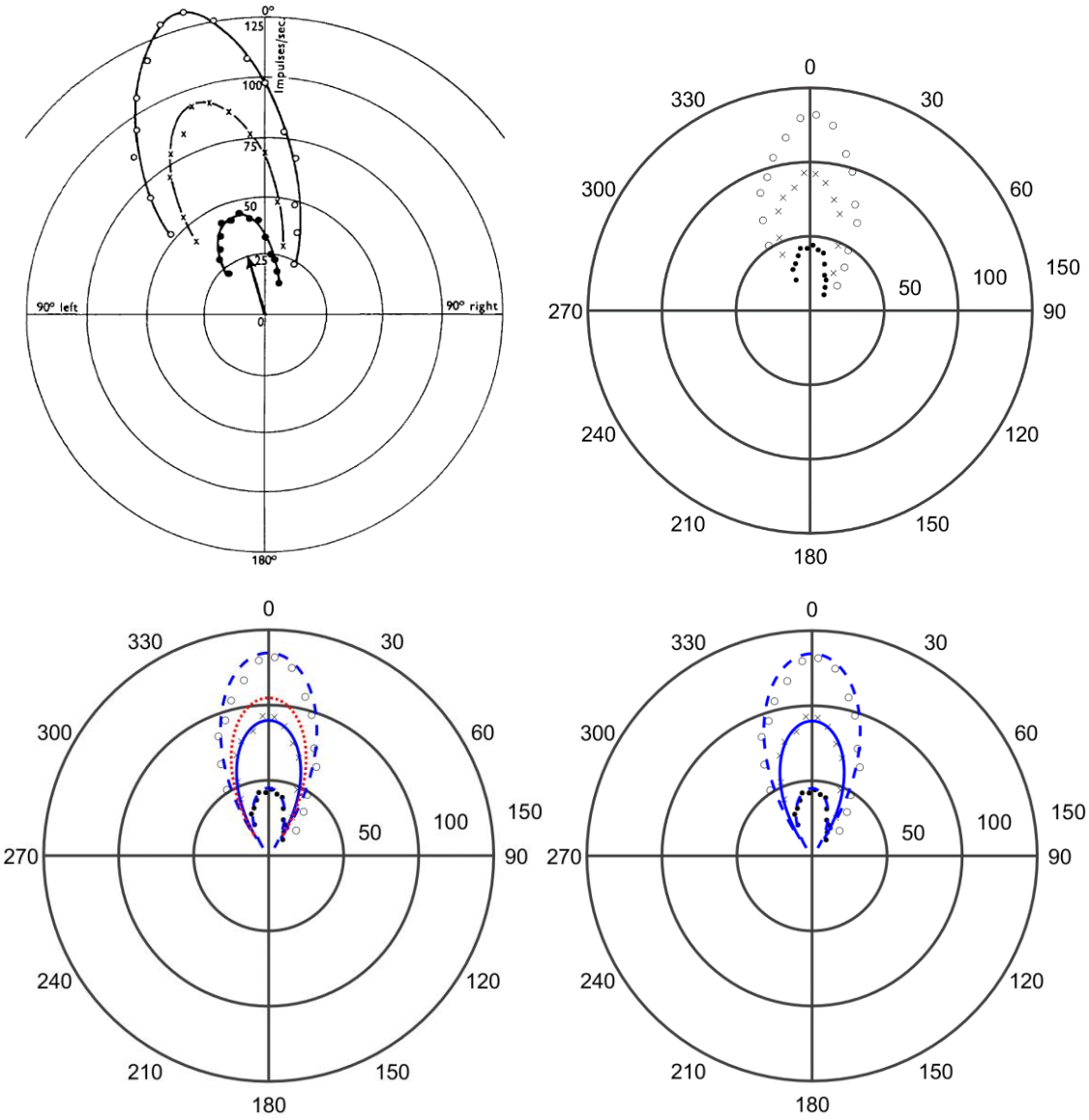


Figure 57: Clockwise from top left: (i) Camhi's original tuning curve [21], showing number of neuronal impulses against angle of airflow. The arrow represents the direction of this particular hair's curvature. (ii) Our digitisation and normalisation to 0°. (iii) Our fitted curve to the middle set of data (solid blue line). We then scale the curve based on the input airflow speed (e.g., Two dotted lines are the curves based on flow speeds of the other two sets of impulse readings). (iv) Red dotted line is the curve for the equilibrium flight speed of locusts [121] (and our CFD flow speed) of 3.3 ms^{-1}.

Using these data, we produced a simple model for predicting spike rate. Firstly, we digitised the data in MATLAB and rotated them to be about 0° in relation to the longitudinal axis of

the locust (Figure 57 (ii)). Camhi [21] fitted a curve to his data but provided no information on its form or equation. We estimated that the data approximately fit a cosine double angle ($\cos 2\sigma$, where σ is the angle between the HSV of the hair and oncoming airflow). One possible explanation for this form may be found in considering that under the double angle formula, $cos\ 2\sigma$ is related to $cos^2\ \sigma$. Therefore, as an example, the projection of the airflow onto the hair, defined by $\cos \sigma$, multiplied by a $\cos \sigma$ mechanical response in the hair socket could feasibly produce this shape of response.

We used $\cos 2\sigma$ as a starting input condition for a nonlinear least-squares curve fitting to the data:

$$\hat{y} = a * u * \cos(b * \sigma)$$

with the minimisation defined as $\sum(y - \hat{y})^2$ where y was the measured response and $\hat{y}$ the modelled response. a and b were the coefficients to optimise, $u =$ airspeed, and $\sigma =$ angle. Polar plots of $\cos\ b\sigma$ produce a rose curve with the number of 'petals' related to the value of b. In our case, we only need the one 'petal' that corresponds to our dataset, and therefore the angle values were bounded to remain within these limits. We fitted the curve to Camhi's middle dataset (solid blue line in Figure 57 (iii)) as this airspeed, 3.0 ms^{-1}, was closest to that used in the CFD (3.3 ms^{-1}). Having solved for the two coefficients ($a = 29.93, b = 2.30$), we could use our model to produce the response curve for any given airspeed (u). For example, the blue dotted curves in Figure 57 (iii) show the predicted spike rates for the other two flow speeds used by Camhi (1.5 and 4.5 ms^{-1}), while the red curve in Figure 57 (iv) represents the angles and neuron impulses we would expect a hair to have when stimulated by airflow at the 3.3 ms^{-1} CFD speed.

By applying this model to the CFD and mean HSV data over each of the fields, and at each of the angles, we calculated the expected neuronal impulses at each angle of attack and sideslip (Figure 58).

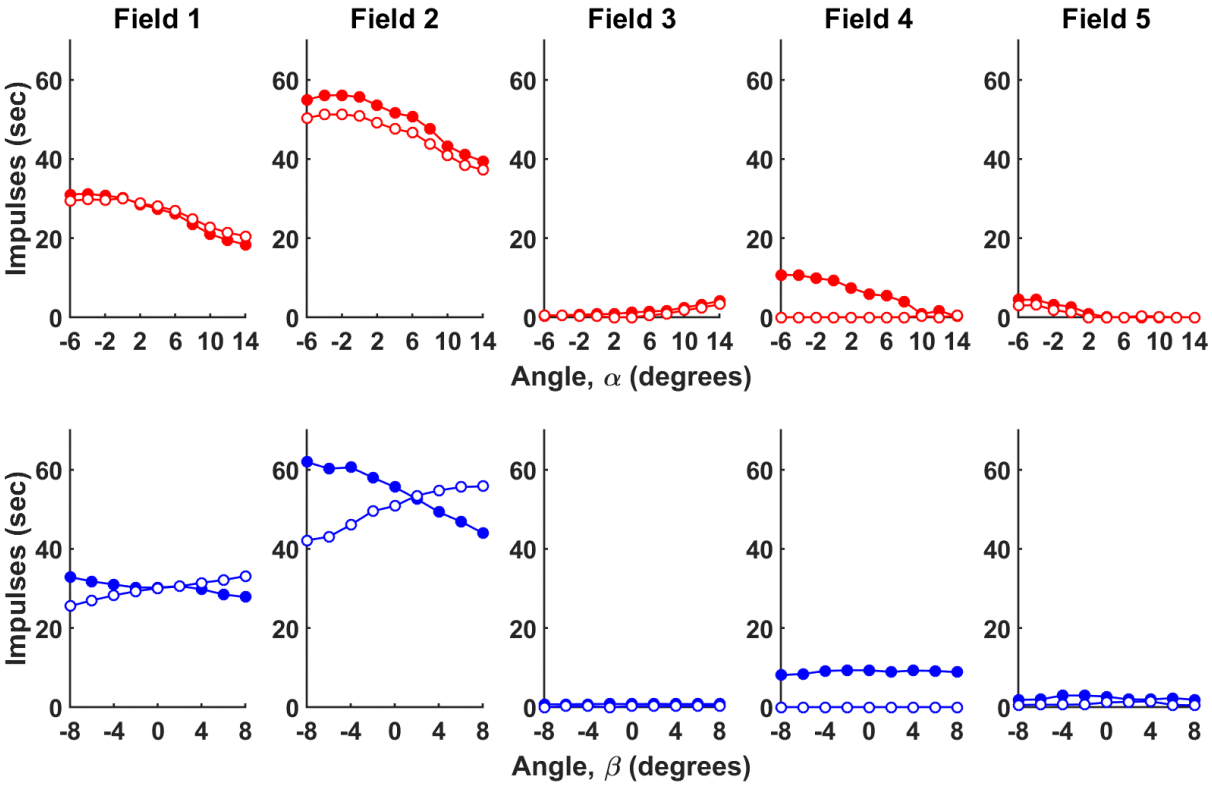


Figure 58: Predicted mean impulses per second for each field, based on angle of the head relative to airflow. Top row: angle of attack, bottom row: sideslip angle. Filled markers represent measurements from the right side of the head, and open markers from the left.

According to our model, we expect the hairs in F1 and F2 to respond at all times through the range of angles of attack, with a negative correlation between number of impulses and head angle. This pattern is easily explained; flow separation at high angles (as demonstrated in Figure 39) caused a decrease in flow speed, and hence a reduced spike rate. Therefore, in this case, changes in spike rate are induced by changing flow speed as opposed to direction. Little to no firing is expected in F3-5 due to the narrowness of the tuning curve – no impulses are expected beyond about 35° either side of the HSV for a hair (Figure 57). As we have shown, the HSVs in F3-5 lie approximately orthogonal to the reference flow and, therefore, the range of angles we have used is not wide enough to cause significant spiking (although F3 begins to show a response at high angles). We do still see the effects of flow separation over F4 and F5 at high angles of attack, with their spiking going to zero.

In the case of changing sideslip, as the head is moved from -8° to 8°, the impulses per second decrease approximately linearly for F1 and F2 on the right side of the head, and *vice versa* on the left. This pattern is the result of changing flow direction relative to HSVs in these fields. It nicely illustrates the strong correlation found between left and right side hair field pairs in our analysis above (because HSVs are approximately mirrored between pairs of fields). Once again, our model predicts little response in F3-5 over the whole range of sideslip angles due to the large angles between HSVs and the CFD flow.

These plots confirm our hypotheses as to the role of F1 and F2; it seems very clear that both fields could detect changes in sideslip (through hairs responding to changes in angle), or sense changes in angle of attack (through hairs responding to changes in airspeed). The positioning of the mean HSVs in these fields (within 35° of the reference airflow) seems optimal for detecting sideslip deviations - we expect little firing at the locust's equilibrium flight angle, but increasingly higher firing rate with deviations around this point. This arrangement makes sense energetically as neurons would not be firing maximally during equilibrium flight conditions.

One caveat with our model is that it was produced using neurophysiological recordings made under static conditions, after the response of the neuron had already rapidly adapted. Therefore, the data in Figure 58 represent static response curves. It would prove a useful point of comparison to produce a tuning curve of a hair's response using dynamic conditions, where the initial higher spike rate of the cells was recorded. We are working under the assumption that a similar relationship with airflow speed and direction would emerge. Dynamic recordings are particularly relevant in reference to the dynamics models we develop in Chapter 7, which involve motions on timescales fast enough that adaptation should not kick in.

The narrowness of the tuning curve has implications for our hypotheses as to the role of fields F3-5. As these hairs appear close to orthogonal relative to equilibrium forward flight conditions, they seem unlikely to be used for flight control in this scenario. Extreme angles

relative to oncoming flow would indicate very large deviations from equilibrium flight conditions and intuitively sensors that respond to small disturbances before reaching this point (such as F1 and F2) would be more effective in maintaining successful flight orientation. What role may the other fields then play? Of these three fields, F3 has a distinctly higher number of hairs and thus it does seem likely it is of some importance. As these hairs are located on the vertical plane, while the locust is descending it is likely hair neurons will be firing (although not during ascent as they do not respond 180° relative to their HSV [21]), therefore they may be used in landing after flight or jumping. It is more difficult to pin a specific role to F4 and F5, both of which are located on the horizontal top head surface. They may be well situated to monitor induced flows by the beating wings as they are positioned further downstream on the head than F1 and F2 and are therefore closer to the wings. The low number of hairs in F4 – often <10 even when combining all F4 hairs on both sides – may suggest their lack of importance, particularly as a whole field of hairs is usually considered as the single sensory unit, as opposed to an individual sensillum, based on response properties and neuronal projections to the descending interneurons [17].

As a final exploration, we also carried out a brief ontogenic study in the form of microscope observations of the trichoid sensilla, which confirmed their presence through all instars (Figure 59). Wings do not develop until the final adult stage, perhaps suggesting an additional non-flight related role for the hairs.

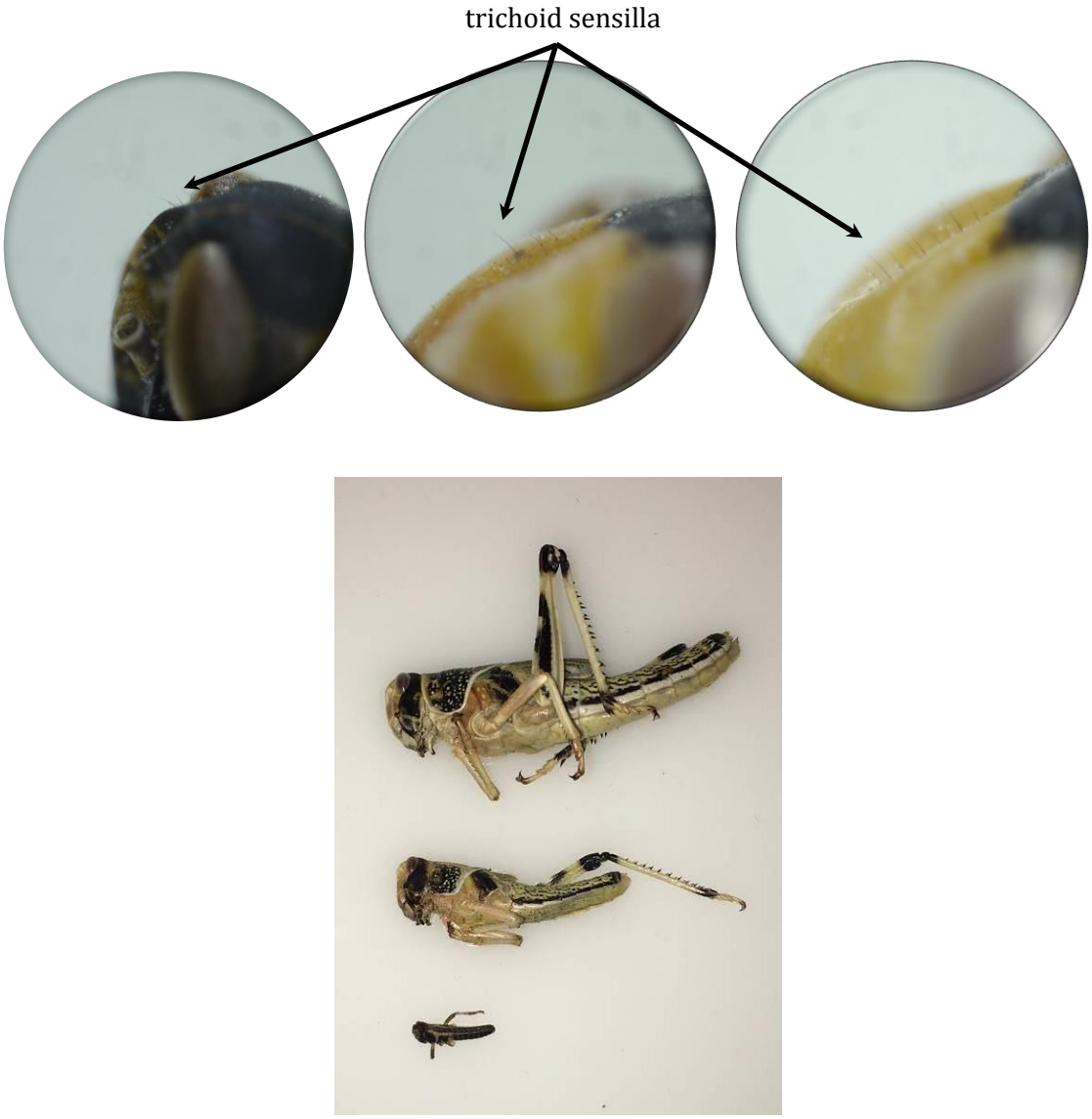


Figure 59: Top: microscope photographs of cephalic trichoid sensilla visible through the 1st, 3rd, and 5th instars (left to right). Bottom: complete body lateral view of all three instars.

Flow sensing in a broader context

Under the assumption that Camhi's [21] characterisation of the neuronal response of a handful of hairs applies to all hairs on the head, we have inferred the sorts of sensory information the locust could sense in relation to various flow conditions. However, it is crucial that we also consider how this information is subsequently transduced to some useful form for the insect.

Firstly, the information these hairs provide should be considered in the context of *changes* in flow (transduced as changes in neuron spike rates) as opposed to any absolute measure of the flow vector. As mentioned in the Chapter 1, there are several explanations for why insect sensors do not measure absolute quantities. In the case of the trichoid sensilla, their high sensitivity to temperature and adaptation of the neuronal response [21] would both require some record to be kept of their changing gain functions in order to produce an absolute measure. Crucially, the tuning curve reveals that a hair cannot be used to provide an independent measure of solely airspeed or flow direction. For example, it would not be possible to disambiguate a slower flow from a flow at a greater angle relative to the hair's axis of peak sensitivity.

In addition, it is unlikely that changes in angle of attack or sideslip are explicitly coded in a fashion that directly influences motor responses. No hair neurons directly synapse with motor neurons. Instead they attach to numerous pairs of descending interneurons (DNs) that bring sensory information relevant to flight control to the thoracic motor centres (synapsing with motor neurons and pre-motor interneurons) [154]. As a group, the DNs also receive input from the ocelli, compound eyes, and neck proprioceptors, as has been demonstrated by recording the response intracellularly to visual and aerodynamic stimuli [37]. Individual DNs are known to receive input in varying combinations of all these – some respond to just one modality, for example wind stimuli, others receive input from all four, and yet more a varying combination of just two or three (an excellent summary can be found in [15]). As we discussed in the introductory chapter, some individual DNs exhibit clear

directionality in their response to stimuli, for example 3 DNs (DNI, DNM, DNC) all respond to visual and wind inputs, but DNI responds optimally to diving banked turns, DNM to downwards pitch, and DNC to diving banked turns to the contralateral side [37]. There is also a complex co-dependency in the response to input stimuli with DNs that combine multiple modalities. For example, input to the ocelli can suppress responses to compound eye or trichoid sensilla stimuli, while the response of the trichoid sensilla in daylight is approximately one tenth that in dim light [37]. These DNs have been well characterised in their role in corrective steering of locusts (with their output to motor neurons being shown to control wingbeat and abdomen and hind leg ruddering), acting analogously to an autopilot to deal with deviations from set course [15], therefore multi-modal inputs are undoubtedly involved in flight control.

Accordingly, although the trichoid sensilla are demonstrably a key component in flight control [24, 30-32], and the aerodynamic flows over the head are transduced in the spike rate of individual hair neurons [21], it may be incorrect to think that this information independently plays a dominant or even a direct role in flight control. It is the case that some DNs only respond to flow stimulation of the trichoid sensilla [34], and previous work has demonstrated that stimulation of just a single DN is enough to create steering behaviours [155]. However, it is unlikely that only a single DN would be stimulated at any given time during free-flight, and therefore any motor output is still almost certainly the result of a combined input of multiple DNs from multiple sensory modalities. There also remains the key unanswered question of how spike information from the neurons is processed by the DNs, and how this input relates to an output signal to the motor neurons. Using Camhi's previous neurophysiology experiments on individual sensilla we have given numerical values to the possible spike rates. Thus, we already have an idea of the quantitative inputs to the DNs from one input. Previous work on lobula plate tangential cells has provided a similar quantitative characterisation of the visual system in flies (indeed, Huston and Krapp [140] provide similar vector map representations of the directional sensitivity as we have presented in Figure 47). A similar scrutiny of the visual system in locusts seems to be a

logical next step. As we know various DNs respond to just visual and trichoid sensilla inputs, further work to quantify visual inputs could provide a complete numerical dataset for a single DN, helping us unravel how inputs are integrated and processed at the descending neuron level.

5.5 Conclusion

In this chapter, we combined the flow stimulus and sensor sensitivity data into a series of analyses. In the process, we addressed the first two of our research questions posed in the Introduction: *What aerodynamic features of the flow could these sensors be measuring?* and *How have sensor position & directional sensitivity been optimised to monitor features of airflow?* Our data demonstrated clear directional bias in hair sensitivity for all fields, as well as the consistency in response properties across individuals. Additionally, the HSVs of all pairs of fields were approximately mirrored in the sagittal plane of the locust, and both curvature and lean measurements yielded similar results. Our model of hair spike rate enabled us to conclude that fields F1 and F2 are ideally located to act as detectors of sideslip following small disturbances from equilibrium flight. In contrast, assuming our simulated airflows are comparable to *in vivo* conditions, it seems unlikely fields F3-5 are suited to monitoring similarly small deviations. Instead, they are used either to monitor much larger disturbances, or to sense other airflow stimuli, such as those induced by the beating wings or during landing. Our findings in relation to F1 are in accordance with Gewecke and Philippen's behavioural experiments which demonstrated F1 was key in producing a yaw-stabilising reaction in locusts experiencing asymmetric airflows (i.e. with the locust at non-zero sideslip angles) [30]. Additionally, Camhi implicated both F1 and F2 in abdominal ruddering under similar sideslip conditions [31]. Our conclusions as to the role of F3 are at odds with a previous finding that this field was key in the yaw-stabilising reaction [24], as we suggest hairs in F3 cannot be used to sense changes in sideslip. However, this prior finding is itself contradictory to those made by Gewecke and Philippen, and it has been suggested that the latter experiments were carried out with more sensitive apparatus [10].

We believe the approach and results presented above have provided a thorough characterisation of the initial stimulation of these sensors. The obvious corollary of this analysis is, what happens next? And this is the focus of our third research question: *How is this sensory information used in flight control?* As the final section of our discussion concluded, there is clearly considerable scope for further neurophysiological work to understand how these input signals are processed. However, in the next chapter we look at this question from a behavioural perspective, by scrutinising the flight dynamics of locusts under changing aerodynamic stimuli.

Chapter 6

In vivo sensor manipulation

6.1 Introduction

In the preceding chapters, we developed a thorough characterisation of the trichoid sensilla's flow stimuli and directional sensitivity. From these we have inferred the likely roles and function of the five pairs of fields. In this chapter, we look at the behavioural response of locusts by recording the *in vivo* forces and moments generated during tethered flight while varying both the sideslip angle ($-12° \leq \beta \leq 12°$) and the input to the trichoid sensilla (by selectively covering fields). Therefore, while our earlier experiments have looked at the initial inputs to the sensory system, here we examine the final motor output in response to varying input stimuli. Our analyses with these measurements are two-fold: this chapter compares the forces and moments generated by locusts before and after manipulating sensory input to the sensilla, while in Chapter 7 we use these data to examine the locusts' dynamic lateral flight stability.

Sensor manipulation

We have described some of the prior sensor manipulation experiments in Chapters 1 and 5. For reference, we provide a complete summary below:

Weis-Fogh previously found a role for the trichoid sensilla in stabilising yaw by observing that locusts turn into asymmetric airflows when tethered to apparatus permitting rotation in the yaw axis [24]. Covering of the F3 field eliminated this reaction. With most likely more accurate apparatus [10], Gewecke and Philippen [30] found that so long as F1 was left intact, there was always some response, and covering F1 created as strong a suppression as covering the four remaining fields. Camhi [31] found that F2 in particular is linked to changes in abdominal position that occur with varying airspeed – with the abdomen being lowered with decreasing speeds. Covering F2 abolished or greatly reduced this response (as did covering F1 and F3, to a lesser degree). An additional study found that covering F2 also disabled the symmetric movements of the abdomen that occur when varying airspeed [32].

We aim with our force measurements to build on these previous experiments, providing an updated and quantitative approach to understanding the role of trichoid sensilla in controlling sideslip. Using a highly sensitive force balance, we intend to measure forces and moments in six axes (three in translation and rotation). This will allow us to discern the key axes in the response of the locust to varying airflow to the sensilla. Using a high-precision rotary motor, we can provide both static and dynamic changes in sideslip angle with speed and accuracy, representing a significant improvement on previous experimental setups. By following the same convention of selectively covering over the hair fields, we hope to resolve the conflicts in the measured responses between previous studies.

6.2 Methods

Axis system

We define the body axes of the locust using a right-handed axis system, with the origin located at the centre of mass (Figure 60). The x-axis is the longitudinal axis of the locust body, the y-axis is the transverse, and the z-axis is the vertical. The roll (Φ), pitch (Θ), and yaw (Ψ) angles are the Euler angles, defining the orientation of the three body axes with respect to a set of Earth-fixed axes in which the z-axis is aligned with gravity. Sideslip angle (β) is the angle of the locust body relative to oncoming airflow in the z (yaw) axis. Sideslip angle is zero when the body is parallel with the oncoming flow.

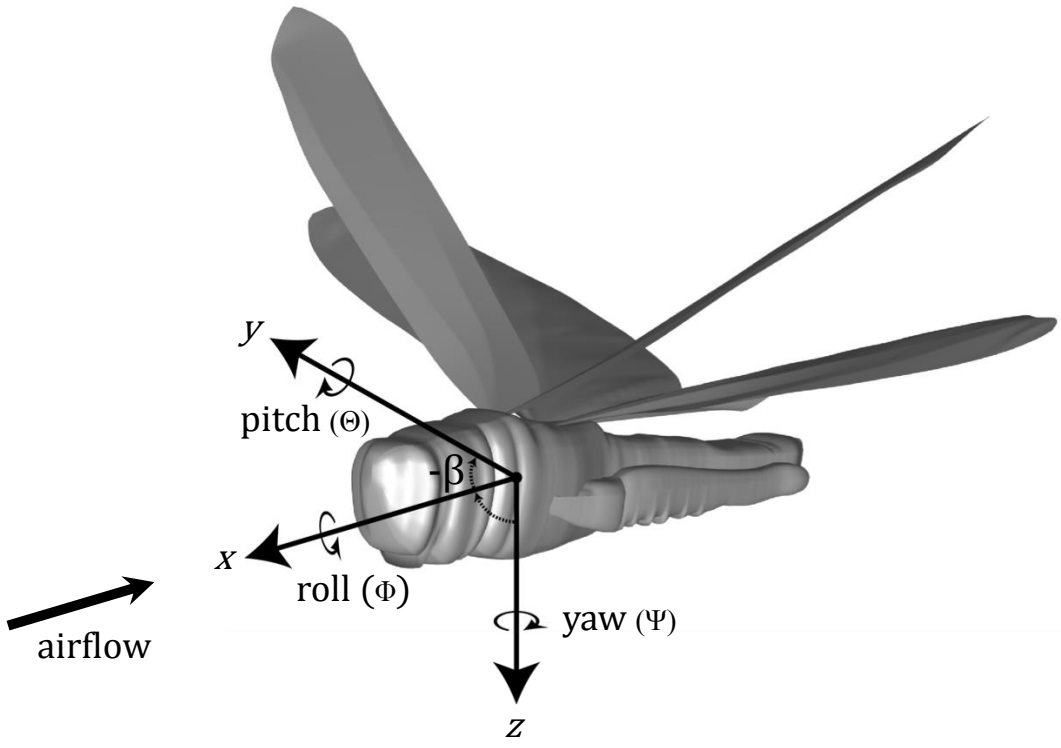


Figure 60: Right-handed axis system used to define the locust's body axes. (Locust geometry courtesy of Dr S. Walker, University of Oxford).

Animals

Four adult gregarious phase desert locusts (*Schistocerca gregaria*) were selected from a population of 150 purchased from commercial supplier Blades Biological (Edenbridge, UK). The population was given two weeks from the date of arrival until trial experiments to allow wings to dry out as they were shipped having newly moulted into their adult phase. Around 100 individuals were tested by tethering them in front of a wind tunnel and the four strongest flyers chosen. The sample size was limited by the requirement of finding individuals that would fly reliably for an entire experimental set.

Tethering

Each locust was tethered to a six-component force-moment balance (Nano17, ATI-IA, NC 27539, USA) placed in front of a wind tunnel providing constant flow speed at 3.3 ms^{-1}. Locusts were cemented ventrally to the tether at the plastron of the pterothorax using cyanoacrylate adhesive (Figure 61). The tether was custom-made with a slant to position the body at 7° relative to the ground (i.e. at $\Theta = 7°$); an angle previously found to consistently stimulate full flight posture with lift balancing body weight [121, 124, 156, 157]. Recordings were only made when the locust was in full flight posture, defined by Weis-Fogh as when "*the antennae are stretched obliquely forwards, the forelegs are drawn up, the middle legs and the hind femora are stretched backwards along the abdomen, the hind tibiae are drawn up against the shallow groove on the underside of the femora, and the abdomen points straight backwards in continuation of the pterothorax*" [124].



Figure 61: Locust in full flight posture while tethered to a mount at $\Theta = 7°$. The mount itself is secured to a 6-DOF force balance housed in the circular silver base. The six channels from the balance are connected to a signal conditioning amplifier via the black cable. The force balance is rigidly fixed to the centre of rotation of a precision rotary motor, allowing sideslip angle (β) adjustments. Airflow travels from left to right in this view.

Force measurements

The force balance itself was tethered to the centre of rotation of a precision rotary motor, allowing static and dynamic varying of the sideslip angle (β). The balance consists of strain gauges arranged to provide six individual channels, each with half Wheatstone bridge arrangement. Each of the channels was attached to a bridge amplifier (2210A Signal Conditioning Amplifier/2250A Rack Adapter, Vishay Measurements Group, NC, USA) providing 5V constant voltage excitation. Each output was filtered online with a 1kHz low-pass hardware filter, sampled at 10kHz using a 16-bit analogue-to-digital converter (PowerLab/16SP, ADInstruments, Pty Ltd., Castle Hill, NSW, Australia), and recorded at 12 bits in Chart 5 (ADInstruments) on a Windows PC. A seventh channel also recorded the angle of the rotary motor (received from the motor driver as an analogue voltage output from the rotary encoder) in order to accurately match angle and force data in analysis (Figure 62).

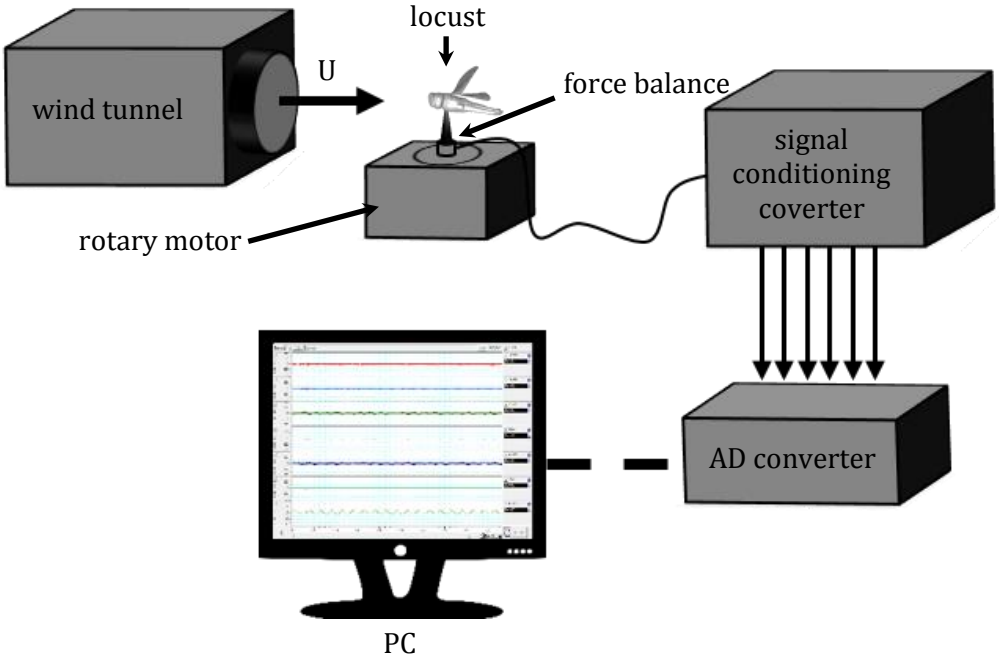


Figure 62: Experimental setup. The locusts were tethered to a six degree of freedom force balance which was itself attached to a precision rotary motor. The six output channels were fed into a signal conditioning amplifier and an analogue-to-digital converter before being recorded on a PC. A seventh channel outputted the encoder position of the rotary motor. Airflow at 3.3 ms^{-1} was provided by a wind tunnel.

Flight conditions

As this experiment concerned responses to airflows, visual inputs were minimised. We used black shielding and cloth to remove any external light source. Low-level (20 lux) red lighting has previously been shown to give reliable flight performance [121, 124] and was provided by overhead LED panels and a diffusing circular red Perspex sheet. The centre of the circular sheet was positioned above the centre of rotation of the rotary motor. Therefore any rotation of the locusts (whose heads were very close to the centre of rotation) should not cause major shifts in the perceived position of the light source. Standard temperature and humidity conditions of 29°C and 35% respectively were maintained throughout.

Measurement series

Voltages from all channels were recorded under static and dynamic stimuli. First, a series of randomised static angle changes in the range -12° ≤ β ≤ 12° (in two degree increments). Each motor position was held for 15 seconds. After each position, a zero degree recording was made to provide a relative zero measurement to account for any drift in the force balance output over time. Following static angle shifts, dynamic sinusoidal stimuli were used over the same angular range, and over a range of frequencies (0.125, 0.25, 0.5, 1, 2 Hz). We used 2 Hz as the upper limit as oscillations beyond this frequency tended to cause flight failure.

Measurements were then repeated, but with progressive removal of sensory input to the trichoid sensilla, achieved by painting over pairs of hair fields using liquid latex (which rapidly solidifies in air). Hair fields were treated in three groups – {F1 and F2}, {F4 and F5}, and {F3}. The decision to use this grouping reflects three considerations: (i) Although previous literature has established a quintuple nomenclature, when classified according to central neuronal projections, the fields form only these three groups [33]. (ii) Our detailed XMT and CFD analysis in Chapters 2-5 suggests that this grouping more accurately reflects the potential roles of different fields, e.g. F1 and F2 seem arranged to capture similar aerodynamic stimuli. (iii) Coaxing locusts to fly for a more fine-grained set of individual field coverings pushed their flight endurance too far. We had significant difficulty in acquiring just four individuals to fly for the requisite time using these three groups. The order in which fields were covered was varied between individual locusts.

Following covering of all fields, a final set of static and sinusoidal measurements were taken with the latex removed. Although the latex solidifies, it peeled off with minimal effort. We confirmed with light microscope observations that removal of the latex did not significantly alter the physical appearance and orientation of the trichoid sensilla. Therefore, assuming the latex had no effects on the neuronal response, we predict that its removal should return normal function to the sensilla.

A complete set of recordings required approximately 45 minutes of flight.

Conversion of force balance output to force-moment data

Balance calibration

To convert the voltage readings from the six channels of the balance into a set of force and moment readings, we calibrated the balance before our *in vivo* measurements using the method developed in [158]. This was achieved by loading it with a range of known masses (ball bearings) at known distances and positions relative to the balance origin, using a custom rig consisting of a T-bar containing seven evenly spaced neodymium magnets. We recorded the balance output with ball bearings at each magnet position, with the bar in both horizontal and vertical orientations, and at eight different orientations (every 45°) relative to the force balance. Before each mass was loaded onto the arm, we took an unloaded measurement to provide zero measure to account for any balance drift over the course of the recording. A shunt calibration was also applied at the beginning and end of each measurement series to control for any changes in the electrical properties of the measurement circuit. Given the high sensitivity of the force transducers to stimuli other than force, we carried out calibration recordings with the same 20 lux lighting and 29°C conditions as used during the *in vivo* experiments. We fitted a linear calibration matrix by regressing the recorded voltage outputs on the known forces and moments, and inverting. The plots in Figure 63 use the calibration matrix to demonstrate the linear response of the balance relative to our known input forces and moments.

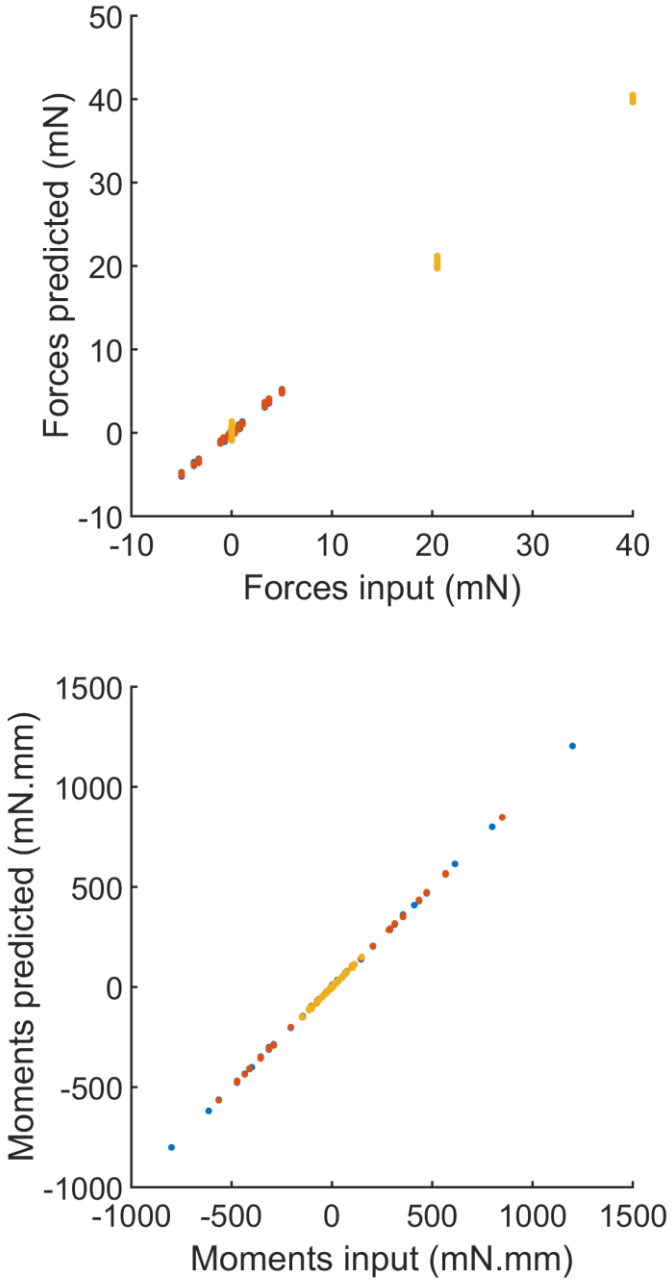


Figure 63: x-axis: known input forces (top) and moments (bottom) applied to the balance. y-axis: predicted forces and moments calculated using the calibration matrix and recorded voltages. Blue, red, and yellow represent the X, Y, Z forces and L, M, N moments respectively.

The inertial effects of dynamic movements on the balance were also characterised by recording the voltages without a locust tethered. These were found to be small relative to the forces and moments generated by the locusts, but were nevertheless cross-correlated with the tethered flight data and accounted for (removed).

Centre of mass measurements

Forces and moments were resolved at the centre of mass of each locust, estimated using the average positions of this point made by Taylor & Thomas [121]. We assumed the *y*-axis was perfectly aligned with the centre of mass, while *x*- and *z*-axis offsets were calculated using lateral view photographs of each locust attached to the mount.

Moments of inertia

Calculating dynamic stability (Chapter 7) requires the locust's moments of inertia. The moments of inertia of the locust body were approximated using the BoneJ plug-in [159] for image processing software ImageJ (ver. 1.49, NIH, USA). A set of 2D slices defining the contours of a body (created from the 3D model used in [130]) (Figure 64) was used as the input, assuming constant density of 0.5 $g.cm^{-3}$ (determined based on the average mass of the four locusts).

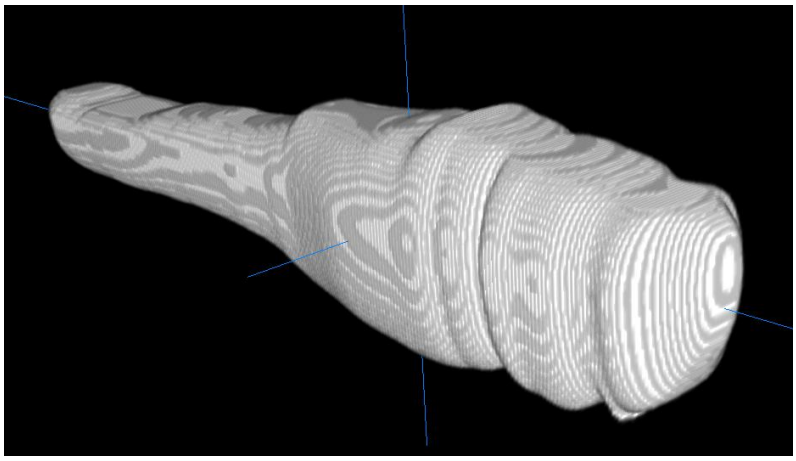


Figure 64: Stack of 2D slices defining the locust body, used in ImageJ with the BoneJ plug-in to calculate moments of inertia.

The wing moments of inertia were estimated by treating equivalent size wing sections as point masses along a thin rod connected to the centreline of the locust's body. Although the wing's contribution to the moment of inertia will vary through each wingbeat, we

approximated the contribution by solely calculating the moments of inertia with the long axis of the wing parallel to the transverse y-axis of the body [160]. The total wing mass was less than 4% of the body mass for each locust.

Variable	Symbol	Value (kg m^2 x 10^{-9})
roll moment of inertia	I_x	10.44
yaw moment of inertia	I_z	145.20
product of inertia between roll and yaw	I_{zx}	0.164

Table 4: The locust's inertia about the centre of mass.

6.3 Results

Having converted voltages to forces and moments, and resolved them at the locust's centre of mass, we seek to reveal the effects of covering the sensilla under static and sinusoidal sideslip changes. Figure 65 plots an example of the time-averaged *X, Y, Z* forces and *L, M, N* moments for one locust undergoing static changes in sideslip angle.

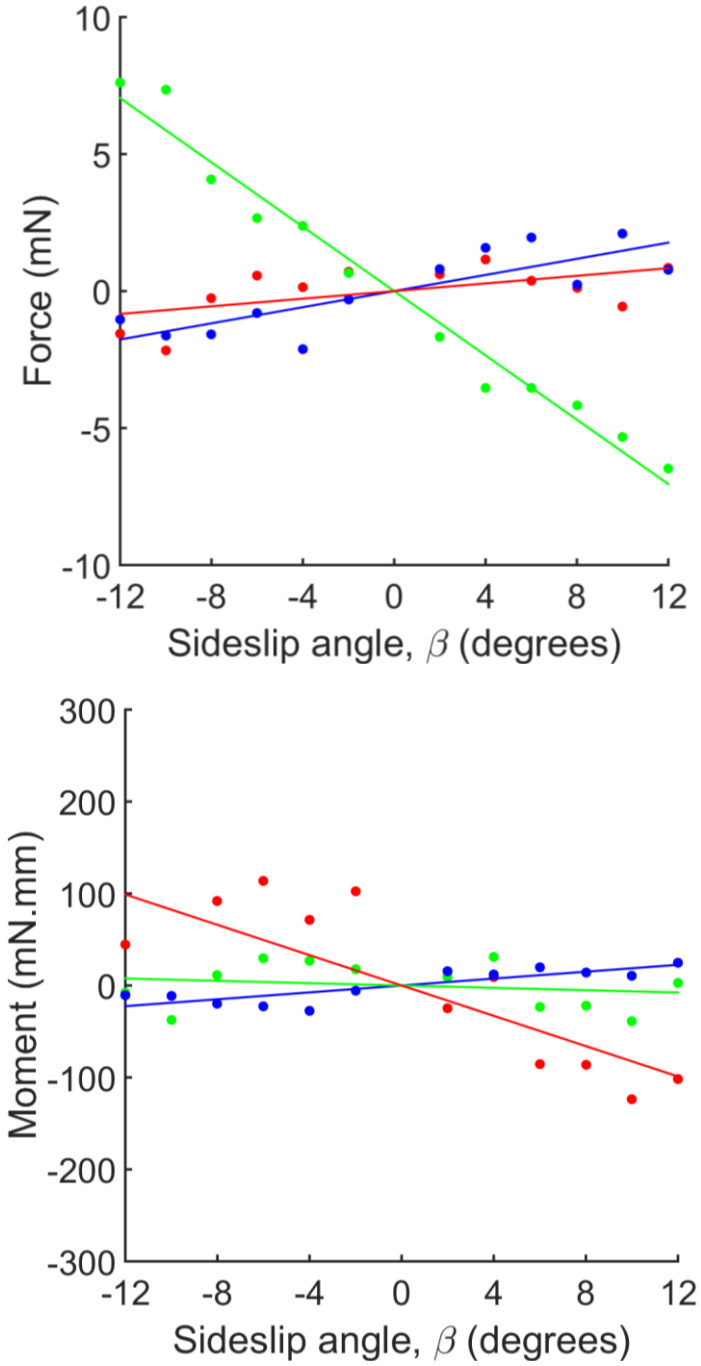


Figure 65: Example force (top) and moment (bottom) data from a single locust over the complete range of static sideslip angles. RGB colour scheme represents the X, Y, and Z forces, and L, M, and N moments respectively. Least squares lines are plotted for each dataset.

From the slopes of the least squares regression lines, it is clear forces and moments are varying as the locust is yawed through the range of sideslip angles. The most prominent

changes are seen in the Y (side) force and L (roll) moment, and could be caused by both passive and active effects.

β derivatives

We combined the forces and moments from all four locusts in separate General Linear Model (GLM) analyses for both static and dynamic cases using SPSS (ver. 22, IBM Corp, USA). For the static model, we used the mean force or moment measurements for each individual at each angle as individual data points. To examine the effect of covering the hairs when moving through sideslip angles, we focussed solely on the asymmetric effects related to generating sideslip forces – the side force (Y), roll moment (L), and yaw moment (N). The model had individual as a random effect, angle as a covariate, ablation as a fixed factor, and included the interaction between ablation and angle.

We defined four ablation stages: intact (beginning of experiment), part covered (some hair fields covered), all covered (all fields covered), and uncovered (covering removed). We originally intended to separately analyse coverings of pairs of fields as defined in our methods section, however, as we had only one sample for each combination, the decision was taken to pool these data into a single 'part covered' category. We include the part covering data for completeness, however, given its limitations, we draw the main points of comparison between the 'all covered' and 'uncovered' cases relative to the initial 'intact' cases.

Before carrying out the GLM for the dynamic data, the dynamic forces and moments were first low-pass filtered at 10 Hz using a 6^{th} order Butterworth filter to remove frequency content left at the wingbeat frequency (~20 Hz). The remaining data was then downsampled to 20 Hz. The sideslip angle, angular velocity, and angular acceleration were all included as predictors in the GLM. Harmonics were evident at 2x and 4x the stimulus frequency in the raw output (force and moment) data, however, none were apparent in the stimulus (recorded as the encoder output from the motor). Even harmonics can be produced by quadratic characteristics [161], and in this case are likely explained by the

quadratic dependence of force on velocity – pressure forces scale with speed squared. In order to account for the harmonics, sine and cosine stimuli at 2x and 4x the stimulus frequency were also included in our GLM. Incorporating them into the model removed autocorrelation in the residuals and increased R^2 values.

Figure 66 plots the derivatives of Y, L, and N with respect to the sideslip angle, β (denoted $C_{y\beta}$, $C_{l\beta}$, and $C_{n\beta}$ respectively), calculated in our static and dynamic data GLMs. Derivatives are given for each ablation stage for both the static and dynamic stimuli, as well as the data from a dead locust undergoing dynamic sideslip changes.

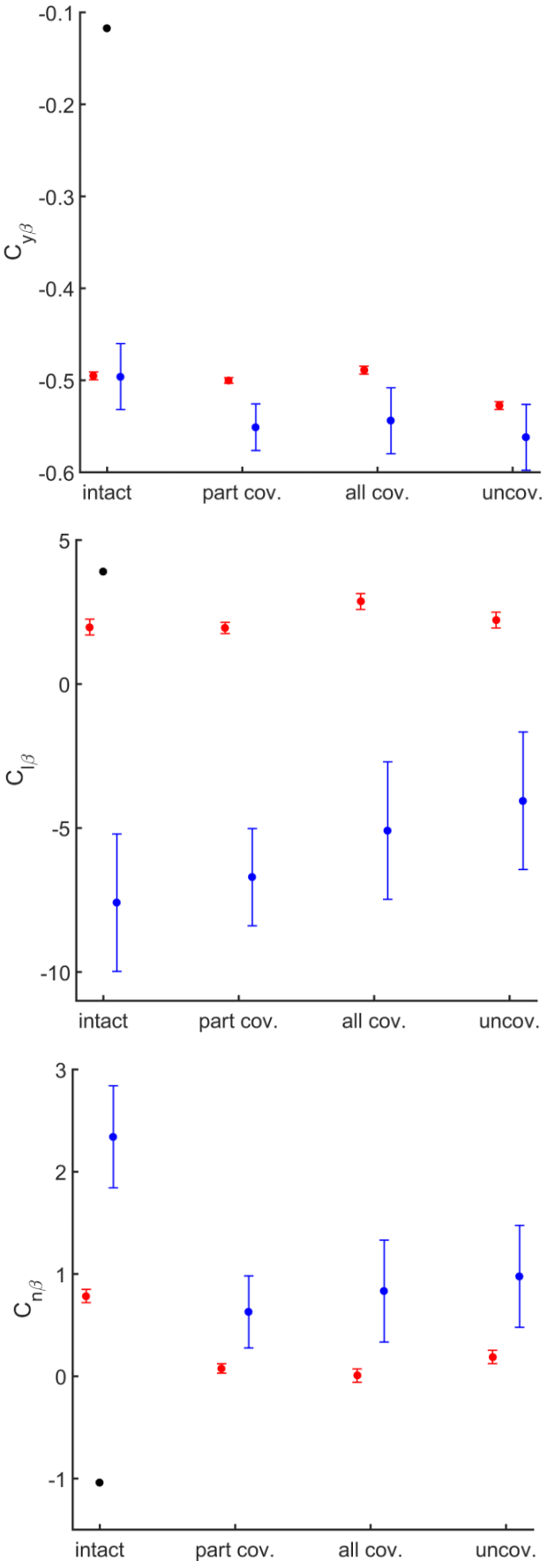

-0.1
-0.2
-0.3
-0.4
-0.5
-0.6
$C_{y\beta}$
intact
part cov.
all cov.
uncov.
5
0
-5
-10
$C_{l\beta}$
intact
part cov.
all cov.
uncov.
3
2
1
0
-1
$C_{n\beta}$
intact
part cov.
all cov.
uncov.

Figure 66: Derivatives of Y, L, and N with respect to the sideslip angle, β, at each ablation stage, for both the static (blue) and dynamic (red) stimuli, as well as the data from a dead locust (black) undergoing dynamic sideslip changes. 'intact' = no hairs covered (beginning of experiment), 'part covered' = some hair fields covered, 'all covered' = all fields covered, and 'uncovered' = covering removed. Error bars are 95% confidence intervals.

The side force (Y) derivative, $C_{y\beta}$

In the static case, the *Y*-force derivative, $C_{y\beta}$, was negative and significantly different from zero for all treatments (linear mixed model: $p<0.001$; $F_{1,220}=4429$). A negative value of $C_{y\beta}$ implies that a component of the aerodynamic force acts in the direction of the sideslip velocity vector, consistent with this being an aerodynamic drag force. The value of $C_{y\beta}$ varied significantly between treatments ($p=0.046$; $F_{3,220}=2.71$), which was wholly attributable to the difference between the intact treatment and the subsequent treatments post-manipulation (Figure 66). Even so, the difference between treatments was small, as the magnitude of $C_{y\beta}$ was only 10-13% greater in the treatments post-manipulation.

In the dynamic case, $C_{y\beta}$ was also negative and significantly different from zero for all treatments (linear mixed model: $p<0.001$; $F_{1,79969}=382173$), as well as varying significantly between treatments ($p<0.001$; $F_{3,79969}=65$). This latter result was predictable given the small size of the 95% confidence intervals for the dynamic data (Figure 66). These are caused by the large number of data points for each angle position and treatment combination. There is a danger that they underestimate the scale of error due to pseudo-replication. We attempted to account for this by averaging the forces on a wingbeat-by-wingbeat basis (i.e. we downsampled the data at 20 Hz), however, because angle varies continuously (in the range $-12° \leq \beta \leq 12°$) under dynamic conditions, the number of data points is still inherently high. With the dead locust, $C_{y\beta}$ was also negative and significantly different from zero (linear model: $p<0.001$; $F_{1,3989}=14766$).

The roll moment (L) derivative, $C_{l\beta}$

In the static case, the *L*-moment derivative, $C_{l\beta}$, was negative and significantly different from zero for all treatments (linear mixed model: $p<0.001$; $F_{1,220}=124$). However, $C_{l\beta}$ did not vary significantly between treatments ($p=0.138$; $F_{3,220}=1.85$) (Figure 66).

In contrast, under dynamic sideslip changes, $C_{l\beta}$ was positive and significantly different from zero for all treatments (linear mixed model: $p<0.001$; $F_{1,79969}=3556$), as well as varying significantly between treatments ($p<0.001$; $F_{3,79969}=4.72$). With the dead locust, $C_{l\beta}$ was also positive and significantly different from zero (linear model: $p<0.001$; $F_{1,3989}=3925$) (Figure 66).

The yaw moment (N) derivative, $C_{n\beta}$

Under static changes, the *N*-moment derivative, $C_{n\beta}$, was positive and significantly different from zero for all treatments (linear mixed model: $p<0.001$; $F_{1,220}=92$). The value of $C_{n\beta}$ varied significantly between treatments ($p<0.001$; $F_{3,220}=10.79$), which was wholly attributable to the difference between the intact treatment and the subsequent treatments post-manipulation (Figure 66).

Similarly, in the dynamic case, $C_{n\beta}$ was positive and significantly different from zero for all treatments (linear mixed model: $p<0.001$; $F_{1,79969}=1471$). It also varied significantly between treatments ($p<0.001$; $F_{3,79969}=170$). In contrast, with the dead locust, $C_{n\beta}$ was negative and significantly different from zero (linear model: $p<0.001$; $F_{1,3989}=10959$).

6.4 Discussion

The side force (Y) derivative, $C_{y\beta}$

The *Y*-force derivative, $C_{y\beta}$, is signed negatively for static, dynamic, and dead dynamic cases, as is customarily found in rigid body aircraft [127]. With the dead locust, we expect the generated force to be almost entirely from drag on the body. We solved the drag equation

($F_D = \rho u^2 C_D A$, where ρ is the density of air, u is the flow velocity, C_D is the drag coefficient, and A is a reference surface area) in the case of the locust's entire lateral surface area being exposed to oncoming flow. The surface area was estimated from the lateral view presented in Figure 4 of Taylor and Thomas' paper on locust dynamic flight stability [121]. The resulting drag force value, 4.30 mN, is on the same order of magnitude as our maximum measured *Y*-force with the dead locust, 2.62 mN. We expect the value from the drag equation to be larger as the range of sideslip angles we used experimentally would not expose as much of lateral surface area as used in our approximation. Therefore, it does appear that the majority of the dead locust's *Y*-force can be explained by drag. In the case of live locusts, $C_{y\beta}$ is significantly larger, likely effected by the beating wings. The wings could generate changes in *Y*-force both passively through drag, and actively, by flapping asymmetrically. If locusts were actively flapping to produce a *Y*-force in opposition to the oncoming airflow when $\beta \neq 0$, $C_{y\beta}$ would be positive (if this force exceeded drag). Therefore, the increased negative slope relative to the dead locust must be caused by drag force and possibly asymmetric flapping in the direction of airflow travel (away from the airflow source).

In the static case, differences in $C_{y\beta}$ were weakly significant across treatments, attributable to the differences between the 'intact' treatment and the three subsequent treatments. Therefore, covering up the sensilla did affect the *Y*-force generated when moving the locusts through the range of sideslip angles. As the slope becomes steeper following covering of the hairs, it suggests that locusts were actively producing some *Y*-force in a direction that opposed drag force when the hairs were intact. In the dynamic case, there were also significant differences across treatment, however, the danger that the 95% confidence intervals may underestimate the scale of error leads us to refrain from drawing firm conclusions when comparing between treatments.

The roll moment (L) derivative, $C_{l\beta}$

The roll derivative, $C_{l\beta}$, shows distinct contrast between the static and dynamic cases, with opposing signs, while the dead locust exhibited a positive slope. In reference to our axis

system, a positive slope indicates the point of action of the force is dorsal relative to the centre of mass, while a negative slope indicates it acts ventrally. Once again, the dead locust is capable of generating only passive effects and the positive slope is expected if the roll moment is solely caused by drag with the point of action dorsal to the centre of mass. The static case illustrates a negative change in roll moment under increasing sideslip angle, suggesting some active control by the locust. Dorsal video recordings demonstrated that, under static changes, locusts curved their abdomens and moved the position of their hind legs (Figure 67) when $\beta \neq 0$, thus shifting their weight distribution and most likely compensating for the offset, in a similar manner to hang gliders. These responses were slow - often easily observable over a few seconds. The movements may be coupled with an equally slow response in the flapping wings to further augment roll moment. Camhi [31] has previously documented the abdomen and leg responses in locusts, concluding they were majority controlled by the trichoid sensilla. We still see some response after the sensilla are covered, however, there is a general decline in the size of the response after each ablation treatment (although the changes were not statistically significant). The changes in abdomen and leg positions were either minor or not evident in the dynamic case, even at the lowest frequencies. Indeed, the hind legs were often in the tucked state for the entire duration of recordings (e.g. Figure 67). We suspect the dynamic angle changes were too fast to allow these postural changes, and consequently we recorded a positive slope. This was likely caused largely by passive changes in roll moment resulting from drag on the body and wings, acting dorsally to the centre of mass in the same manner as in the dead locust case.

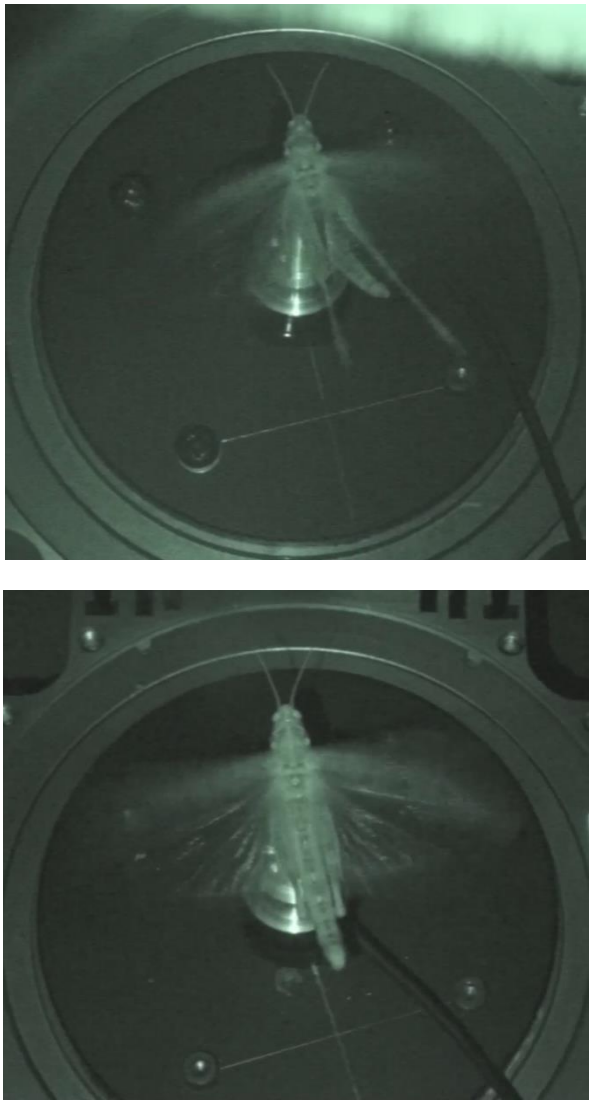


Figure 67: Dorsal view of tethered locusts during static (top) and dynamic (bottom) sideslip changes. Both views show the locusts undergoing positive sideslip. Note, in the static case, the curving of the abdomen and shifting of leg position (and possibly asymmetric wing kinematics). In the dynamic case, the legs are tucked and the abdomen largely parallel with the rest of the body, with only a very slight camber.

The yaw moment (N) derivative, $C_{n\beta}$

The static and dynamic yaw derivatives, $C_{n\beta}$, are all positive, while in the case of dead locust, the value is negative. The positive sign indicates that the point of action of the force acts anterior (i.e. towards the locust head) to the centre of mass while the negative sign indicates it acts posteriorly. In reference to our axis system, the positive sign indicates that the live locusts oppose changes in sideslip (the moment is stabilising), and this could manifest itself

in both passive and active effects. This yaw stiffness, i.e. weathercock stability, is largely caused passively by the body and vertical tail in rigid aircraft [127]. In insects (and birds), the wings bestow a similar response, termed 'flapping counter torque' (FCT) [162]. FCT arises from wing velocity asymmetries, leading to force asymmetries, between symmetrically flapping wings on each side of an animal when it undergoes rotations (with maximum effect when rotating about an axis normal to the stroke plane). These forces act counter to the direction of body rotation and therefore have a damping effect [162]. As locusts have a stroke plane angle approximately 45° relative to the axis of yaw rotation, flapping counter torque may not solely affect the yaw moment, but it is reasonable to assume there is some yaw damping.

Active asymmetric flapping also likely generates yaw moment. We find evidence for an active response when comparing the 'intact' treatment relative to all others: $C_{n\beta}$ values are significantly higher for the 'intact' treatment in both static and dynamic cases. The larger $C_{n\beta}$ of static relative to dynamic stimuli likely indicates the slow response of locusts in changing wing kinematics. As the dead locust is not flapping, and has its wings tucked against the body, we do not see any of these effects. The negative sign of the $C_{n\beta}$ indicates the moment is destabilising for the dead locust.

Both the static and dynamic $C_{n\beta}$ values were significantly different overall between all ablation treatments. It is very clear from Figure 66 that there are large differences between the initial 'intact' treatment and all three subsequent treatments. This appears to demonstrate the role of the trichoid sensilla in controlling yaw moment. Interestingly, the initial 'intact' treatment derivatives appear to be significantly different to the final, 'uncovered' treatment (latex removed). Therefore, although we observed no apparent morphological change to the sensilla after removing the latex, the sensory response was likely affected by the application. The other possibility is a temporally correlated decline in $C_{n\beta}$ over the course of the experiment. However, the similarity in $C_{n\beta}$ over the three latter ablation treatments suggests this is not the case. Indeed, $C_{n\beta}$ slightly increased between the

'part covered' and 'all covered' treatments, and between the 'all covered' and 'uncovered' treatments for both the static and dynamic cases.

6.5 Conclusion

Our *in vivo* sensor manipulation experiments have demonstrated clear evidence of the trichoid sensilla providing feedback on changes in sideslip. We identified the response of locusts to sideslip (β) in their generation of Y-force and L- and N-moments. After removing sensory input to the trichoid sensilla, Y-force and N-moment derivatives were significantly increased and decreased respectively. Both these results suggest the locusts were actively using feedback from the trichoid sensilla to counter the changes in sideslip. In the case of the L-moment, we identified the slow response of shifting abdomen and hind leg position as the likely reason for distinct differences in L between static and dynamic sideslip changes. These results are in agreement with Weis-Fogh's [24] and Gewecke and Philippen's [30] findings that the hairs are involved in yaw stabilisation in asymmetric airflows. We have provided a quantitative basis to support these earlier experiments and have revealed the particular axes about which these responses occur. It was also the case that removing the latex covering was insufficient to return these forces and moments to the initial 'intact' treatment levels (at least, over the timescale of these experiments). In the next chapter, we extend our analysis of the force and moment recordings to reveal the locusts' natural modes of motion.

Chapter 7

Dynamic stability analysis

7.1 Introduction

In this chapter, we utilise the same *in vivo* force and moment data detailed in Chapter 6 to examine the dynamic lateral flight stability of the locusts. The flight dynamics relate the forces and moments the insects generate to the kinematics these would produce in free-flight. Analysing dynamic flight stability is a crucial part of the study of flight control, describing the behaviour of a flying body following disturbance from equilibrium flight. It reveals the dynamic properties of the system such as which degrees of freedom are unstable and how quickly the instabilities develop [163]. An unstable system is characterised by ever-increasing magnitude in a disturbance away from the equilibrium condition, while in a stable system the disturbance will decay over time. Stability is typically expressed in terms of the damping and timescales of the modes of motion generated by disturbances.

Flight dynamics modelling has been widely applied in the study of insects, including the bumblebee [133, 164], fruit fly [165], hawk moth [166-168], and locust [121, 169, 170]. Our experiment develops the work of Taylor & Thomas [121], which provided the first formal

quantitative analysis of dynamic longitudinal flight stability in the desert locust (and at the time, of any flying animal). Our setup differs in that it measures the lateral forces generated following instantaneous changes in sideslip (as opposed to longitudinal forces in response to angle of attack), as well as including manipulation of the trichoid sensilla. Recent work has also investigated the effect of sideslip angle on forces and wing kinematics in locusts [171], but over a narrower range of angles and without sensor manipulation or analysis of dynamic stability. Many of the studies listed above rely on computational fluid dynamics to compute the necessary aerodynamic derivatives. Here, we follow the techniques of Taylor & Thomas [121] by calculating these derivatives using *in vivo* measurements.

7.2 Methods

Our framework for analysing insect flight stability is based upon a set of linearised equations of rigid body motion widely used in aircraft dynamics (see e.g. [127]), which are applied under what is known as the small-disturbance theory. This framework approximates the insect as a rigid body and consequently has three key assumptions: (i) the insect has only six degrees of freedom – three in rotation and three in translation. Thus, we neglect any postural or elastic degrees of freedom relating to the body and wings. During flapping flight, the position of the centre of mass will also shift, however, under this approximation, forces and moments are resolved at an assumed constant point. (ii) We assume the wingbeat frequency is sufficiently fast so as to not excite the natural oscillatory modes of the system [172], hence the effects of the flapping wings are wingbeat cycle averaged. (iii) The motion of the flying body consists of small disturbances from the reference condition of steady flight. This assumption has been found in practice to yield good results for aircraft, partly because the major aerodynamic effects are approximately linear functions of the disturbances [127]. The linearisation has the convenient property of decoupling longitudinal and lateral stability. Here we are solely interested in the lateral stability, which has two further assumptions: absence of gyroscopic effects, and neglect of all aerodynamic cross-coupling [127].

The complete time-dependent linearised equations can be expressed as:

$$\dot{x}(t) = Ax(t) + Bu(t) \qquad (1)$$

Where the system matrix, *A*, describes changes in the forces *X, Y, Z* and moments *L, M, N* as a function of the state variables $x(t) = [u, v, w, p, q, r, \varphi, \theta, \psi]^T$. These variables are the forward, sideways, and vertical velocities, the roll, pitch, and yaw rates, and the roll, pitch, and yaw angles respectively. The control matrix, *B*, and the control input vector, *u(t)*, describe the active control of the flight dynamics. As *A* and *B* contain only real constant numbers, Equation 1 is linear time-invariant with respect to the small disturbances about the equilibrium condition on which the equations are linearised [121].

It is customary in the study of aircraft control to reserve *A* for passive aerodynamic effects, with pilot and automatic control placed in *B*. However, in the case of insects we are unable to isolate the passive aerodynamic stability of the locust without destroying the control inputs necessary for stimulating normal forward flight. Therefore, we must use the approach of viewing automatic control as augmenting the stability derivatives in *A* [121, 127]. Under this regime, the lateral stability derivatives combine passive aerodynamic effects with the aerodynamic effects stemming from automatic changes in muscle firing caused by changes in body angle [121].

As we are not evaluating a control model, we drop the *B* term, retaining solely the intrinsic dynamics of the uncontrolled system (Equation 2), known as the natural or free dynamics:

$$\dot{x}(t) = Ax(t) \qquad (2)$$

The complete system matrix, *A*, for the lateral case is given in Equation 3:

$$A = \begin{bmatrix} \frac{Y_v}{m} & \frac{Y_p}{m} & \left(\frac{Y_r}{m} - u_0\right) & g\cos\theta_0 \\ \left(\frac{L_v}{I'_x} + I'_{zx}N_v\right) & \left(\frac{L_p}{I'_x} + I'_{zx}N_p\right) & \left(\frac{L_r}{I'_x} + I'_{zx}N_r\right) & 0 \\ \left(I'_{zx}L_v + \frac{N_v}{I'_z}\right) & \left(I'_{zx}L_p + \frac{N_p}{I'_z}\right) & \left(I'_{zx}L_r + \frac{N_r}{I'_z}\right) & 0 \\ 0 & 1 & \tan\theta_0 & 0 \end{bmatrix} \qquad (3)$$

$$I'_x = (I_x I_z - I_{zx}^2)/I_z$$

$$I'_z = (I_x I_z - I_{zx}^2)/I_x$$

$$I'_{zx} = I_{zx}/(I_x I_z - I_{xz}^2)$$

Where m denotes the reference body mass, Ix and Iz the moments of inertia about x and z respectively, and Izx the product of inertia about these two axes. A contains the partial derivatives of Y, L, and N with respect to the lateral state variables v, p, and r. The state vector, $x(t)$, for the lateral case, contains only the variables $[v, p, r, \varphi]$ (sideways velocity, roll rate, yaw rate, and roll angle).

We can calculate the stability derivatives in A using the force and moment data from Chapter 6. The broken-loop conditions of our experimental setup were necessary to ensure that changes in stroke cycle do not affect the external stimuli that the locusts receive [121]. Hence, we make the assumption that the locusts respond similarly to perturbations from equilibrium under broken-loop tethered flight as they would during closed-loop free flight. Although there remains debate about the value of this experimental design, we argue it is preferable to vary only one degree of freedom at a time, as opposed to Weis-Fogh's [124] suggestion that the insect be allowed to control other variables such as tunnel wind speed. While the latter may logically produce more natural flying conditions, it remains highly artificial if body angle cannot also vary freely [121]. The axis of rotation is also likely to not be aligned with the centre of mass, which itself will change through wingbeat anyway. Therefore, we believe our single broken-loop study is more informative than a hybrid case where some control loops are closed whilst leaving others open [121].

7.3 Results

In this section, we use our recorded force and moment data to examine the modes of motion of the locusts under sideslip changes. It is necessary to use the dynamic (not static) data because we require angular velocity force and moment derivatives. The key comparison for our analysis is between the initial 'intact' hair treatment and the 'all covered' case, as we are

particularly interested in seeing the effect of feedback from the trichoid sensilla on the stability and modes of motion.

Finding the natural modes of motion

The clearly linear trends demonstrated in Figure 65 support the linearisation of the measured forces and moments as (linear) functions of sideslip angle in the stability equations.

As stated above, the equation for the natural dynamics of the uncontrolled system is:

$$\dot{x}(t) = Ax(t) \qquad (4)$$

Solutions to this equation are of the form:

$$x(t) = e^{At}x(0) \qquad (5)$$

Where e^A is the matrix exponential of A, and $x(0)$ are the initial conditions at $t = 0$. If A can be diagonalised, this equation can be re-written as:

$$x(t) = Ve^{Dt}V^{-1}x(0) \qquad (6)$$

Where D is a diagonal matrix containing the eigenvalues of A, and V is a matrix whose columns are the right eigenvectors of A. It therefore follows that the eigenvalues and eigenvectors of A are sufficient to fully characterise the natural dynamics of the system [127, 158, 160].

Eigenvalues can be either real or complex numbers, and their values indicate the stability of the system. A positive real value signifies an unstable monotonic mode, indicating an exponentially growing amplitude of motion away from equilibrium. In contrast, a negative real value signifies a stable subsidence mode in which there is exponential decay in motion back to equilibrium. In the case of complex numbers, the imaginary part represents the angular frequency of an oscillatory motion, while the sign of the real part determines

whether the motion is unstable (positive) or stable (negative). Once again, the system is unstable if any of the eigenvalues have a real positive part. Each eigenvalue is associated with an eigenvector describing the phase and magnitude of the motion, and together each pair of values describes a natural mode of motion of the body. The modes linearly combine to describe the motion of a flying body following any deviation from equilibrium flight.

Using our mass, force, moment, and moment of inertia measures, A can be populated. As the roll rate, p, was not altered, the stability derivatives with respect p (second column) are all equal to zero. The stability derivatives with respect to sideslip velocity were readily calculated by regressing the Y, L, and N measurements on sideslip velocity, v, and yaw rate, r. The derivatives with respect to sideslip velocity are slightly different to the β derivatives presented in Chapter 6 ($C_{y\beta}$, $C_{l\beta}$, $C_{n\beta}$). They are simply calculated trigonometrically by multiplying by the airspeed, U, to convert to sideslip velocity (e.g. $Y_v = U \cdot C_{y\beta}$).

System matrices (A) were produced for each individual locust using dynamic angle and angular velocity derivatives for the 'intact' and 'all covered' hair treatments. These were then averaged across individuals, producing two system matrices for analysis (one for the 'intact' treatment and the other for the 'all covered' treatment). An example A is given below:

$$A = \begin{bmatrix} -4.11 & 0 & -0.09 & 9.81 \\ 2450 & 0 & 1700 & 0 \\ 97.08 & 0 & 18.63 & 0 \\ 0 & 1 & 0 & 0 \end{bmatrix}$$

We computed the eigenvalues and eigenvectors of each matrix using the *eig* function in MATLAB. In the following discussion, we first analyse these values for the 'all covered' treatment. We follow with the 'intact' treatment, allowing us to see the role of sensilla feedback on the dynamic stability of the locusts.

All sensilla covered

The eigenvalues and eigenvectors of the 'all covered' system matrix describe three modes of motion: a fast, unstable monotonic mode, a fast, stable oscillatory mode, and a slow, stable monotonic mode (Table 5 and Table 6).

	fast, unstable monotonic	fast, stable oscillatory	slow, stable monotonic
Eigenvalue	35.08	-18.19 ± 30.63i	-1.63
Time to half/double (wingbeats)	0.40	0.76	8.52
Time to half/double (s)	0.02	0.04	0.43
Frequency (Hz)	-	4.88	-

Table 5: Eigenvalues characterising the lateral modes of motion calculated using the system matrix of locusts with all trichoid sensilla covered. Times to half/double refer to the time (in wingbeats or seconds) for the mode to half (stable mode) or double (unstable) in magnitude.

	fast, unstable monotonic		fast, stable oscillatory		slow, stable monotonic	
	magnitude	phase (°)	magnitude	phase (°)	magnitude	phase (°)
δv	0.25	0	0.29	245	4.03	0
δp	35.08	0	35.62	120	1.63	180
δr	0.07	0	0.07	123	12.77	180
$\delta \varphi$	1	0	1	360	1	0

Table 6: Eigenvectors illustrating the magnitude and phase (given in polar form) of the disturbance variables δv, δp, δr, and δφ for each mode of motion.

The modal structure of one unstable monotonic mode, one stable monotonic mode, and one stable oscillatory mode has been identified in several other models of lateral flight stability in flying insects (e.g. [158, 164, 173]).

The unstable monotonic mode would have to be actively stabilised by the insect through feedback control to achieve a fully stable system. The mode is predominantly unstable in roll rate and to a lesser degree in sideways velocity. There is a very small effect of yaw rate, but it likely plays no significant role.

The two stable modes do not require stabilisation through feedback control. However, they are important as their damping characteristics indicate axes that would be more energetically costly to move about than others [158]. The fast, oscillatory mode is a highly damped oscillation – halving in three-quarters of a wingbeat. The rapid speed of the oscillation means the mode will effectively have the character of a monotonic mode. This mode is largely damped in roll rate, and to a lesser degree in sideways velocity. The stable monotonic mode is much more lightly damped - halving in 8.52 wingbeats. It contrasts with the oscillatory mode as it is predominantly damped in yaw rate (and to lesser extents in sideways velocity and roll rate). It therefore has the character of a stable spiral mode [127].

All sensilla intact

	fast, unstable monotonic	slow, stable oscillatory	fast, stable monotonic
Eigenvalue	43.30	-1.93 ± 32.84i	-24.93
Time to half/double (wingbeats)	0.32	7.19	0.56
Time to half/double (s)	0.02	0.36	0.03
Frequency (Hz)	-	5.23	-

Table 7: Eigenvalues characterising the lateral modes of motion calculated using the system matrix of locusts with all trichoid sensilla intact. Times to half/double refer to the time (in wingbeats or seconds) for the mode to half (stable mode) or double (unstable) in magnitude.

	fast, unstable monotonic		slow, stable oscillatory		fast, stable monotonic	
	magnitude	phase (°)	magnitude	phase (°)	magnitude	phase (°)
δv	0.21	0	0.30	274	0.47	180
δp	43.30	0	32.90	93	24.93	180
δr	0.81	0	0.75	152	1.04	0
$\delta \varphi$	1	0	1	0	1	0

Table 8: Eigenvectors illustrating the magnitude and phase of the disturbance variables δv, δp, δr, and δφ for each mode of motion.

When the trichoid sensilla are intact, the system matrix predicts the existence of three lateral modes of motion (Table 7 and Table 8): a fast, unstable monotonic mode, a slow, stable, oscillatory mode, and a fast, stable monotonic mode.

The modal structure of two stable modes and one unstable is the same as the 'all covered' case, however, the stable monotonic mode is now fast and the oscillatory mode is slow. The speed of the stable, monotonic mode indicates it is now highly damped relative to the 'all covered' case. As the trichoid sensilla are likely being used for sensing sideslip (using the fields F1 and F2 in particular, as we have argued in previous chapters), it seems their active feedback enhances the inherent passive weathercock stability. As a result, the fast, stable mode is largely not affecting yaw rate (in contrast to the 'all covered' case), but instead now has a strong roll rate component.

The oscillatory mode has shifted from fast to slow, and now has an order of magnitude larger component of yaw rate than the 'all covered' case. The mode now more closely resembles a Dutch roll, one of the basic dynamic modes of aircraft. Dutch roll can arise as a result of static weathercock stability (i.e. yaw damping) [174]. As we believe feedback from the trichoid sensilla does indeed provide increased yaw damping, this seems the likely explanation for the nature of the oscillation.

The unstable mode also has an order of magnitude larger component in yaw rate, but is still principally a roll rate instability. The large roll component would create a motion similar to a roll divergence mode, although the in-phase yaw term may also give it some characteristics of an unsteady spiral mode [127]. The divergence speed of the mode is very fast – doubling in magnitude over 0.32 wingbeats (0.02 s). This seems a short time for the insect to observe the excitation and to counteract accordingly. However, the locust would need to control this mode to produce a stable system.

Figure 68 illustrates the eigenvalues for both 'all covered' and 'intact' system matrices in Argand diagram form. These provide a visual comparison of the modes of motion between the two treatments.

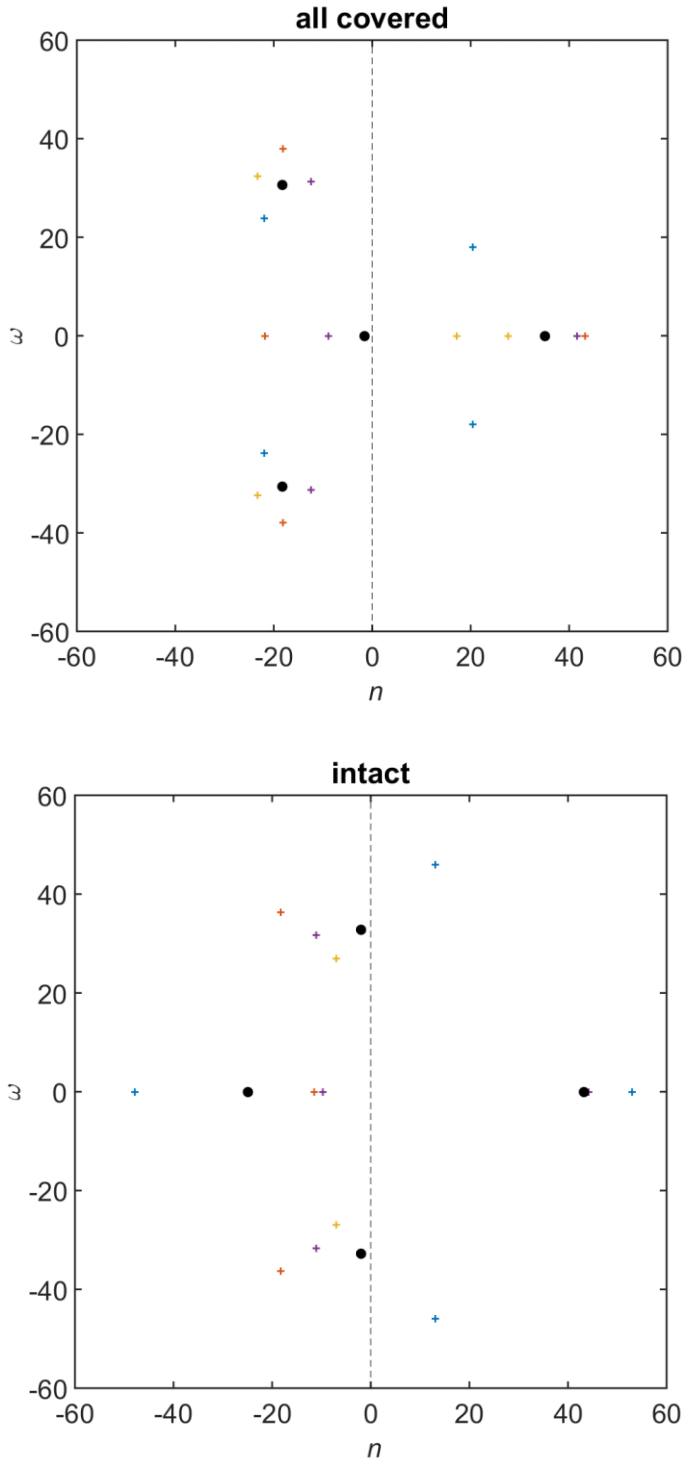


Figure 68: Argand diagrams of individual and average system matrices (A) for all covered (top) and intact (bottom) treatments. The x-axis is the real part of the root (eigenvalue), while the y-axis is the imaginary part. Crosses denote the values for individual locusts, while closed circles are from the average system matrices.

Simulating sensory feedback

In this section, we continue using the Argand diagram form to produce root locus plots. We use these to demonstrate the effects of changing stability derivatives on the modes of motion. By incrementally varying the stability derivatives in A, we can simulate changes in the response of the locusts (and thus simulate sensory feedback). Our focus is on N_v and the stability derivatives needed to fully stabilise the system of the 'intact' sensilla locusts.

N_v (yaw moment with respect to sideways velocity)

As we have described, we propose the difference between the modes of the 'all covered' and 'intact' treatments is predominantly caused by feedback from the sensilla affecting yaw moment in the latter case. We should be able to demonstrate this effect by manually changing the yaw rate derivative, N_v, in the system matrix of the 'all covered' case, to bring the modal structure closer to that of the 'intact' sensilla case. The root locus plot, Figure 69, reveals this is indeed possible. By manually increasing the yaw rate derivative to the same level as the 'intact' treatment, we can see the modes become more stable or unstable in the direction of the 'intact' sensilla modes.

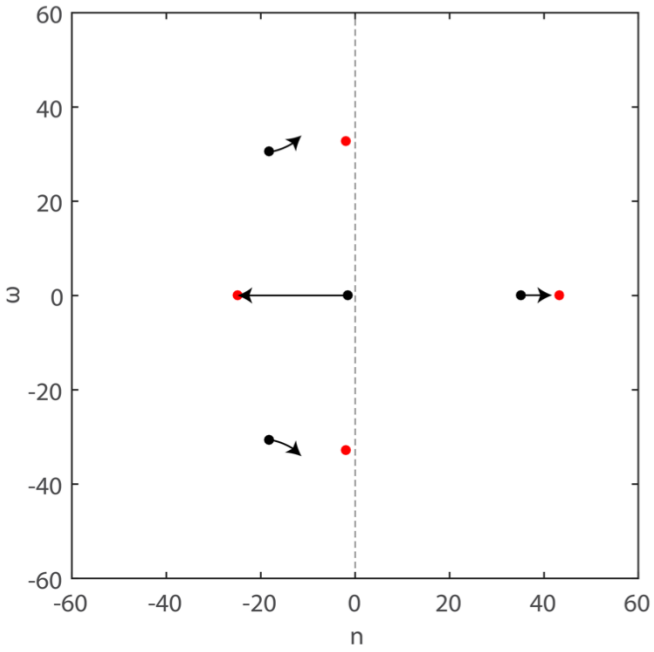


Figure 69: Root locus plot showing the effect of manually increasing the yaw rate derivative, N_v, (simulating feedback from the trichoid sensilla) for the 'all covered' treatment system matrix. The black points show the original modes produced from the unaltered system matrix. The red points are the modes from the 'intact' treatment system matrix. The arrows indicate the direction of movement of each black point as N_v is increased.

Stabilising the system

In order to demonstrate a fully stable system in the 'intact' case, the unstable mode needs to stabilised through active control by the locust. Table 8 reveals the mode is principally unstable in roll rate. Therefore, we initially surmised that all that is needed is to provide feedback on roll angle. However, we were not able to stabilise the system by solely adding in non-zero L_Φ or L_p terms (roll moment with respect to roll angle and rate, respectively), indicating the picture must be more complicated. We know that lateral motions are controlled by roll moment, yaw moment, or some combination of the two. Thus, it is likely there is yaw component that must also be accounted for.

In order to reveal the relative contributions of roll and yaw, we examined the controllability properties of the system by applying a modal decomposition (as used in [158, 175]). This

requires us first to define a control matrix, B, where we assume the only control inputs are a roll moment and a yaw moment:

$$B = \begin{bmatrix} 0 & 0 \\ \frac{I_z}{(I_x I_z - I_{xz}^2)} & \frac{I_{xz}}{(I_x I_z - I_{xz}^2)} \\ \frac{I_{xz}}{(I_x I_z - I_{xz}^2)} & \frac{I_x}{(I_x I_z - I_{xz}^2)} \\ 0 & 0 \end{bmatrix} = \begin{bmatrix} 0 & 0 \\ 9.58e^{07} & 1.08e^{05} \\ 1.08e^{05} & 6.89e^{06} \\ 0 & 0 \end{bmatrix}$$

Using A and B, we make a similarity transformation to modal canonical form:

$$A = \begin{bmatrix} 43.30 & 0 & 0 & 0 \\ 0 & -1.93 & 32.84 & 0 \\ 0 & -32.84 & -1.93 & 0 \\ 0 & 0 & 0 & -24.93 \end{bmatrix}$$

$$B = \begin{bmatrix} -2.33e^{06} & -1.06e^{07} \\ -4.73e^{06} & 7.58e^{05} \\ 2.41e^{06} & -1.72e^{07} \\ -3.80e^{06} & 1.11e^{07} \end{bmatrix}$$

After the transformation, A is a block-diagonal matrix of the eigenvalues of the system (see Table 7 for comparison). The rows of B relate to the four modes of motion of the system (two of which form a conjugate pair to produce the oscillatory mode), while the columns represent the two moments – roll and yaw. The values describe how each moment about their given axis injects energy into the modes of motion. The relative values of roll and yaw represent the relative proportion of both moments that would introduce the maximum energy into a given mode. As it is the first mode which is unstable, we look solely at the first row of B and see that the ratio of yaw moment to roll moment is 4.55 (-1.06e^{07} / -2.33e^{06}). By using this ratio, we can manually change stability derivatives concerning roll and yaw moments with respect to roll angle/rate with the maximum effect. As the mode is principally unstable in roll, we included a negative L_Φ term and a N_Φ term at 4.55x the value of L_Φ in the system matrix. Examining the eigenvectors of the system, the ratio of roll rate to roll angle is 43.30 (Table 8). Therefore, we included an L_p term, at 1/43.30 the value of L_Φ, and N_p at 4.55x L_p (maintaining the same ratio of yaw to roll moments).

Gradually increasing these values proved sufficient to stabilise the system (Figure 70). The plot shows changes in the modes up to the critical point of the whole system stabilising (in this case, when the oscillatory mode, which initially became unstable, restabilised). Thus, if the locust were to have additional feedback from sensors measuring roll angle and roll rate, the system could be stabilised.

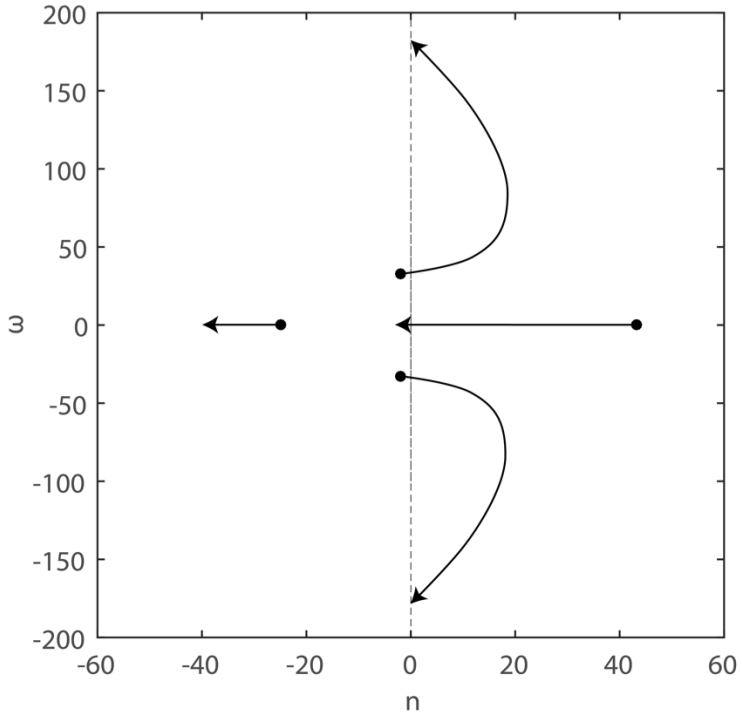


Figure 70: Stabilising the system. Black points are the eigenvalues produced from the 'intact' treatment system matrix. By including non-zero L_φ, N_φ, L_p, and N_p terms, we were able to stabilise the system (all values become concurrently negative).

In vivo, information on roll angle and roll rate is most likely fed back to the control system by the locusts' visual systems – the compound eyes and three ocelli. The role of the visual systems are well documented in insects for detecting and being used to control changes in attitude of the head/body during flight (see review in [10]). A common response is in adjusting orientation to remain parallel with the ground, using the dorsal overhead sun/sky as a point of reference, known as the dorsal light reaction. Goodman [176] demonstrated that desert locusts do indeed exhibit a dorsal light reaction in their roll axis, mediated by both the compound eyes and ocelli. When he presented locusts with complete darkness,

they continually rotated about the roll axis in their freely rotating mounts (they were unable to stabilise). Our experimental setup included overhead lighting that could potentially be used by the visual system to elicit the dorsal light reaction. However, our analysis demonstrated clear roll instability. It may be that an additional stimulus in the form of an artificial horizon was necessary, as Goodman also found a strong roll stabilising response when a mock horizon was presented to the locusts [176]. This would make sense given the location of the locust ocelli; while many insect species have dorsal ocelli, all three of the desert locust's ocelli are on the anterior surface on the head, pointing forwards. As a result, they may be optimally located for sensing the horizon as opposed to overhead light. Thus, we postulate there was insufficient stimulus from the dim overhead light to provide feedback on roll angle or rate in our experimental setup.

7.4 Conclusion

Analysis of the lateral dynamic stability revealed three natural modes of motion in locusts in both the 'intact' and 'all covered' hair cases: two stable and one unstable. We once again demonstrated the role of the sensilla in controlling yaw by manually adjusting N_v to bring the modes of the 'all covered' case closer to the 'intact' case. This artificial change was key in confirming our inferences about the nature of the modes of motion generated from our force and moment data. We were also able to stabilise the complete system by augmenting L and N derivatives with respect to roll angle and roll rate.

We have therefore revealed how behavioural and kinematic changes by the locusts relate to their natural flight dynamics. Further work would logically focus on longitudinal dynamics under similar conditions (i.e. the same manipulation experiments and force measurements, but under varying angle of attack). Our experimental setup also imposed the limitation of having no roll rate terms measured. We have demonstrated (artificially) in our system that non-zero roll rate terms were key components in stabilising the system. Thus, an informative extension to our experimental setup would be to allow variation in roll and capture the dynamics of the system under these extended conditions. We suggest a

rotatable artificial horizon would prove a useful addition to enable visually perceived variations in roll rate for the locust, as well as potentially providing the necessary visual stimulus to stabilise about the roll axis.

Chapter 8

Summary and outlook

In the Introduction, we posed three questions to explore over the course of this thesis:

What aerodynamic features of the flow could the cephalic hair sensilla be measuring?

How have sensillum position & directional sensitivity been optimised to monitor features of airflow?

How is this sensory information used in flight control?

In Chapters 2 and 3 we addressed the first of these using a combination of experimental and simulated flow visualisation. Particle image velocimetry revealed the gross flow features around a scale model of the desert locust head, enabling identification of stagnation and flow separation points, as well as the airflow over each of the five fields, F1-5, down to 2 mm above the head surface. This combined information allowed us to begin suggesting features of airflow that specific hair fields may optimally be placed to measure. Computational fluid dynamics simulations enabled us to scrutinise the boundary layer into which the sensilla protrude. We revealed that the airflow over the head exhibited distinct differences in the

local patterns over fields F1-5 in response to small disturbances in α and β. By visualising the average flow vectors over all fields at each angle, we suggested the optimal roles for the fields based on their position on the head: F1 and F2 for sensing sideslip, F4 and F5 as step detectors of steep angles of attack, and F3 for consistently sensing changes in angle of attack. F3 had the unique property of significantly amplifying the local changes in flow direction relative to the angle of the whole head, improving its sensitivity.

Chapters 4 and 5 sought to answer the second research question. We developed a methodology to generate high-resolution three-dimensional morphological data of each trichoid sensilla over several individuals and species. 3D visualisations revealed that, although there are several hundred sensilla on each head, they are not densely packed, suggesting they are optimally spaced to prevent mechanical coupling between hairs. We also noted the consistency in directional sensitivity of hairs across individuals and taxa as well as the distinct differences in sensitivity between each field. The data provided a thorough and informative map of the response properties of the entire cephalic trichoid sensilla system. In Chapter 5 we combined our CFD flow measurements and HSV vector data to examine the relationship between stimulus and sensor. This revealed that F1 and F2 both respond similarly to oncoming airflow, with their peak responses being within 35° of the flow direction at the equilibrium flight condition. While our model revealed these fields could sense changes in angle of attack, they appear optimally placed to act as sideslip sensors. F3-5 all exhibited peak directional sensitivities approximately orthogonal to the flow at the equilibrium condition. Given the known narrowness of the static tuning curve of hair neurons, we postulated these hairs may have a role other than flight control, or only at extreme flight orientations relative to equilibrium flight.

Having established the likely inputs and sensitivity of the system, the final chapters addressed the third question by examining the locust's flight dynamics in response to varying stimuli *in vivo*. The recorded force-torque data provided clear evidence that the trichoid sensilla affect lateral force and moments. We demonstrated that covering the sensilla significantly increased and decreased side force and yaw moment derivatives

respectively. Dynamic and static changes in sideslip elicited contrasting responses in some cases, revealing slow changes in kinematics driven by postural changes in the abdomen and legs. Analysis of the lateral dynamic flight stability revealed a modal structure similar to previous studies on flying insects: an unstable monotonic mode, a stable monotonic mode, and a stable oscillatory mode. We were able to demonstrate artificially the effects of the sensilla on these modes by augmenting the stability derivatives recorded when all the sensilla were covered. We also revealed that roll feedback was necessary to stabilise the system fully, and that this was likely to be provided by the visual system.

The insights on sensor placement and sensitivity from our research could be applied directly to the use of manmade flow sensing arrays, such as those being produced by the Air Force Research Laboratories [99-102]. We suspect certain fields of hairs are playing a similar role to the vanes on manmade aircraft for sensing angles of attack and sideslip, but providing far richer information on the airflows across a surface area, rather than at a single point. Given that we have demonstrated such distinct local flow behaviours over adjacent areas of the head, monitoring flows across wide areas is likely crucial to providing an accurate picture. Therefore, we suggest any incorporation of flow sensing arrays onto manmade vehicles takes full consideration of the local placement and orientation of the sensors relative to the shape of the structure. A general trend towards arrays of sensors seems a sensible approach for the benefits of redundancy and increased information, however, our research shows they need not be ubiquitous – the cephalic sensilla are discretely arranged on only a small section of the head. With this in mind, if we refer back to our introductory chapter, in which we discussed modelling flight dynamics using direct measurement of flows and loads, our research suggests such an approach may only require a small number of optimally placed sensors measuring well-known aerodynamic quantities, such as the angles of attack and sideslip. The seemingly analogous function between natural and artificial systems leads us to conclude that our research is highly applicable to manmade applications and justifies the continued study of biological systems to inform on our own designs.

Any continuation of our research would logically focus on deconstructing the complex sensor fusion and motor signal production at the level of the descending interneurons. This would further our understanding of the relative role of airflow sensing to the visual and force sensing modalities also known to be key in locust flight control [10]. Using Camhi's previous neurophysiology experiments on individual sensilla, we have given numerical values to the spike rate of hair neurons. Thus, we already have an idea of the quantitative inputs to the DNs from one input modality. Similar characterisation is needed for the other systems used, or likely to be used, in flight control, such as the numerous other flow-sensing hairs on the locust wings. Recent behavioural experiments by Khurana and Sane [177] have demonstrated how multi-modal cues (optic flow and airflow) are combined in a linear fashion in honeybees. While earlier work by Sherman and Dickinson [178] revealed that haltere and compound eye inputs are combined in a weighted sum. These elegant demonstrations are crucial in teasing apart the multi-faceted structure of insect flight control, and are encouraging in that they show inputs combining in logical and mathematically uncomplicated ways.

On a higher level, there remain many unanswered questions on the function of neurons and the interaction between stimuli. A pertinent example is Rowell's [15] consideration of the nature and possible mechanisms of how insects 'voluntarily' change course in flight (that is, '*at times unexpected by the observer*'). Such behaviours likely require some over-riding of the 'autopilot' sensory systems such as the trichoid sensilla that maintain flight equilibrium in response to unexpected disturbances. The interplay of these seemingly distinct command structures certainly warrants further scrutiny.

It is sometimes frustrating that we cannot transport ourselves into the "mind" of a desert locust to discern rapidly the mechanics and function of seemingly simple structures like the trichoid sensilla; instead, we are consigned to third-party inference and observation. Nevertheless, the body of work amassed over seventy years of research on the species has revealed an enormous amount about animal flight and new insights have never been discovered at a greater rate. The current state of the art of tools for neurophysiology, 3D

imaging, photogrammetry, and force measurement are demonstrably sufficient to probe the inner and outer workings of insect flight. The ongoing drive towards understanding natural systems, and investment aimed at utilising biological principles in manmade designs, gives us confidence that the complexities of multi-modal flight control will be unravelled readily through continued research. We hope our insights on one component of this system will prove beneficial in answering these questions.

Bibliography

[1] Burrows, M., *The neurobiology of an insect brain*. 1996, Oxford ; New York: Oxford University Press. xv, 682 p.

[2] Srygley, R.B. and A.L.R. Thomas, *Unconventional lift-generating mechanisms in free-flying butterflies.* Nature, 2002. **420**(6916): p. 660-664.

[3] Bomphrey, R.J., *Advances in Animal Flight Aerodynamics Through Flow Measurement.* Evolutionary Biology, 2012. **39**(1): p. 1-11.

[4] CIA, *Insectothopter: The Bug-Carrying Bug.* YouTube: CIA channel (https://www.youtube.com/watch?v=TZ3spmVqnco).

[5] Matthew, K., K. Karl, and W. Henry, *Development of the Nano Hummingbird: A Tailless Flapping Wing Micro Air Vehicle*, in *50th AIAA Aerospace Sciences Meeting including the New Horizons Forum and Aerospace Exposition*. 2012, American Institute of Aeronautics and Astronautics.

[6] Caetano, J.V., et al., *Tethered vs. Free Flight Force Determination of the DelFly II Flapping Wing Micro Air Vehicle.* 2014 International Conference on Unmanned Aircraft Systems (Icuas), 2014: p. 942-948.

[7] de Croon, G.C.H.E., et al., *Design, aerodynamics and autonomy of the DelFly.* Bioinspiration & Biomimetics, 2012. **7**(2).

[8] De Clercq, K.M.E., et al., *Aerodynamic Experiments on DelFly II: Unsteady Lift Enhancement.* International Journal of Micro Air Vehicles, 2009. **1**(4): p. 255-262.

[9] de Croon, G.C.H.E., et al., *Design, aerodynamics, and vision-based control of the DelFly.* International Journal of Micro Air Vehicles, 2009. **1**(2): p. 71-97.

[10] Taylor, G.K. and H.G. Krapp, *Sensory systems and flight stability: What do insects measure and why?* Advances in Insect Physiology: Insect Mechanics and Control, 2007. **34**: p. 231-316.

[11] Snelling, E.P., et al., *Maximum metabolic rate, relative lift, wingbeat frequency and stroke amplitude during tethered flight in the adult locust Locusta migratoria.* Journal of Experimental Biology, 2012. **215**(18): p. 3317-3323.

[12] Wolf, H., *The Locust Tegula - Significance for Flight Rhythm Generation, Wing Movement Control and Aerodynamic Force Production.* Journal of Experimental Biology, 1993. **182**: p. 229-253.

[13] Fischer, H., H. Wolf, and A. Buschges, *The locust tegula: kinematic parameters and activity pattern during the wing stroke.* Journal of Experimental Biology, 2002. **205**(11): p. 1531-1545.

[14] Strausfeld, N.J., *Atlas of an insect brain*. 1976, Berlin ; New York: Springer-Verlag. xiv, 214 p.

[15] Rowell, C.H.F., *Descending Interneurones of the Locust Reporting Deviation from Flight Course - What Is Their Role in Steering.* Journal of Experimental Biology, 1989. **146**: p. 177-194.

[16] Altman, J.S., E. Anselment, and W. Kutsch, *Post-Embryonic Development of an Insect Sensory System - Ingrowth of Axons from Hindwing Sense-Organs in Locusta-Migratoria.* Proceedings of the Royal Society Series B-Biological Sciences, 1978. **202**(1149): p. 497-+.

[17] Bacon, J.P. and M. Tyrer, *Innervation of the Wind-Sensitive Head Hairs of the Locust, Schistocerca-Gregaria.* Physiological Entomology, 1979. **4**(4): p. 301-309.

[18] Pfluger, H.J. and J. Tautz, *Air Movement Sensitive Hairs and Interneurons in Locusta-Migratoria.* Journal of Comparative Physiology, 1982. **145**(3): p. 369-380.

[19] Burrows, M. and H.J. Pfluger, *Output Connections of a Wind Sensitive Interneuron with Motor Neurons Innervating Flight Steering Muscles in the Locust.* Journal of Comparative Physiology a-Neuroethology Sensory Neural and Behavioral Physiology, 1992. **171**(4): p. 437-446.

[20] Smola, U., *Receptor Potential and Nervous Impulses of Sensory Hairs on Head of Locusta-Migratoria.* Zeitschrift Fur Vergleichende Physiologie, 1970. **70**(3): p. 335-&.

[21] Camhi, J.M., *Locust Wind Receptors .I. Transducer Mechanics and Sensory Response.* Journal of Experimental Biology, 1969. **50**(2): p. 335-&.

[22] Camhi, J.M., *Locust Wind Receptors .2. Interneurones in Cervical Connective.* Journal of Experimental Biology, 1969. **50**(2): p. 349-&.

[23] Smola, U., *Investigation into Topography, Mechanics and Aerodynamics of Sensory Hairs on Head of Locusta-Migratoria.* Zeitschrift Fur Vergleichende Physiologie, 1970. **67**(4): p. 382-&.

[24] Weis-Fogh, T., *An Aerodynamic Sense Organ Stimulating and Regulating Flight in Locusts.* Nature, 1949. **164**(4177): p. 873-874.

[25] Dickinson, B.T., *Hair receptor sensitivity to changes in laminar boundary layer shape.* Bioinspiration & Biomimetics, 2010. **5**(1).

[26] Sterbing-D'Angelo, S., et al., *Bat wing sensors support flight control.* Proceedings of the National Academy of Sciences of the United States of America, 2011. **108**(27): p. 11291-11296.

[27] Weis-Fogh, T., *Biology and Physics of Locust Flight .4. Notes on Sensory Mechanisms in Locust Flight.* Philosophical Transactions of the Royal Society of London Series B-Biological Sciences, 1956. **239**(667): p. 553-584.

[28] Boyd, K.E. and D.W. Ewer, *Flight responses in grasshoppers.* S. African Sci., 1949(2): p. 168-169.

[29] Horsmann, U., H.G. Heinzel, and G. Wendler, *The Phasic Influence of Self-Generated Air Current Modulations on the Locust Flight Motor.* Journal of Comparative Physiology, 1983. **150**(4): p. 427-438.

[30] Gewecke, M. and J. Philippen, *Control of Horizontal Flight-Course by Air-Current Sense-Organs in Locusta-Migratoria.* Physiological Entomology, 1978. **3**(1): p. 43-52.

[31] Camhi, J.M., *Yaw-Correcting Postural Changes in Locusts.* Journal of Experimental Biology, 1970. **52**(3): p. 519-&.

[32] Camhi, J.M., *Sensory Control of Abdomen Posture in Flying Locusts.* Journal of Experimental Biology, 1970. **52**(3): p. 533-&.

[33] Tyrer, N.M., J.P. Bacon, and C.A. Davies, *Sensory Projections from the Wind-Sensitive Head Hairs of the Locust Schistocerca-Gregaria - Distribution in the Central Nervous-System.* Cell and Tissue Research, 1979. **203**(1): p. 79-92.

[34] Bacon, J.P. and M. Tyrer, *Tritocerebral Commissure Giant (Tcg) - Bimodal Interneurone in Locust, Schistocerca-Gregaria.* Journal of Comparative Physiology, 1978. **126**(4): p. 317-325.

[35] Rowell, C.H.F., *Orthopteran Descending Movement Detector (Dmd) Neurones - Characterisation and Review.* Zeitschrift Fur Vergleichende Physiologie, 1971. **73**(2): p. 167-&.

[36] Hensler, K., *The Pars Intercerebralis Neuron Pi(2)5 of Locusts - Convergent Processing of Inputs Reporting Head Movements and Deviations from Straight Flight.* Journal of Experimental Biology, 1988. **140**: p. 511-533.

[37] Rowell, C.H.F. and H. Reichert, *3 Descending Interneurons Reporting Deviation from Course in the Locust .2. Physiology.* Journal of Comparative Physiology a-Neuroethology Sensory Neural and Behavioral Physiology, 1986. **158**(6): p. 775-794.

[38] Schneider, D., *Insect Antennae.* Annual Review of Entomology, 1964. **9**: p. 103-&.

[39] Gewecke, M., *Movement Mechanism and Joint Receptors of Antennae of Locusta-Migratoria L (Insecta, Orthoptera).* Zeitschrift Fur Morphologie Der Tiere, 1972. **71**(2): p. 128-&.

[40] Imms, A.D., *Memoirs: On the Antennal Musculature in Insects and other Arthropods.* Journal of Cell Science, 1939. **s2-81**(322): p. 273-320.

[41] Burkhard.D and M. Gewecke, *Mechanoreception in Arthropoda - Chain from Stimulus to Behavioral Pattern.* Cold Spring Harbor Symposia on Quantitative Biology, 1965. **30**: p. 601-&.

[42] Gewecke, M., H.G. Heinzel, and Philippe.J, *Role of Antennae of Dragonfly Orthetrum-Cancellatum in Flight Control.* Nature, 1974. **249**(5457): p. 584-585.

[43] Gewecke, M. and H.G. Heinzel, *Aerodynamic and Mechanical-Properties of the Antennae as Air-Current Sense-Organs in Locusta-Migratoria .1. Static Characteristics.* Journal of Comparative Physiology, 1980. **139**(4): p. 357-366.

[44] Gewecke, M., *Central Projection of Antennal Afferents for the Flight Motor in Locusta-Migratoria (Orthoptera, Acrididae).* Entomologia Generalis, 1979. **5**(4): p. 317-320.

[45] Uchiyama, H.K. and Y. Katsuki, *Recording of action potentials from the antennal nerve of locusts by means of microelectrodes.* Physiol. Comp. Oecolog., 1956(4): p. 154-163.

[46] Gewecke, M., *Die Wirkung Von Luftstromung Auf Die Antennen Und Das Flugverhalten Der Blauen Schmeissfliege (Calliphora Erythrocephala).* Zeitschrift Fur Vergleichende Physiologie, 1967. **54**(2): p. 121-&.

[47] Gewecke, M., *Flight Control in Locusta-Migratoria by Antennae and Hairs on Frons and Vertex as Air-Current Sense-Organs.* Journal of Comparative Physiology, 1972. **80**(1): p. 57-&.

[48] Ochieng, S.A., E. Hallberg, and B.S. Hansson, *Fine structure and distribution of antennal sensilla of the desert locust, Schistocerca gregaria (Orthoptera : Acrididae).* Cell and Tissue Research, 1998. **291**(3): p. 525-536.

[49] Gewecke, M., *Influence of Air-Current Sense-Organs on Flight Behavior of Locusta-Migratoria.* Journal of Comparative Physiology, 1975. **103**(1): p. 79-95.

[50] Gewecke, M., *Antennae - Another Wind-Sensitive Receptor in Locusts.* Nature, 1970. **225**(5239): p. 1263-&.

[51] Campan, M., *Recherches Sur La Fonction Dynamogene De Lantenne Des Insectes . Experiences Sur La Geotaxie Ascensionnelle Et La Phototaxie Positive De Drosophila Melanogaster Meigen.* Comptes Rendus Des Seances De La Societe De Biologie Et De Ses Filiales, 1964. **158**(11): p. 2189-&.

[52] Neese, V., *Zur Bedeutung Der Augenborsten Bei Der Fluggeschwindigkeitsregulation Der Bienen.* Zeitschrift Fur Vergleichende Physiologie, 1966. **52**(2): p. 149-&.

[53] Niehaus, M., *Flight and Flight Control by the Antennae in the Small Tortoiseshell (Aglais-Urticae L-Lepidoptera) .2. Flight Mill and Free Flight Experiments.* Journal of Comparative Physiology, 1981. **145**(2): p. 257-264.

[54] Weis-Fogh, T., *Fat Combustion and Metabolic Rate of Flying Locusts (Schistocerca-Gregaria Forskal).* Philosophical Transactions of the Royal Society of London Series B-Biological Sciences, 1952. **237**(640): p. 1-36.

[55] Heran, H., *Wahrnehmung Und Regelung Der Flugeigengeschwindigkeit Bei Apis-Mellifica L.* Zeitschrift Fur Vergleichende Physiologie, 1959. **42**(2): p. 103-163.

[56] Krishnan, A. and S.P. Sane, *Antennal positioning in flying hawk moths.* Integrative and Comparative Biology, 2013. **53**: p. E117-E117.

[57] Schneider, G., **Die Halteren Der Schmeissfliege (Calliphora) Als Sinnesorgane Und Als Mechanische Flugstabilisatoren.* Zeitschrift Fur Vergleichende Physiologie, 1953. **35**(5): p. 416-458.

[58] Arbas, E.A., *Control of Hindlimb Posture by Wind-Sensitive Hairs and Antennae during Locust Flight.* Journal of Comparative Physiology a-Neuroethology Sensory Neural and Behavioral Physiology, 1986. **159**(6): p. 849-857.

[59] Grunert, U. and W. Gnatzy, *Campaniform Sensilla of Calliphora-Vicina (Insecta, Diptera) .2. Typology.* Zoomorphology, 1987. **106**(5): p. 320-328.

[60] Vincent, J.F.V. and U.G.K. Wegst, *Design and mechanical properties of insect cuticle.* Arthropod Structure & Development, 2004. **33**(3): p. 187-199.

[61] Dumpert, K. and W. Gnatzy, *Cricket Combined Mechanoreceptors and Kicking Response.* Journal of Comparative Physiology, 1977. **122**(1): p. 9-25.

[62] Heinzel, H.G. and M. Gewecke, *Directional Sensitivity of the Antennal Campaniform Sensilla in Locusts.* Naturwissenschaften, 1979. **66**(4): p. 212-213.

[63] Elson, R.C., *Flight Motor-Neuron Reflexes Driven by Strain-Sensitive Wing Mechanoreceptors in the Locust.* Journal of Comparative Physiology a-Sensory Neural and Behavioral Physiology, 1987. **161**(5): p. 747-760.

[64] Gettrup, E., *Sensory Regulation of Wing Twisting in Locusts.* Journal of Experimental Biology, 1966. **44**(1): p. 1-&.

[65] Newland, P.L. and N.J. Emptage, *The central connections and actions during walking of tibial campaniform sensilla in the locust.* Journal of Comparative Physiology a-Sensory Neural and Behavioral Physiology, 1996. **178**(6): p. 749-762.

[66] Zaćwilichowski, J., *Uber die Innervierung und die Sinnesorgane der Flugel der Feldheuschrecke Stauroderus biguttulus (L.).* Bull. Int. Acad. Pol. Sci. Lett. B 1934. **11**: p. 187-196.

[67] Gettrup, E., *Sensory Mechanisms in Locomotion - Campaniform Sensilla of Insect Wing and Their Function during Flight.* Cold Spring Harbor Symposia on Quantitative Biology, 1965. **30**: p. 615-&.

[68] Elson, R.C., *Integration of Wing Proprioceptive and Descending Exteroceptive Sensory Inputs by Thoracic Interneurons of the Locust.* Journal of Experimental Biology, 1987. **128**: p. 193-217.

[69] Elson, R.C., *Interneuronal Processing of Inputs from the Campaniform Sensilla of the Locust Hindwing.* Journal of Comparative Physiology a-Sensory Neural and Behavioral Physiology, 1987. **161**(5): p. 761-776.

[70] Waldron, I., *Mechanisms for Production of Motor Output Pattern in Flying Locusts.* Journal of Experimental Biology, 1967. **47**(2): p. 201-&.

[71] Wendler, G., *Influence of Proprioceptive Feedback on Locust Flight Coordination.* Journal of Comparative Physiology, 1974. **88**(2): p. 173-200.

[72] Wendler, G., *Possible Role of Fast Wing Reflexes in Locust Flight.* Naturwissenschaften, 1978. **65**(1): p. 65-66.

[73] Wilson, D.M. and T. Weis-Fogh, *Patterned Activity of Co-Ordinated Motor Units, Studied in Flying Locusts.* Journal of Experimental Biology, 1962. **39**(4): p. 643-&.

[74] Taylor, G.K., *Mechanics and aerodynamics of insect flight control.* Biological Reviews, 2001. **76**(4): p. 449-471.

[75] Gettrup, E. and D.M. Wilson, *Lift-Control Reaction of Flying Locusts.* Journal of Experimental Biology, 1964. **41**(1): p. 183-&.

[76] Taylor, G.K., *Modelling the effects of unsteady flow phenomena on flapping flight dynamics – stability and control.* Flow Phenomena in Nature: A Challenge to Engineering Design, 2007. **1**: p. 155-166.

[77] Bryan, G.H., *Stability in aviation; an introduction to dynamical stability as applied to the motions of aeroplanes*. 1911, London,: Macmillan and co., limited. x p., 1 l., 92 p.

[78] Tobak, M.S. and L.B. Schiff, *Aerodynamic mathematical modeling—basic concepts.* NATO Advisory Group for Aeronautical Research and Development, 1981(114): p. 1.1-1.32.

[79] Goman, M. and A. Khrabrov, *State-Space Representation of Aerodynamic Characteristics of an Aircraft at High Angles of Attack.* Journal of Aircraft, 1994. **31**(5): p. 1109-1115.

[80] Liebe, R., *Flow phenomena in nature*. Design and nature. 2007, Southampton ; Boston: WIT.

[81] Klein, V., *Modeling of aircraft unsteady aerodynamic characteristics. Part 1, Postulated models [microform] / Vladislav Klein and Keith D. Noderer*. NASA technical memorandum ; 109120, ed. K.D. Noderer and C. Langley Research. 1994, Hampton, Va. : [Springfield, Va: National Aeronautics and Space Administration, Langley Research Center ; National Technical Information Service, distributor.

[82] Pfau, H.K., U.T. Koch, and B. Mohl, *Temperature-Dependence and Response Characteristics of the Isolated Wing Hinge Stretch-Receptor in the Locust.* Journal of Comparative Physiology a-Sensory Neural and Behavioral Physiology, 1989. **165**(2): p. 247-252.

[83] Krapp, H.G., G.K. Taylor, and J.S. Humbert, *The mode-sensing hypothesis: matching sensors, actuators and flight dynamics.* Frontiers in Sensing: From Biology to Engineering, 2012: p. 101-114.

[84] Arun, S.M. and J.B. Martin, *Fly-by-Feel Sensing and Control: Aeroservoelasticity*, in *AIAA Atmospheric Flight Mechanics Conference*. 2014, American Institute of Aeronautics and Astronautics.

[85] Zbikowski, R., *Sensor-rich feedback control.* Ieee Instrumentation & Measurement Magazine, 2004. **7**(3): p. 19-26.

[86] Samy, I., et al., *Neural-Network-Based Flush Air Data Sensing System Demonstrated on a Mini Air Vehicle.* Journal of Aircraft, 2010. **47**(1): p. 18-31.

[87] Dijkstra, M., et al., *Artificial sensory hairs based on the flow sensitive receptor hairs of crickets.* Journal of Micromechanics and Microengineering, 2005. **15**(7): p. S132-S138.

[88] Takahashi, H., et al., *Air flow senser for an insect-like flapping wing.* Mems 2008: 21st Ieee International Conference on Micro Electro Mechanical Systems, Technical Digest, 2008: p. 916-919.

[89] Jaganatharaja, R.K., et al., *Unraveling the Viscosity-Mediated Coupling Effect in Biomimetic Hair Sensor Arrays.* 2011 Ieee 24th International Conference on Micro Electro Mechanical Systems (Mems), 2011: p. 652-655.

[90] Casas, J., T. Steinmann, and G. Krijnen, *Why do insects have such a high density of flow-sensing hairs? Insights from the hydromechanics of biomimetic MEMS sensors.* Journal of the Royal Society Interface, 2010. **7**(51): p. 1487-1495.

[91] Huang, K.Y. and C.T. Huang, *Hair sensor using a photoelectronic principle for sensing airflow and its direction.* Optical Engineering, 2011. **50**(1).

[92] Maschmann, M.R., et al., *Force sensitive carbon nanotube arrays for biologically inspired airflow sensing.* Smart Materials and Structures, 2012. **21**(9).

[93] Sadeghi, M.M., R.L. Peterson, and K. Najafi, *Hair-based sensors for micro-autonomous systems.* Micro- and Nanotechnology Sensors, Systems, and Applications Iv, 2012. **8373**.

[94] Tang, Y., R.L. Peterson, and K. Najafi, *Technology for Fabricating Dense 3-D Microstructure Arrays for Biomimetic Hair-Like Sensors.* 26th Ieee International Conference on Micro Electro Mechanical Systems (Mems 2013), 2013: p. 355-358.

[95] Ozaki, Y., et al. *An air flow sensor modeled on wind receptor hairs of insects*. in *Micro Electro Mechanical Systems, 2000. MEMS 2000. The Thirteenth Annual International Conference on*. 2000.

[96] National Instruments, *How Is Temperature Affecting Your Strain Measurement Accuracy?* 2011.

[97] Krijnen, G.J.M., et al., *MEMS based hair flow-sensors as model systems for acoustic perception studies.* Nanotechnology, 2006. **17**(4): p. S84-S89.

[98] Dagamseh, A.M.K., et al., *Engineering of Biomimetic Hair-Flow Sensor Arrays Dedicated to High-Resolution Flow Field Measurements.* 2010 Ieee Sensors, 2010: p. 2251-2254.

[99] Slinker, K., et al., *Variable Deflection Response of Sensitive CNT-on-Fiber Artificial Hair Sensors from CNT Synthesis in High Aspect Ratio Microcavities.* Bioinspiration, Biomimetics, and Bioreplication 2015, 2015. **9429**.

[100] Maschmann, M.R., et al., *Bioinspired Carbon Nanotube Fuzzy Fiber Hair Sensor for Air-Flow Detection.* Advanced Materials, 2014. **26**(20): p. 3230-+.

[101] Phillips, D.M., et al., *Artificial Hair Sensors: Electro-Mechanical Characterization.* Proceedings of the Asme Conference on Smart Materials Adaptive Structures and Intelligent Systems, 2014. **2**.

[102] Chidurala, M., B.T. Dickinson, and U.K. Chakravarty, *Dynamic Response of Biomimetic Hair Receptors in Both Steady and Unsteady Flow Environment.* Proceedings of the Asme International Mechanical Engineering Congress and Exposition, 2014. **10**.

[103] Su, W.H. and G.W. Reich, *Gust alleviation of highly flexible UAVs with artificial hair sensors.* Sensors and Smart Structures Technologies for Civil, Mechanical, and Aerospace Systems 2015, 2015. **9435**.

[104] Phillips, D.M., et al., *Detection of flow separation and stagnation points using artificial hair sensors.* Smart Materials and Structures, 2015. **24**(11).

[105] Vincent, J.F.V., *Biomimetics - a review.* Proceedings of the Institution of Mechanical Engineers Part H-Journal of Engineering in Medicine, 2009. **223**(H8): p. 919-939.

[106] Eberle, A.L., et al., *A new twist on gyroscopic sensing: body rotations lead to torsion in flapping, flexing insect wings.* Journal of the Royal Society Interface, 2015. **12**(104).

[107] Dickerson, B.H., Z.N. Aldworth, and T.L. Daniel, *Control of moth flight posture is mediated by wing mechanosensory feedback.* Journal of Experimental Biology, 2014. **217**(13): p. 2301-2308.

[108] Fox, J.L., A.L. Fairhall, and T.L. Daniel, *Encoding properties of haltere neurons enable motion feature detection in a biological gyroscope.* Proceedings of the National Academy of Sciences of the United States of America, 2010. **107**(8): p. 3840-3845.

[109] Fox, J.L. and T.L. Daniel, *A neural basis for gyroscopic force measurement in the halteres of Holorusia.* Journal of Comparative Physiology a-Neuroethology Sensory Neural and Behavioral Physiology, 2008. **194**(10): p. 887-897.

[110] Ellington, C.P., et al., *Leading-edge vortices in insect flight.* Nature, 1996. **384**(6610): p. 626-630.

[111] Henningsson, P. and R.J. Bomphrey, *A view of dragonfly and damselfly aerodynamics through high-speed stereo PIV.* Integrative and Comparative Biology, 2011. **51**: p. E56-E56.

[112] Bomphrey, R.J., G.K. Taylor, and A.L.R. Thomas, *Smoke visualization of free-flying bumblebees indicates independent leading-edge vortices on each wing pair.* Experiments in Fluids, 2009. **46**(5): p. 811-821.

[113] Bomphrey, R.J., et al., *Application of digital particle image velocimetry to insect aerodynamics: measurement of the leading-edge vortex and near wake of a Hawkmoth.* Experiments in Fluids, 2006. **40**(4): p. 546-554.

[114] Bomphrey, R.J., et al., *The aerodynamics of Manduca sexta: digital particle image velocimetry analysis of the leading-edge vortex.* Journal of Experimental Biology, 2005. **208**(6): p. 1079-1094.

[115] Bomphrey, R.J., et al., *Digital particle image velocimetry measurements of the downwash distribution of a desert locust Schistocerca gregaria.* J R Soc Interface, 2006. **3**(7): p. 311-7.

[116] Bomphrey, R.J., et al., *Tomographic particle image velocimetry of desert locust wakes: instantaneous volumes combine to reveal hidden vortex elements and rapid wake deformation.* J R Soc Interface, 2012. **9**(77): p. 3378-86.

[117] Elsinga, G.E., et al., *Tomographic particle image velocimetry.* Experiments in Fluids, 2006. **41**(6): p. 933-947.

[118] Spedding, G.R., M. Rosen, and A. Hedenstrom, *A family of vortex wakes generated by a thrush nightingale in free flight in a wind tunnel over its entire natural range of flight speeds.* Journal of Experimental Biology, 2003. **206**(14): p. 2313-2344.

[119] Henningsson, P., et al., *The complex aerodynamic footprint of desert locusts revealed by large-volume tomographic particle image velocimetry.* Journal of the Royal Society Interface, 2015. **12**(108).

[120] Feldkamp, L.A., L.C. Davis, and J.W. Kress, *Practical Cone-Beam Algorithm.* Journal of the Optical Society of America a-Optics Image Science and Vision, 1984. **1**(6): p. 612-619.

[121] Taylor, G.K. and A.L.R. Thomas, *Dynamic flight stability in the desert locust Schistocerca gregaria.* Journal of Experimental Biology, 2003. **206**(16): p. 2803-2829.

[122] Walker, S., A. Thomas, and G. Taylor, *Photogrammetry and Kalman filtering used to obtain topographic kinematics of tethered locust flight.* Comparative Biochemistry and Physiology a-Molecular & Integrative Physiology, 2005. **141**(3): p. S131-S131.

[123] Walker, S., G. Taylor, and A. Thomas, *Kinematics and aerodynamics of tethered locust flight.* Comparative Biochemistry and Physiology a-Molecular & Integrative Physiology, 2007. **146**(4): p. S114-S114.

[124] Weis-Fogh, T., *Biology and Physics of Locust Flight .2. Flight Performance of the Desert Locust (Schistocerca-Gregaria).* Philosophical Transactions of the Royal Society of London Series B-Biological Sciences, 1956. **239**(667): p. 459-510.

[125] Waloff, Z., *Observations on Airspeeds of Freely Flying Locusts.* Animal Behaviour, 1972. **20**(May): p. 367-&.

[126] Baker, P.S., M. Gewecke, and R.J. Cooter, *The Natural Flight of the Migratory Locust, Locusta-Migratoria L .3. Wing-Beat Frequency, Flight Speed and Attitude.* Journal of Comparative Physiology, 1981. **141**(2): p. 233-237.

[127] Etkin, B. and L.D. Reid, *Dynamics of flight : stability and control*. 3rd ed. 1996, New York: Wiley. xi, 382 p.

[128] Gillespie, D., *An Intro to Computational Fluid Dynamics*. General Material on CFD - Osney-Thermo Laboratory Fluids.

[129] Tritton, D.J., *Physical fluid dynamics*. 2nd ed. Oxford science publications. 1988, Oxford England New York: Clarendon Press ; Oxford University Press. xvii, 519 p.

[130] Young, J., et al., *Numerical simulation of the aerodynamics of a desert locust (Schistocerca gregaria) in forward flight.* Comparative Biochemistry and Physiology a-Molecular & Integrative Physiology, 2008. **150**(3): p. S79-S79.

[131] Nakata, T. and H. Liu, *A fluid-structure interaction model of insect flight with flexible wings.* Journal of Computational Physics, 2012. **231**(4): p. 1822-1847.

[132] Noda, R., T. Nakata, and H. Liu, *Effects of wing deformation on aerodynamic performance of a revolving insect wing.* Acta Mechanica Sinica, 2014. **30**(6): p. 819-827.

[133] Sun, M. and Y. Xiong, *Dynamic flight stability of a hovering bumblebee.* Journal of Experimental Biology, 2005. **208**(3): p. 447-459.

[134] Sun, M., Y.P. Liu, and J.K. Wang, *Dynamic flight stability of a hovering hoverfly.* New Trends in Fluid Mechanics Research, 2007: p. 626-629.

[135] Alliez, P., et al., *Isotropic surface remeshing.* Smi 2003: Shape Modeling International 2003, Proceedings, 2003: p. 49-58.

[136] Taubin, G., *Curve and surface smoothing without shrinkage.* Fifth International Conference on Computer Vision, Proceedings, 1995: p. 852-857.

[137] Sane, S.P. and N.P. Jacobson, *Induced airflow in flying insects - II. Measurement of induced flow.* Journal of Experimental Biology, 2006. **209**(1): p. 43-56.

[138] Hengstenberg, R., *Multisensory control in insect oculomotor systems.* Rev Oculomot Res, 1993. **5**: p. 285-98.

[139] Kutsch, W., J. Camhi, and G. Sumbre, *Close Encounters among Flying Locusts Produce Wing-Beat Coupling.* Journal of Comparative Physiology a-Neuroethology Sensory Neural and Behavioral Physiology, 1994. **174**(5): p. 643-649.

[140] Huston, S.J. and H.G. Krapp, *Visuomotor transformation in the fly gaze stabilization system.* Plos Biology, 2008. **6**(7): p. 1468-1478.

[141] Boyde, A., et al., *Iodine Vapor Staining for Atomic Number Contrast in Backscattered Electron and X-Ray Imaging.* Microscopy Research and Technique, 2014. **77**(12): p. 1044-1051.

[142] Chapman, R.F., S.J. Simpson, and A.E. Douglas, *The insects : structure and function*. Fifth edition / ed. 2013, New York: Cambridge University Press. xxxi, 929 pages.

[143] Boas, F.E. and D. Fleischmann, *CT artifacts: causes and reduction techniques.* Imaging in Medicine, 2012. **4**(2): p. 229-240.

[144] Walker, S.M., et al., *In Vivo Time- Resolved Microtomography Reveals the Mechanics of the Blowfly Flight Motor*. Plos Biology, 2014. **12**(3).

[145] Paganin, D., et al., *Simultaneous phase and amplitude extraction from a single defocused image of a homogeneous object.* Journal of Microscopy-Oxford, 2002. **206**: p. 33-40.

[146] Weitkamp, T., et al., *ANKAphase: software for single-distance phase retrieval from inline X-ray phase-contrast radiographs.* Journal of Synchrotron Radiation, 2011. **18**: p. 617-629.

[147] Marone, F., B. Munch, and M. Stampanoni, *Fast reconstruction algorithm dealing with tomography artifacts.* Developments in X-Ray Tomography Vii, 2010. **7804**.

[148] Van Uitert, R. and I. Bitter, *Subvoxel precise skeletons of volumetric data based on fast marching methods.* Medical Physics, 2007. **34**(2): p. 627-638.

[149] Berens, P., *CircStat: A MATLAB Toolbox for Circular Statistics.* 2009, 2009. **31**(10): p. 21.

[150] Fisher, N.I., *Statistical Analysis of Circular Data.* 1995.

[151] Harrison, D. and G.K. Kanji, *The development of analysis of variance for circular data.* Journal of Applied Statistics, 1988. **15**(2): p. 197-223.

[152] Harrison, D., G.K. Kanji, and R. Gadsden, *Analysis of variance for circular data.* Journal of Applied Statistics, 1986. **13**(2): p. 123-138.

[153] Jammalamadaka, S.R. and A. Sengupta, *Topics in Circular Statistics.* World Scientific, 2001.

[154] Svidersky, V.L., *Electrical activity in receptors concerned with maintenance of flight in locusts (In Russian).* Dokl. Akad. Nauk. Sci. SSSR, 1967(172): p. 1230-1233.

[155] Mohl, B. and J.P. Bacon, *The Tritocerebral Commissure Giant (Tcg) Wind-Sensitive Interneurone in the Locust .2. Directional Sensitivity and Role in Flight Stabilization.* Journal of Comparative Physiology, 1983. **150**(4): p. 453-465.

[156] Zarnack, W. and M. Wortmann, *On the So-Called Constant-Lift Reaction of Migratory Locusts.* Journal of Experimental Biology, 1989. **147**: p. 111-124.

[157] Wortmann, M. and W. Zarnack, *Wing Movements and Lift Regulation in the Flight of Desert Locusts.* Journal of Experimental Biology, 1993. **182**: p. 57-69.

[158] Windsor, S.P., R.J. Bomphrey, and G.K. Taylor, *Vision-based flight control in the hawkmoth Hyles lineata.* Journal of the Royal Society Interface, 2014. **11**(91).

[159] Doube, M., et al., *BoneJ Free and extensible bone image analysis in ImageJ.* Bone, 2010. **47**(6): p. 1076-1079.

[160] Muller, T., *Vision-based flight control and stabilisation in hawkmoths.* DPhil Thesis, 2015.

[161] Adali, T. and S.S. Haykin, *Adaptive signal processing : next generation solutions*. Adaptive and learning systems for signal processing, communications, and control. 2010, Hoboken, N.J.: Wiley-IEEE.

[162] Hedrick, T.L., B. Cheng, and X.Y. Deng, *Wingbeat Time and the Scaling of Passive Rotational Damping in Flapping Flight.* Science, 2009. **324**(5924): p. 252-255.

[163] Liang, B. and M. Sun, *Dynamic flight stability of a hovering model dragonfly.* Journal of Theoretical Biology, 2014. **348**: p. 100-112.

[164] Xu, N. and M. Sun, *Lateral dynamic flight stability of a model bumblebee in hovering and forward flight.* Journal of Theoretical Biology, 2013. **319**: p. 102-115.

[165] Ristroph, L., et al., *Active and passive stabilization of body pitch in insect flight.* Journal of the Royal Society Interface, 2013. **10**(85).

[166] Sun, M., J.K. Wang, and Y. Xiong, *Dynamic flight stability of hovering insects.* Acta Mechanica Sinica, 2007. **23**(3): p. 231-246.

[167] Zhang, Y.L. and M. Sun, *Dynamic flight stability of hovering model insects: theory versus simulation using equations of motion coupled with Navier-Stokes equations.* Acta Mechanica Sinica, 2011. **27**(2): p. 308-308.

[168] Liang, B. and M. Sun, *Nonlinear flight dynamics and stability of hovering model insects.* Journal of the Royal Society Interface, 2013. **10**(85).

[169] Taylor, G.K. and R. Zbikowski, *Nonlinear time-periodic models of the longitudinal flight dynamics of desert locusts Schistocerca gregaria.* Journal of the Royal Society Interface, 2005. **2**(3): p. 197-221.

[170] Taylor, G.K., R.J. Bomphrey, and J. 't Hoen, *Insect Flight Dynamics and Control*, in *44th AIAA Aerospace Sciences Meeting and Exhibit*. 2006, American Institute of Aeronautics and Astronautics.

[171] Kumar, R. and S. Shkarayev, *Kinematic and Aerodynamic Response of Locusts in Sideslip.* International Journal of Micro Air Vehicles, 2015. **7**(2): p. 159-180.

[172] Taylor, G.K. and A.L.R. Thomas, *Animal flight dynamics II. Longitudinal stability in flapping flight.* Journal of Theoretical Biology, 2002. **214**(3): p. 351-370.

[173] Zhang, Y.L. and M. Sun, *Dynamic flight stability of a hovering model insect: lateral motion.* Acta Mechanica Sinica, 2010. **26**(2): p. 175-190.

[174] Cook, M.V., *Flight Dynamics Principles: A Linear Systems Approach to Aircraft Stability and Control, 3rd Edition.* Flight Dynamics Principles: A Linear Systems Approach to Aircraft Stability and Control, 3rd Edition, 2013: p. 1-575.

[175] Sun, M. and J.K. Wang, *Flight stabilization control of a hovering model insect.* Journal of Experimental Biology, 2007. **210**(15): p. 2714-2722.

[176] Goodman, L.J., *The Role of Certain Optomotor Reactions in Regulating Stability in the Rolling Plane During Flight in the Desert Locust, Schistocerca Gregaria.* Journal of Experimental Biology, 1965. **42**(3): p. 385-407.

[177] Roy Khurana, T. and S.P. Sane, *Airflow and optic flow mediate antennal positioning in flying honeybees.* Elife, 2016. **5**.

[178] Sherman, A. and M.H. Dickinson, *Summation of visual and mechanosensory feedback in Drosophila flight control.* Journal of Experimental Biology, 2004. **207**(1): p. 133-142.